ONE-DIMENSIONAL ZINC OXIDE NANOMATERIALS

SYNTHESIS AND PHOTOVOLTAIC APPLICATIONS

A Dissertation
Presented to
The Academic Faculty

by

Benjamin A. Weintraub

In Partial Fulfillment
of the Requirements for the Degree
Doctor of Philosophy in the
School of Materials Science & Engineering

Georgia Institute of Technology
August 2010

ONE-DIMENSIONAL ZINC OXIDE NANOMATERIALS

SYNTHESIS AND PHOTOVOLTAIC APPLICATIONS

Approved by:

Dr. Zhong Lin 'ZL' Wang, Advisor
School of Materials Science & Engineering
Georgia Institute of Technology

Dr. Yulin Deng, Co-advisor
School of Chemical & Biomolecular Engineering
Georgia Institute of Technology

Dr. Robert L. Snyder
School of Materials Science & Engineering
Georgia Institute of Technology

Dr. W. Brent Carter
School of Materials Science & Engineering
Georgia Institute of Technology

Dr. Christopher Summers
School of Materials Science & Engineering
Georgia Institute of Technology

Date Approved: May 19, 2010

To my family

ACKNOWLEDGEMENTS

I wish to thank my advisors Professor Zhong Lin Wang and Professor Yulin Deng for providing academic guidance during my doctoral studies at Georgia Tech. I want to acknowledge my thesis committee members, Professor Robert Snyder, Professor Christopher Summers, and Professor Brent Carter for their comments on my thesis and helping me to establish an advanced materials science & engineering foundation through their course offerings. I wish to thank a number of my collaborators at Georgia Tech including Sehoon Chang, Dr. Singamaneni, and Dr. Buchine. I deeply enjoyed working and learning from you. I would like to thank Susan Bowman and Professor Tom Sanders for their sage advising and IPST at Georgia Tech for funding my research.

On a personal note, I would like to thank my parents for their unwavering love and support from the beginning and Uncle Peter for always encouraging and supporting my academic endeavors. For mentoring me at a crucial age and helping me to develop my own personal mechanism for overcoming challenges, I would like to acknowledge Master Kenneth Church. Lastly, to my fiancée Ivy – I would never have obtained this academic goal if it were not for your uncompromising support at every turn.

TABLE OF CONTENTS

LIST OF TABLES

LIST OF FIGURES

LIST OF ABBREVIATIONS

AC	Alternate Current
AFM	Atomic Force Microscope
AM	Air Mass
ALD	Atomic Layer Deposition
CNT	Carbon Nanotube
DC	Direct Current
DSSC	Dye-Sensitized Solar Cell
EQE	External Quantum Efficiency
FE	Field Emission
FIB	Focused Ion Beam
FN	Fowler-Nordheim
HMTA	Hexamethylenetetramine
ICP	Inductive Coupled Plasma
IPCE	Incident-Photon-to-electron Conversion Efficiency
ITO	Indium Tin Oxide
LBL	Layer-By-Layer
LHE	Light Harvesting Efficiency
MEMS	Micrometer-Electro-Mechanical-Systems
NEMS	Nanometer-Electro-Mechanical-Systems
NR	Nanorod
NW	Nanowire
PAH	Poly(allylamine hydrochloride)
PDMS	Polydimethylsiloxane

PI	Polyimide
PL	Photoluminescence
PMMA	Polymethylmethacrylate
PS	Polystyrene
PSS	Poly(sodium 4-styrenesulfonate)
SC	Solar Cell
SAM	Self-Assembled Monolayer
SEM	Scanning Electron Microscope
UV	Ultra-violet
XPS	X-ray Photoelectron Spectroscopy
XRD	X-ray Diffraction

LIST OF SYMBOLS

η	Efficiency [%]
β	Field Enhancement Factor [dimensionless]
d	Gap Distance [m]
φ	Work Function [eV]
σ	Supersaturation [dimensionless]
Φ_{inj}	Electron Injection Efficiency [%]
η_c	Charge Collection Efficiency [%]
k	Slope of F-N Curve [dimensionless]
λ	Wavelength [m]
I	Current [A]
J	Current Density [A/m^2]
R	Resistance [Ω]
V	Voltage [V]
ε	Extinction coefficient [dimensionless]
L_n	Diffusion length [m]
Resp	Responsivity [A/W]

SUMMARY

As humanly engineered materials systems approach the atomic scale, top-down manufacturing approaches breakdown and following nature's example, bottom-up or self-assembly methods have the potential to emerge as the dominant paradigm. Synthesis of one-dimensional nanomaterials takes advantage of such self-assembly manufacturing techniques, but until now most efforts have relied on high temperature vapor phase schemes which are limited in scalability and compatibility with organic materials. The solution-phase approach is an attractive low temperature alternative to overcome these shortcomings. To this end, this thesis is a study of the rationale solution-phase synthesis of ZnO nanowires and applications in photovoltaics.

The following thesis goals have been achieved: rationale synthesis of a single ZnO nanowire on a polymer substrate without seeding, design of a wafer-scale technique to control ZnO nanowire array density using layer-by-layer polymers, determination of optimal nanowire field emitter density to maximize the field enhancement factor, design of bridged nanowires across metal electrodes to order to circumvent post-synthesis manipulation steps, electrical characterization of bridged nanowires, rationale solution-phase synthesis of long ZnO nanowires on optical fibers, fabrication of ZnO nanowire dye-sensitized solar cells on optical fibers, electrical and optical characterization of solar cell devices, comparison studies of 2-D versus 3-D nanowire dye-sensitized solar cell devices, and achievement of 6-fold solar cell power conversion efficiency enhancement using a 3-D approach. The thesis results have implications in nanomanufacturing scale-up and next generation photovoltaics.

CHAPTER 1

INTRODUCTION

Nanotechnology and nanoscience are common terms for 21st century chemistry. As humanly engineered materials systems approach the atomic scale, top-down manufacturing approaches breakdown and following nature's example, bottom-up or self-assembly methods emerge as the dominant paradigm. Nanotechnology utilizes materials at length scales below 100 nm and takes advantage of such self-assembly manufacturing techniques. At such small length scales, quantum mechanical effects give rise to novel material behavior compared to the bulk. In recent years, a tremendous amount of research effort has gone towards studying synthesis, fundamental properties, manipulation, characterization, device fabrication, and testing. These new materials and systems have far reaching implications for important industry sectors including medicine, security, communication, transportation, and energy.

As environmental and supply concerns of fossil fuels grow, it is apparent that finding a green and renewable energy source will be the most important challenge of the 21st century. Among the potential clean energy sources such as nuclear, biofuels, wind, ocean, and solar thermal, solar photovoltaic is a viable candidate and has been receiving increased attention recently. However, solar photovoltaic technology still faces significant material challenges before achieving grid parity ($1/watt) and widespread acceptance.

1.1 Thesis Scientific Questions

With this short introduction to nanotechnology and photovoltaics in mind, there were a number of scientific questions that this thesis sought to address. First, how can we apply self-assembly materials synthesis approaches to improve the rational growth of one-dimensional nanostructures? Second, how can we develop self-assembly nanostructure synthesis pathways to promote synergy between both organic and inorganic materials systems for expanded applicability? Third, how can we overcome the optical absorption depth/carrier diffusion length dilemma common in excitonic solar cells? Lastly, how can we develop new photon management techniques with general applicability to photovoltaics?

1.2 Thesis overview

The following is an overview of this thesis. Chapter 2 provides a background in nanotechnology and photovoltaic fundamentals and provides a context for the content in later chapters. Chapter 3 discusses rationale ZnO nanowire synthesis using aqueous solution-based approaches. Chapter 4 examines photovoltaic device fabrication and electrical and optical characterization. Chapter 5 discusses future directions and new questions raised. Finally, the thesis ends with a conclusion in chapter 6.

CHAPTER 2

ZINC OXIDE NANOWIRES & PHOTOVOLTAICS

This chapter provides a theoretical background and framework into which the content of subsequent chapters will be introduced. Within this chapter, topics will include ZnO material properties, nanowire synthesis fundamentals, and fundamental photovoltaic theory.

2.1 Zinc Oxide

There has been a revival of interest in the ZnO materials system during the last decade as a functional material with widespread applicability in fields spanning electronics, optics, and magnetism. To understand its importance, the following section discusses various materials properties.

2.2.1 Material properties

Similar to other II-VI semiconductor materials, ZnO exhibits a hexagonal crystal structure (point group 3m, space group C6mc, lattice parameters a = 3.296 Å and c= 5.207 Å) and belongs to the wurtzite crystal structure family whose defining features are non-centrosymmetric symmetry and polar surfaces. The thermodynamically stable phase for ZnO is the wurtzite structure although two metastable cubic phases exist as well, namely zinc blende and high pressure rocksalt (see Figure 2.1). The hexagonal unit cell contains two formula units. The crystal structure (see Figure 2.2) is best described as alternating planes composed of tetrahedrally coordinated Zn^{2+} and O^{2-} ions stacked along the c axis. The oppositely charged ions produce a positively charged (0001)-Zn

terminated and $(000\bar{1})$-O terminated polar surface. The structure is enclosed by non-polar $(10\bar{1}0)$ and $(11\bar{2}0)$ faces. ZnO is a relatively open structure with half of the tetrahedral sites being occupied by Zn^{2+} and all the octahedral sites remaining empty. ZnO exhibits both piezoelectric and pyroelectric behavior due to the non-centrosymmetric symmetry inherent to the wurtzite family crystal structure.

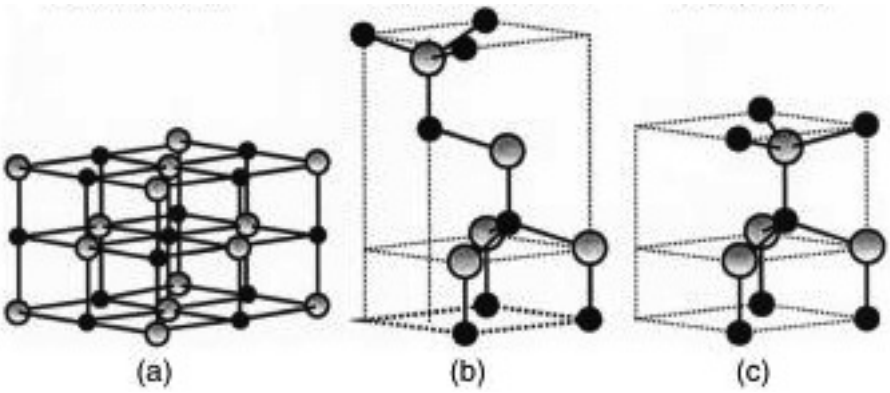

Figure 2.1 ZnO crystal structure models: (a) cubic rocksalt, (b) cubic zinc blende, and (c) hexagonal wurtzite. The shaded gray and black spheres denote Zn and O atoms, respectively. [1]

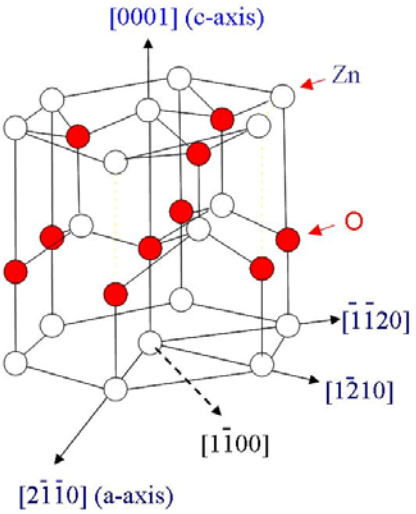

Figure 2.2 ZnO wurtzite crystal defining the crystallographic directions

It is a wide direct bandgap (3.37 eV) semiconductor with a large excitation binding energy (60 meV) which ensures efficient excitonic emission in the UV range at room temperature [2]. It is intrinsically an n-type semiconductor. Electron doping is attributed to Zn interstitials (V''_{Zn} V'_{Zn}), oxygen vacancies ($V^{\bullet\bullet}_{O}$ $V^{\bullet}_{O}$ V_O), and hydrogen [3-8]. The n-type intrinsic defect levels lay 0.01-0.05 eV below the conduction band (see Figure 2.3). For electronic applications, p-type doping is quite useful, but has proven difficult to achieve [9].

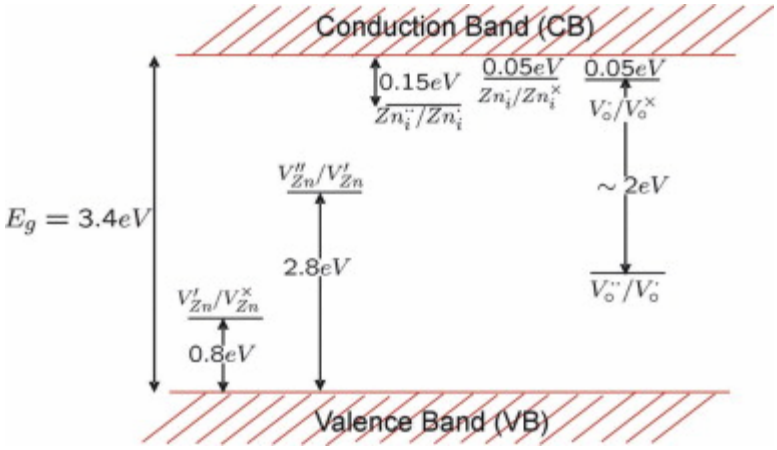

Figure 2.3 Energy levels of native defects in ZnO. Adapted from [10].

The non-centrosymmetric symmetry of the wurtzite crystal structure leads to piezoelectricity in ZnO. Piezoelectricity arises from atomic scale polarization. The ZnO unit cell in Figure 2.4a shows a Zn^{2+} cation situated inside a tetrahedral cage surrounded by O^{2-} anions. Under non-stress conditions, the positive and negative center of mass coincide so all ionic dipoles cancel (Figure 2.4b). However, when the crystal is subjected to a mechanical force, **F**, the positive and negative centers of mass become displaced with respect to each other leading to a net polarization, **P** (Figure 2.4). In single crystal ZnO, this results in a macroscopic dipole whereby positive and negative electric charge builds

up on opposite crystal faces. The polarization and applied stress are linearly related as shown by the following equation:

$$P_i = d_{ij}T_j \quad (1)$$

T_j, a mechanical stress exerted along direction j and P_i, the induced polarization along direction i are related by the piezoelectric coefficient, d_{ij}. The strongest piezoelectric coefficient (d_{33}) in ZnO arises from a stress applied along the [0001] direction resulting in polarization across the (0001) and $(000\bar{1})$ planes. The effective piezoelectric coefficient (d_{33}) of a ZnO nanobelt was experimentally measured by piezoresponse force microscopy ranging from 14.3 pm V^{-1} to 26.7 pm V^{-1} depending on the frequency [11]. It is worth noting that these are higher than the ZnO bulk value of 9.93 pm V^{-1}. The converse piezoelectric effect also exists whereby an applied electric field, E_i induces strain, S_j in the crystal represented by the following equation:

$$S_j = d_{ij}E_i \quad (2)$$

The piezoelectric coefficient, d_{ij} is defined in the same way as above. In general, ZnO piezoelectric crystals are electromechanical transducers which can convert electric signals to mechanical signals, and vice versa.

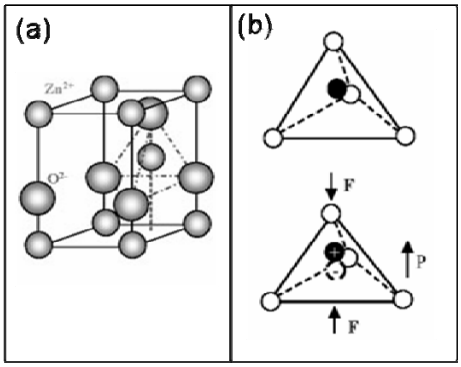

Figure 2.4 (a) Wurtzite structure model of ZnO emphasizing the tetrahedral coordination; (b) Schematic showing the piezoelectric effect in a tetrahedral-coordinated cation-anion unit [12].

2.2 Nanowires

One-dimensional nanomaterials with two physical dimensions in the range of 1-100 nm and a larger third dimension, are of interest in both academia and industry because of their potential as building blocks for other hierarchical structures and implantation into nanodevices. Three main types, classified according to their cross-sectional geometry, include nanotubes (NTs), nanowires (NWs), and nanobelts (NBs). Nanorods (NRs) are a subset of NWs (aspect ratios < 100). NRs and NWs will be the main topic of discussion in this thesis.

To achieve single-crystalline NWs, vapor-phase and solution-phase growth are the most dominant approaches. Vapor phase growth methods such as chemical vapor deposition (CVD), physical vapor deposition (PVD), molecular beam epitaxy (MBE), and pulsed laser deposition (PLD) have been well developed and often used for metal and metal oxide NW synthesis with high quality results.

2.2.1 Vapor Phase Synthesis

The first report of one-dimensional semiconducting single crystal structures dates back to 1964 when Wagner and Ellis successfully synthesized Si whiskers with diameters up to the micrometer scale through the vapor-liquid-solid(VLS) mechanism at 950 ºC [13]. Westwater et al. [14] and Lieber et al. [15] went on to further develop the VLS growth mechanism in the late 1990s and synthesize nanometer scale Si wires. High temperature catalyst-assisted vapor transport growth of one-dimensional nanowires usually follows the VLS mechanism. A metal catalyst forms a liquid alloy with the nanowire component under the reaction conditions. The liquid droplet serves as a preferential site for absorption of the gas phase reactant and the nucleation site for

crystallization when supersaturated. Nanowire growth begins after the liquid becomes supersaturated in reactant materials and continues as long as the catalyst alloy remains in a liquid state and the reactant is available [16].

ZnO is traditionally synthesized at high temperatures (450 - 900 ºC) in the gas phase. Huang et al. first reported the VLS catalytic growth of ZnO nanowires by vapor transport using an Au catalyst on Si substrates [17]. Others used catalyst-free vapor-solid (VS) processes such as metal-organic chemical vapor deposition (MOCVD) [18, 19]. These methods can produce high quality, single-crystalline nanowires with high aspect ratios, but are limited in terms of sample uniformity, low product yield, and substrate choice. Epitaxial substrates are typically required to minimize lattice mismatch.

2.2.2 Solution Phase Synthesis

Compared to the vapor phase synthesis approach, solution phase techniques have many advantages such as scalability, low-cost, and easy of handling. Additionally, solution phase synthesis methods allow for a greater choice of substrates, including both inorganic and organic substrates, since solution phase reactions occur at relatively low temperatures (25–200˚C) compared to those in the vapor phase (>450˚C). Solution phase approaches have been successfully implemented for NW materials systems such as TiO_2 [20], ZnO [21, 22], and CdTe [23] as well as complex oxides such as $BaTiO_3$ [24] which are particularly difficult to achieve by vapor phase synthesis.

Mild, wet chemical methods at low temperatures (< 100 ^{o}C) are one of the most attractive solution phase routes [21]. The reaction system employing hexamethylenetetramine (HMTA) and soluble zinc salts has been extensively explored to synthesize ZnO nanowires (see Table 2.1). Early reports by Andres et al. showed that

HMTA and $Zn(NO_3)_2$ or $ZnCl_2$ could be used to synthesize ZnO NRs at temperatures below 100 ^oC for relatively short reaction periods of c.a. 0.5 hr. It was suggested for the first time that preferential growth along the c-axis was responsible for the 1D morphology.

Govender et al. studied solution grown ZnO NR synthesis in detail including factors such as choice of complexing ligand and Zn counter-ion effect [25]. It is known that weak bases such as amines hydrolyze in aqueous Zn environments and slowly release hydroxide ions which form various Zn-hydroxide complexes. When ethylenediamine (EN) was used as the weak base, at low zinc concentration and high hydroxide concentration, rod-shape morphology resulted regardless of the Zn counter-ions. When triethanolamine (TEA) was used, only particles and no rods resulted. However, when HMTA was used, high-quality ZnO NRs resulted. The synthesis was successful only at high concentrations of free zinc and low concentrations of hydroxide, contradictory to that of EN as a ligand. The counter-ion effects were also investigated. Zinc salts including acetates, formates, nitrates, perchlorates, and chlorides all resulted in rod-like morphology except zinc sulfate which produced large, flat hexagonal platelets. Other reaction systems have also been studied to synthesize ZnO nanorods at low temperatures. For example, polyethylene glycol and ammonia were added drop-wise into an aqueous solution of zinc nitrate at room temperature and the final mixture was heated to temperatures ranging from 60 to 90 ^oC under stirring in an unsealed reactor. It was found that the diameter of the as-synthesized NRs increased with temperature [26]. Additionally, ZnO NRs were synthesized from aqueous zinc nitrate and ammonia with zinc metal acting as seeds at temperatures ranging from 60 to 90 ^oC [27].

Table 2.1 Summary of different results and methods for aqueous solution growth of ZnO nanorods and nanowires. Adapted from [28]

Growth Solution	Resulting Morphology	Focus of Investigation
Zinc nitrate, HMTA	Nanorods, microtubes	On Si and conducting glass substrates [22, 29]
Zinc nitrate, HMTA	Nanorods, nanotubes	Influence of substrate and seed layer [30]
Zinc nitrate, HMTA	Aligned nanowire arrays	Influence of seed layer [31]
Zinc-nitrate, HMTA, citrate	Oriented nanocolumns, nanoplates	Control of aspect ratio: addition of citrate anions decreases aspect ratio [32]
Zinc nitrate, zinc acetate, HMTA	Highly aligned nanorods	Influence of substrate and seed layer [33]
Zinc nitrate, triethanolamine, HCl (pH 5)	Ordered nanorods	Influence of substrate and counter ions in growth solution [34]
Zinc nitrate, thiourea, ammonium chloride, ammonia	Nanowires, tower- like, flower-like, tube-like	Influence of reactants, substrate pretreatment, and growth time and temperature [35]
Zinc acetate, sodium hydroxide, citric acid	Disk-like, flower- like, nanorods	Influence of pH on growth solution [36]
Comparison of different growth solutions	Star-like, nanorods	Influence of reaction conditions: ligand, counter-ions, pH, ionic strength, and deposition time Influence of substrate/ seed layer [25]
Zn foil, zinc sulfate, ammonium ions, sodium hydroxide	Nanobelt arrays, ordered nanowires	Influence of temperature and concentration of solutions [37, 38]

Hydrothermal synthesis, typically carried out at elevated temperatures and pressures in a Teflon-sealed stainless steel autoclave, another popular solution phase route for achieving ZnO nanowires. For example, ZnO NRs were prepared through the hydrolysis of a $ZnCO_3$ complex at temperatures between 160 - 200 ^oC [39]. The NRs exhibited an a-axis preferred growth direction, contrary to the commonly reported c-axis growth direction. Additionally, ZnO NRs were realized via a hydrothermal method using $ZnCl_2$, Na_2CO_3, and sodium dodecyl sulfonate (SDSN) in a Telfon-lined stainless steel autoclave at 140 ^oC for 12 hrs [40]. The Na_2CO_3 amount affected the final morphology such that the NR diameter decreased with the added amount of Na_2CO_3 since the CO_3^{2-}

could preferentially adsorb on the a-planes thereby suppressing growth on those surfaces. In a third example, ZnO nanorods with diameters less than 50 nm were synthesized using an ethylenediamine capping agent [41]. Molar ratios of 1:20 $Zn(NO_3)_2$ and NaOH were mixed to form zinc complex precursors in pure alcohol with an ethylenediamine (Zn^{2+}:EDA =1:50 or 60) capping agent. After sonication treatment, the mixture was hydrothermally treated at 180 °C for 20 hrs. The NRs had diameters of 45 nm and lengths of 1.5 μm with aspect ratios as high as 30-40. It was found that the ultrasonic treatment during the nucleation stage significantly affected the final NR structure since it likely generated many ZnO nuclei clusters. Without this treatment, only large diameter rods with low aspect ratios were observed.

Reaction media significantly effects nanomaterial growth. Solubility, viscosity, polarity, and surface energy are important parameters to consider when selecting a solvent system. Solubility and polarity directly influence supersaturation, a key parameter for nucleation and crystal growth. Viscosity may affect the mass transport in the reaction. It has been reported that ZnO nanoparticle growth was controlled through the selection of reaction media [42]. Strong alkaline conditions can ensure that Zn exists in an ionized state, making it more facile to diffuse to nanocrystal growth fronts in the solvent.

By using various capping agents in the solution synthesis process, the morphology of 1D ZnO NMs can be rationally controlled. Platelet-like morphology was reported when $ZnSO_4$ was used in conjunction with the hexamethylenetetramine (HMTA) reaction system [25]. In addition to NRs and platelets, ZnO nanotubes (NTs) have also been synthesized in solution [43]. To achieve NTs, ZnO NRs were first synthesized at 90 °C from the zinc nitrate and hexamethylenetetramine (HMTA) reaction system and

subsequently converted to NTs. Vayssieres et al. explained the NT formation in terms of selective dissolution of the metastable polar (0002) face of the ZnO NR [44]. Recent studies have attributed the dissolution of the polar facet a screw dislocation [45]. Hou et al. also reported ZnO NT growth using a hydrothermal method [46]. A mixture of zinc acetate, CTAB, and ammonia acting as a pH modifier (pH 10) was reacted at 140 ^{o}C for 12 hrs. The authors proposed different growth mechanisms for tubular and rod formation. For tubular morphology, ZnO seed crystals likely formed from the dehydration of $Zn(NH_3)_4^{2+}$ under conditions of high ammonia concentration. CTAB likely functioned as a structure directing agent along a preferred direction starting from the seed crystal to directly form NTs. No tubular structures were found when NaOH was substituted for NH_3 as the pH modifier indicating that ammonia acted not only as a pH modifier, but also a critical factor for achieving NT morphology. CTAB also played a critical role in the tubular morphology since other surfactants such as sodium dodecyl benzene sulphonate (SDBS) and sodium dodecyl sulfate (SDS) did not produce NTs under the same experimental conditions.

2.3 Photovoltaic Theory

The evolution and best solar cell efficiencies can be seen in Figure 2.5. Technology development of first generation photovoltaics based on crystalline Si is fully matured and manufacturing scale devices ship with efficiencies 18-20% [47]. In an effort to minimize the high material costs associated with high purity Si, second generation thin film solar cells based on amorphous Si, CdTe, and $CuInSe_2$ are beginning to reach the market place and show moderate efficiencies in the range of 8-12% [47]. Third generation devices based on multijunction concentrators have reached efficiencies above

40% [47], but processing costs limit their terrestrial applications. The goal of second and third generation photovoltaic devices seek to maximize conversion efficiencies while minimizing processing costs to achieve the $1/watt goal which represents the economic benchmark when PV is cost competitive with fossil fuel energy sources. To achieve this, the Shockley-Quisser limit for single bandgap absorbers must be overcome and nanomaterials such as nanowires and nanoparticles will play a crucial role.

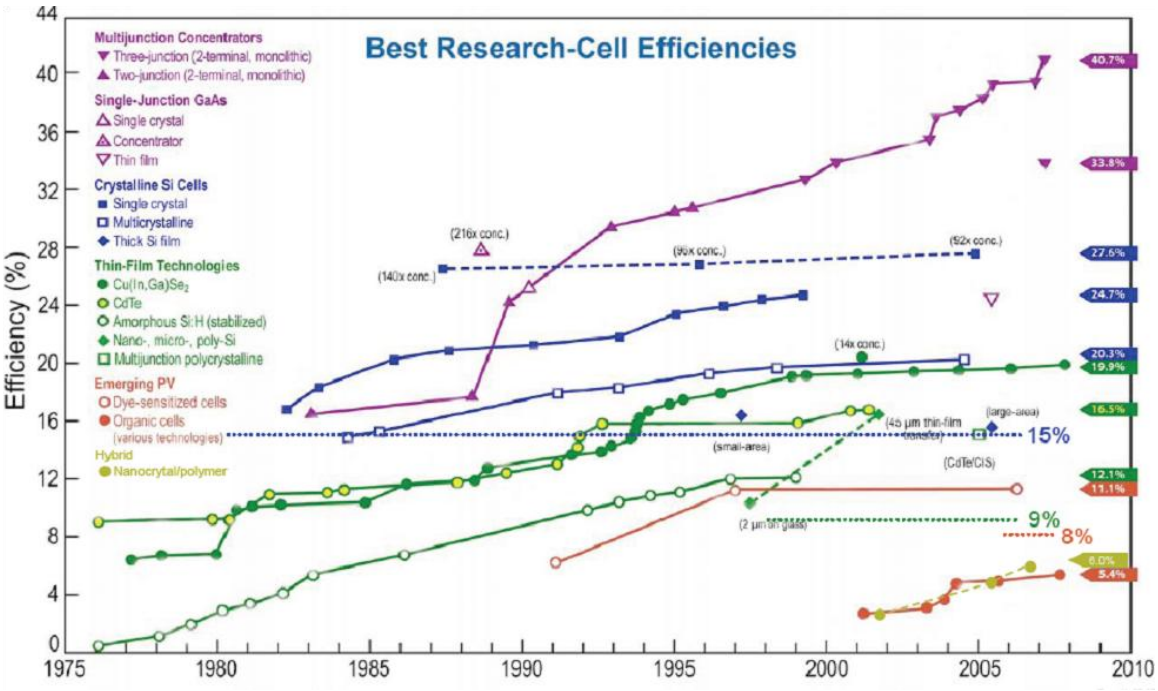

Figure 2.5 Best research solar cell efficiencies. [47]

2.3.1 Theoretical Efficiency limits

In the famous work by Shockley and Queisser, they theorized that the semiconductor bandgap dictates the p-n junction solar cell efficiency [48]. They predicted that the maximum power conversion efficiency of 30% at 1 sun corresponded to a 1.2 eV bandgap. In terms of energy loss, incoming photons whose energy are above the bandgap are lost to heating and those whose energy are below the band gap pass

through and are not absorbed. In the work, they assumed the following: the sun is a blackbody at 6000 K, the solar cell is a blackbody at 300 K and uniform in temperature, the active region is thick enough to absorb all light above the band gap, one photon gives rise to one electron-hole pair, all recombination is via radiative processes, all photoexcited carrier pairs that do not recombine radiatively are extracted, and all excited carriers relax to the band edge prior to extraction, relaxation is by creating phonons. The Shockley-Queisser approach is useful for theorizing first generation (bulk crystalline) and second generation (thin film) photovoltaics. That being said, one of the goals of third generation photovoltaics is to overcome the Shockley-Queisser limits imposed on single bandgap absorbers.

2.3.2 Testing Standards

To simulate solar radiation and characterize the performance of photovoltaic devices in a controlled laboratory environment, there are a number of important considerations. The first consideration is the emissive light power distribution. The sun is approximated as a blackbody radiating at a temperature of 6000 K and the emissive power radiation as a function of wavelength is characterized by Plank's radiation formula. This is the light power distribution experience by objects in outside the earth's atmosphere refered to as air mass (AM) 0 distribution. However, to account for the light scattering and absorption losses associated with earth's atmosphere, the AM 1.5 is established to account for the path length that light travels in earth's atmosphere and is defined as:

$$AM = \frac{1}{\cos\theta} \tag{1}$$

Θ is the angle between a light ray at noon and the zenith angle of the sun at a given time. Under AM 1.5 standard conditions, $\Theta = 48.2^{\circ}$. The air mass concept accounts for the selective absorption at particular wavelengths of light due to various atmospheric species (O_3, H_2O, CO_2).

2.3.3 Dye-sensitized Solar Cells

Among the various third generation PV approaches such as all organic and multijunction, dye-sensitized solar cells (DSSCs) are considered a promising technology because of their low processing costs and moderate efficiencies. DSSCs are photovoltaic devices in which light absorption and charge carrier transport are controlled separately. A photosensitizing dye anchored to a high surface area wide bandgap semiconductor absorbs the light while photogenerated electrons are transported through the semiconductor and holes through a redox electrolyte (see Figure 2.6). Typically, TiO_2 nanoparticles are sintered to form a mesoporous film with roughness factors of 1000. The iodine-based electrolyte forms a second phase interspersed within the TiO_2 phase to form a hole transport medium by way of a redox reaction. Reaction (2) takes place at the photoanode to replenish the electron deficient dye and reaction (3) takes place at the Pt cathode counter electrode.

$$3I^- \rightarrow I_3^- + 2e^- \quad (2)$$

$$I_3^- + 2e^- \rightarrow 3I^- \quad (3)$$

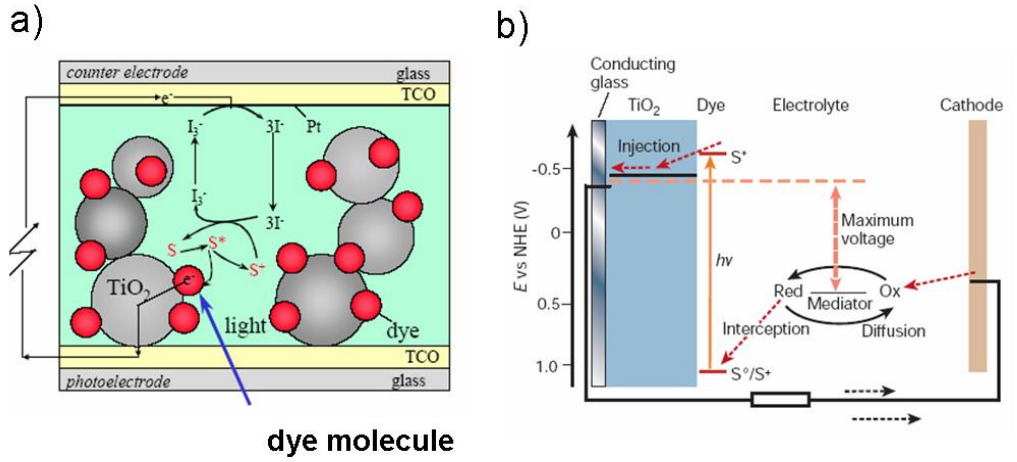

Figure 2.6 (a) Design of a traditional TiO_2 nanoparticle DSSC; (b) Energy diagram depicting the theory of a dye-sensitized solar cell [49]

There are a number of loss mechanisms in a DSSC. 1) the excited dye can decay before it injects an electron; 2) the injected electron can recombine with the oxidized dye before the dye is regenerated; or 3) the redox shuttle can intercept an electron from the photoanode before it is collected [50].

Compared to traditional TiO_2 nanoparticle films, ZnO nanowire arrays are considered promising photoanode material alternatives because of their highly controllable 1D single-crystalline nanoscale morphology which can provide direct electron transport pathways for photogenerated electrons (see figure 2.7). Well-oriented, high aspect ratio crystalline ZnO NWs were synthesized hydrothermally and DSSCs were fabricated [51]. The high crystallinity and internal electric field resulted in good electron transport within the nanowire photoanode and effective carrier collection. At 1 sun illumination intensity, the ZnO NW DSSC yielded the following performance: short-circuit current density (J_{sc}) 5.3-5.85 mA cm^{-2}, open circuit voltage (V_{oc}) 0.61-0.71 V, fill factor (FF) 0.36-0.38 and total efficiency (η) 1.2-1.5%. The overall conversion efficiency was limited primarily by low nanowire surface area which reduced dye loading.

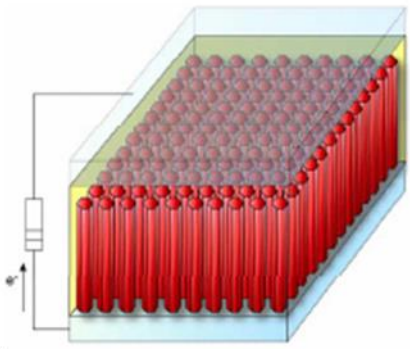

Figure 2.7 Schematic of a nanowire-based dye-sensitized solar cell [51]

The type and properties of dyes affect the DSSC performance. Wu et al. studied the effects of dye adsorption on the electron transport properties in ZnO-nanowire DSSCs and suggested that the mercurochrome dyes are more appropriate than ruthenium complex dyes because N3-sensitized ZnO photoanodes exhibited a higher surface trap density.[143] Recently, He et. al. investigated the electron transport and recombination properties of hydrothermally-synthesized ZnO nanorod based DSSCs using electrochemical impedance spectroscopy (EIS).[144] They pointed out that the recombination at the ZnO-electrolyte interface occurs via electron transfer from surface trap states and device performance is greatly influenced by the variation of recombination properties as a function of illumination intensity.

2.3.4 ZnO Nanostructured solar cell designs

Hybrid photovoltaic devices consisting of a π–conjugated polymer and a metal oxide semiconductor have also attracted significant attention. Olson et al. fabricated hybrid photovoltaic devices by infiltrating poly(3-hexylthiophene) (P3HT) or P3HT/ (6,6)-phenyl C_{61} butyric acid methyl ester (PCBM) into solution-synthesized ZnO nanofibers [52].

Due to its wide band gap, ZnO cannot absorb in the visible region of the solar spectrum (> 420 nm). Therefore, hybrid ZnO solar cell devices employing organic dye molecules [53], inorganic quantum dots [54] and nanoparticles [55] which effectively absorb in the visible and IR regions are of interest for efficient energy harvesting. The charge injection efficiency of hybrid P3HT/PCBM/ZnO solar cells processed with and without N719 dye was compared and it was and found that both the short circuit current density and the efficiency were higher with the dye [53]. In the CdSe quantum dot-sensitized ZnO nanowire solar cell reported by Leschkies et. al., the photocurrent generated from the visible light was due to the electron-hole pairs created in the CdSe quantum dots, followed by electron injection into the ZnO nanowires [54]. Chen et al. reported a Au nanoparticle-sensitized ZnO nanorod solar cell where the Au nanoparticles enhanced the absorption of visible light through surface plasmon resonance and the schottky barrier at the ZnO/Au interface reduced electron-hole recombination, which ultimately led to improved efficiency [55]. Others have fabricated core-shell heterostructures to optimize surface chemistry. For example, Plank et. al. fabricated ZnO-MgO core-shell based solid-state DSSCs and observed a five-fold efficiency improvement compared to pristine ZnO nanowire based photovoltaic devices [56]. Greene et al. found that the efficiency of P3HT/ZnO nanorod solar cells could be improved five-fold by a thin TiO_2 shell on the ZnO nanorod arrays [57]. Enhancing light coupling into the active region of the photovoltaic devices is another way to improve efficiency by adding anti-reflective coatings to minimize reflectance losses. ZnO is regarded as a good dielectric anti-reflective coating material due to its high transparency and appropriate refractive index (n=2) and solution-synthesized ZnO nanorod arrays have

been employed as efficient solar cell anti-reflective coatings to enhance solar cell performance [58].

Flexible solar cells based on nanostructured metal oxides have attracted increasing interest due to the potentially light weight, thin, and bendable advantages. A dye-sensitized solar cell based on hydrothermally grown ZnO nanowire films on flexible PET/ITO substrates was reported [59]. ZnO nanoparticles were attached to ZnO nanowire surfaces to further increase the surface area and the results showed promising device stability.

2.4 References

[1] U. Ozgur, Y. I. Alivov, C. Liu, A. Teke, M. A. Reshchikov, S. Dogan, V. Avrutin, S. J. Cho, and H. Morkoc, "A comprehensive review of ZnO materials and devices," *Journal of Applied Physics,* vol. 98, pp. -, Aug 15 2005.

[2] M. H. Huang, S. Mao, H. Feick, H. Q. Yan, Y. Y. Wu, H. Kind, E. Weber, R. Russo, and P. D. Yang, "Room-temperature ultraviolet nanowire nanolasers," *Science,* vol. 292, pp. 1897-1899, Jun 8 2001.

[3] S. F. J. Cox, E. A. Davis, S. P. Cottrell, P. J. C. King, J. S. Lord, J. M. Gil, H. V. Alberto, R. C. Vilao, J. P. Duarte, N. A. de Campos, A. Weidinger, R. L. Lichti, and S. J. C. Irvine, "Experimental confirmation of the predicted shallow donor hydrogen state in zinc oxide," *Physical Review Letters,* vol. 86, pp. 2601-2604, Mar 19 2001.

[4] D. M. Hofmann, A. Hofstaetter, F. Leiter, H. J. Zhou, F. Henecker, B. K. Meyer, S. B. Orlinskii, J. Schmidt, and P. G. Baranov, "Hydrogen: A relevant shallow donor in zinc oxide," *Physical Review Letters,* vol. 88, pp. -, Jan 28 2002.

[5] A. R. Hutson, "Hall Effect Studies of Doped Zinc Oxide Single Crystals," *Physical Review,* vol. 108, pp. 222-230, 1957.

[6] B. J. Jin, S. H. Bae, S. Y. Lee, and S. Im, "Effects of native defects on optical and electrical properties of ZnO prepared by pulsed laser deposition," *Materials Science and Engineering B-Solid State Materials for Advanced Technology,* vol. 71, pp. 301-305, Feb 14 2000.

[7] D. C. Look, J. W. Hemsky, and J. R. Sizelove, "Residual native shallow donor in ZnO," *Physical Review Letters,* vol. 82, pp. 2552-2555, Mar 22 1999.

[8] C. G. Van De Walle, "Strategies for controlling the conductivity of wide-band-gap semiconductors," *Physica Status Solidi B-Basic Research,* vol. 229, pp. 221-228, Jan 2002.

[9] D. I. Florescu, L. G. Mourokh, F. H. Pollak, D. C. Look, G. Cantwell, and X. Li, "High spatial resolution thermal conductivity of bulk ZnO (0001)," *Journal of Applied Physics,* vol. 91, pp. 890-892, Jan 15 2002.

[10] F. A. Kröger, *The Chemistry of Imperfect Crystals*, 2nd Edition ed. vol. 73. North Holland, Amsterdam, 1974.

[11] M. H. Zhao, Z. L. Wang, and S. X. Mao, "Piezoelectric characterization of individual zinc oxide nanobelt probed by piezoresponse force microscope," *Nano Letters,* vol. 4, pp. 587-590, Apr 2004.

[12] Z. L. Wang, X. Y. Kong, Y. Ding, P. X. Gao, W. L. Hughes, R. S. Yang, and Y. Zhang, "Semiconducting and piezoelectric oxide nanostructures induced by polar surfaces," *Advanced Functional Materials,* vol. 14, pp. 943-956, Oct 2004.

[13] R. S. Wagner and W. C. Ellis, "Vapor-Liquid-Solid Mechanism of Single Crystal Growth (New Method Growth Catalysis from Impurity Whisker Epitaxial + Large Crystals Si E)," *Applied Physics Letters,* vol. 4, pp. 89-&, 1964.

[14] J. Westwater, D. P. Gosain, S. Tomiya, S. Usui, and H. Ruda, "Growth of silicon nanowires via gold/silane vapor-liquid-solid reaction," *Journal of Vacuum Science & Technology B,* vol. 15, pp. 554-557, May-Jun 1997.

[15] A. M. Morales and C. M. Lieber, "A laser ablation method for the synthesis of crystalline semiconductor nanowires," *Science,* vol. 279, pp. 208-211, Jan 9 1998.

[16] Z. L. Wang, "Zinc oxide nanostructures: growth, properties and applications," *Journal of Physics-Condensed Matter,* vol. 16, pp. R829-R858, Jun 30 2004.

[17] Y. Huang, X. F. Duan, Y. Cui, L. J. Lauhon, K. H. Kim, and C. M. Lieber, "Logic gates and computation from assembled nanowire building blocks," *Science,* vol. 294, pp. 1313-1317, Nov 9 2001.

[18] W. I. Park, G. C. Yi, M. Y. Kim, and S. J. Pennycook, "ZnO nanoneedles grown vertically on Si substrates by non-catalytic vapor-phase epitaxy," *Advanced Materials,* vol. 14, pp. 1841-1843, Dec 17 2002.

[19] J. J. Wu, S. C. Liu, C. T. Wu, K. H. Chen, and L. C. Chen, "Heterostructures of ZnO-Zn coaxial nanocables and ZnO nanotubes," *Applied Physics Letters,* vol. 81, pp. 1312-1314, Aug 12 2002.

[20] X. J. Feng, K. Shankar, O. K. Varghese, M. Paulose, T. J. Latempa, and C. A. Grimes, "Vertically Aligned Single Crystal TiO2 Nanowire Arrays Grown Directly on Transparent Conducting Oxide Coated Glass: Synthesis Details and Applications," *Nano Letters,* vol. 8, pp. 3781-3786, Nov 2008.

[21] M. A. Verges, A. Mifsud, and C. J. Serna, "Formation of Rod-Like Zinc-Oxide Microcrystals in Homogeneous Solutions," *Journal of the Chemical Society-Faraday Transactions,* vol. 86, pp. 959-963, Mar 21 1990.

[22] L. Vayssieres, "Growth of arrayed nanorods and nanowires of ZnO from aqueous solutions," *Advanced Materials,* vol. 15, pp. 464-466, Mar 4 2003.

[23] A. L. Rogach, T. Franzl, T. A. Klar, J. Feldmann, N. Gaponik, V. Lesnyak, A. Shavel, A. Eychmuller, Y. P. Rakovich, and J. F. Donegan, "Aqueous synthesis of

thiol-capped CdTe nanocrystals: State-of-the-art," *Journal of Physical Chemistry C,* vol. 111, pp. 14628-14637, Oct 11 2007.

[24] Z. Y. Wang, J. Hu, A. P. Suryavanshi, K. Yum, and M. F. Yu, "Voltage generation from individual BaTiO3 nanowires under periodic tensile mechanical load," *Nano Letters,* vol. 7, pp. 2966-2969, Oct 2007.

[25] K. Govender, D. S. Boyle, P. B. Kenway, and P. O'Brien, "Understanding the factors that govern the deposition and morphology of thin films of ZnO from aqueous solution," *Journal of Materials Chemistry,* vol. 14, pp. 2575-2591, 2004.

[26] H. X. Zhang, J. Feng, J. Wang, and M. L. Zhang, "Preparation of ZnO nanorods through wet chemical method," *Materials Letters,* vol. 61, pp. 5202-5205, Dec 2007.

[27] Y. Tak and K. J. Yong, "Controlled growth of well-aligned ZnO nanorod array using a novel solution method," *Journal of Physical Chemistry B,* vol. 109, pp. 19263-19269, Oct 20 2005.

[28] L. S. Mende and J. L. MacManus-Driscoll, "ZnO – nanostructures, defects, and devices," *Materials Today,* vol. 10, pp. 40-48, May 2007 2007.

[29] L. Vayssieres, K. Keis, S. E. Lindquist, and A. Hagfeldt, "Purpose-built anisotropic metal oxide material: 3D highly oriented microrod array of ZnO," *Journal of Physical Chemistry B,* vol. 105, pp. 3350-3352, May 3 2001.

[30] Y. Sun, D. J. Riley, and M. N. R. Ashfold, "Mechanism of ZnO nanotube growth by hydrothermal methods on ZnO film-coated Si substrates," *Journal of Physical Chemistry B,* vol. 110, pp. 15186-15192, Aug 10 2006.

[31] L. E. Greene, M. Law, D. H. Tan, M. Montano, J. Goldberger, G. Somorjai, and P. D. Yang, "General route to vertical ZnO nanowire arrays using textured ZnO seeds," *Nano Letters,* vol. 5, pp. 1231-1236, Jul 2005.

[32] Z. R. R. Tian, J. A. Voigt, J. Liu, B. McKenzie, M. J. McDermott, M. A. Rodriguez, H. Konishi, and H. F. Xu, "Complex and oriented ZnO nanostructures," *Nature Materials,* vol. 2, pp. 821-826, Dec 2003.

[33] Z. T. Chen and L. Gao, "A facile route to ZnO nanorod arrays using wet chemical method," *Journal of Crystal Growth,* vol. 293, pp. 522-527, Aug 1 2006.

[34] D. S. Boyle, K. Govender, and P. O'Brien, "Novel low temperature solution deposition of perpendicularly oriented rods of ZnO: substrate effects and evidence of the importance of counter-ions in the control of crystallite growth (vol 15, pg 80, 2002)," *Chemical Communications,* pp. 1651-1651, 2002.

[35] Z. Wang, X. F. Qian, J. Yin, and Z. K. Zhu, "Large-scale fabrication of tower-like, flower-like, and tube-like ZnO arrays by a simple chemical solution route," *Langmuir,* vol. 20, pp. 3441-3448, Apr 13 2004.

[36] M. L. Zhang, G. Y. Sheng, J. M. Fu, T. C. An, X. M. Wang, and X. H. Hu, "Novel preparation of nanosized ZnO-SnO2 with high photocatalytic activity by homogeneous co-precipitation method," *Materials Letters,* vol. 59, pp. 3641-3644, Dec 2005.

[37] F. Xu, Z. Y. Yuan, G. H. Du, T. Z. Ren, C. Volcke, P. Thiry, and B. L. Su, "A low-temperature aqueous solution route to large-scale growth of ZnO nanowire arrays," *Journal of Non-Crystalline Solids,* vol. 352, pp. 2569-2574, Jul 15 2006.

[38] C. H. Lu, L. M. Qi, J. H. Yang, L. Tang, D. Y. Zhang, and J. M. Ma, "Hydrothermal growth of large-scale micropatterned arrays of ultralong ZnO nanowires and nanobelts on zinc substrate," *Chemical Communications,* pp. 3551-3553, 2006.

[39] J. M. Wang and L. Gao, "Wet chemical synthesis of ultralong and straight single-crystalline ZnO nanowires and their excellent UV emission properties," *Journal of Materials Chemistry,* vol. 13, pp. 2551-2554, 2003.

[40] H. M. Hu, X. H. Huang, C. H. Deng, X. Y. Chen, and Y. T. Qian, "Hydrothermal synthesis of ZnO nanowires and nanobelts on a large scale," *Materials Chemistry and Physics,* vol. 106, pp. 58-62, Nov 15 2007.

[41] B. Liu and H. C. Zeng, "Hydrothermal synthesis of ZnO nanorods in the diameter regime of 50 nm," *Journal of the American Chemical Society,* vol. 125, pp. 4430-4431, Apr 16 2003.

[42] Z. S. Hu, G. Oskam, and P. C. Searson, "Influence of solvent on the growth of ZnO nanoparticles," *Journal of Colloid and Interface Science,* vol. 263, pp. 454-460, Jul 15 2003.

[43] Y. Sun, G. M. Fuge, N. A. Fox, D. J. Riley, and M. N. R. Ashfold, "Synthesis of aligned arrays of ultrathin ZnO nanotubes on a Si wafer coated with a thin ZnO film," *Advanced Materials,* vol. 17, pp. 2477-+, Oct 17 2005.

[44] L. Vayssieres, N. Beermann, S. E. Lindquist, and A. Hagfeldt, "Controlled aqueous chemical growth of oriented three-dimensional crystalline nanorod arrays: Application to iron(III) oxides," *Chemistry of Materials,* vol. 13, pp. 233-235, Feb 2001.

[45] M. J. B. S.A. Morin, J. Tong, S. Jin, "Mechanism and Kinetics of Spontaneous Nanotube Growth Driven by Screw Dislocations," *Science,* vol. 328, pp. 476-480, 2010.

[46] H. W. Hou, Y. Xie, and Q. Li, "Structure-directing self-organized, one-dimensional ZnO single-crystal whiskers," *Solid State Sciences,* vol. 7, pp. 45-51, Jan 2005.

[47] http://www.nrel.gov/pv/thin_film/pn_general_interest.html, downloaded May 2010.

[48] W. Shockley and H. J. Queisser, "Detailed Balance Limit of Efficiency of P-N Junction Solar Cells," *Journal of Applied Physics,* vol. 32, pp. 510-&, 1961.

[49] M. Gratzel, "Photoelectrochemical cells," *Nature,* vol. 414, pp. 338-344, Nov 15 2001.

[50] T. W. Hamann, Jensen,R. A., Martinson, A. B. F., Ryswyk, H. V., Hupp, J. T. , "Advancing beyond current generation dye-sensitized solar cells," *Energy and Environmental Science,* vol. 1, pp. 66-78, 2008.

[51] M. Law, L. E. Greene, J. C. Johnson, R. Saykally, and P. D. Yang, "Nanowire dye-sensitized solar cells," *Nature Materials,* vol. 4, pp. 455-459, Jun 2005.

[52] D. C. Olson, Piris, J., Collins, R. T., Shaheen, S. E., Ginley, D. S., "Hybrid photovoltaic devices of polymer and ZnO nanofiber composites " *Thin Solid Films,* vol. 496, pp. 26-29 2006.

[53] R. Thitima, C. Patcharee, S. Takashi, and Y. Susumu, "Efficient electron transfers in ZnO nanorod arrays with N719 dye for hybrid solar cells," *Solid-State Electronics,* vol. 53, pp. 176-180, Feb 2009.

[54] K. S. Leschkies, R. Divakar, J. Basu, E. Enache-Pommer, J. E. Boercker, C. B. Carter, U. R. Kortshagen, D. J. Norris, and E. S. Aydil, "Photosensitization of ZnO nanowires with CdSe quantum dots for photovoltaic devices," *Nano Letters,* vol. 7, pp. 1793-1798, Jun 2007.

[55] Z. H. Chen, Y. B. Tang, C. P. Liu, Y. H. Leung, G. D. Yuan, L. M. Chen, Y. Q. Wang, I. Bello, J. A. Zapien, W. J. Zhang, C. S. Lee, and S. T. Lee, "Vertically Aligned ZnO Nanorod Arrays Sentisized with Gold Nanoparticles for Schottky Barrier Photovoltaic Cells," *Journal of Physical Chemistry C,* vol. 113, pp. 13433-13437, Jul 30 2009.

[56] N. O. V. Plank, H. J. Snaith, C. Ducati, J. S. Bendall, L. Schmidt-Mende, and M. E. Welland, "A simple low temperature synthesis route for ZnO-MgO core-shell nanowires," *Nanotechnology,* vol. 19, pp. -, Nov 19 2008.

[57] L. E. Green, Law, M., Yuhas, B. D., Yang, P. , "ZnO−TiO2 Core−Shell Nanorod/P3HT Solar Cells," *Journal of Physical Chemistry C,* vol. 111, p. 18451, 2007.

[58] Y. J. Lee, D. S. Ruby, D. W. Peters, B. B. McKenzie, and J. W. P. Hsu, "ZnO nanostructures as efficient antireflection layers in solar cells," *Nano Letters,* vol. 8, pp. 1501-1505, May 2008.

[59] C. Y. Jiang, X. W. Sun, K. W. Tan, G. Q. Lo, A. K. K. Kyaw, and D. L. Kwong, "High-bendability flexible dye-sensitized solar cell with a nanoparticle-modified ZnO-nanowire electrode," *Applied Physics Letters,* vol. 92, pp. -, Apr 7 2008.

CHAPTER 3

SOLUTION-PHASE ZINC OXIDE NANOWIRE SYNTHESIS

In the previous chapter, background was provided on one-dimensional nanomaterial synthesis, characterization, and applications in photovoltaics. In this chapter, experimental data are presented and discussed for solution-phase ZnO nanowire synthesis in terms of position, density, and orientation control.

3.1 Synthesis setup

ZnO nanowires can be successfully synthesized using vapor or solution phase approaches, however this thesis primarily focuses on a solution phase approach. Solution phase approaches based on the zinc nitrate and HMTA system can be carried out under relatively mild conditions (i.e. low temperature and pressure). Compared to high temperature vapor phase synthesis approaches, the low temperature pathway offers advantages of low cost, flexibility, possible in-situ investigations, and both inorganic and organic material compatibility. The general synthesis setup is shown in Figure 3.1. The system consists of a capped Pyrex glass bottle (50 - 500 ml) with 90% of the volume filled with precursor solution. In general, the substrates were positioned in three different locations depending on the synthesis requirements. The substrates were either floated face-down at the solution/gas interface by virtue of the surface tension of H_2O, fully immersed and fastened vertically to the bottom, or fully immersed and oriented diagonally against the Pyrex bottle sidewall.

Figure 3.2 shows a representative image of the synthesis setup. Optical fiber substrates are fully immersed in the precursor solution contained in a 250 mL capped

Pyrex vessel. In this example, the substrates are fastened to the top directly from the cap. However, the substrates can also be oriented vertically by fastening them to an anchor on the bottom of the vessel.

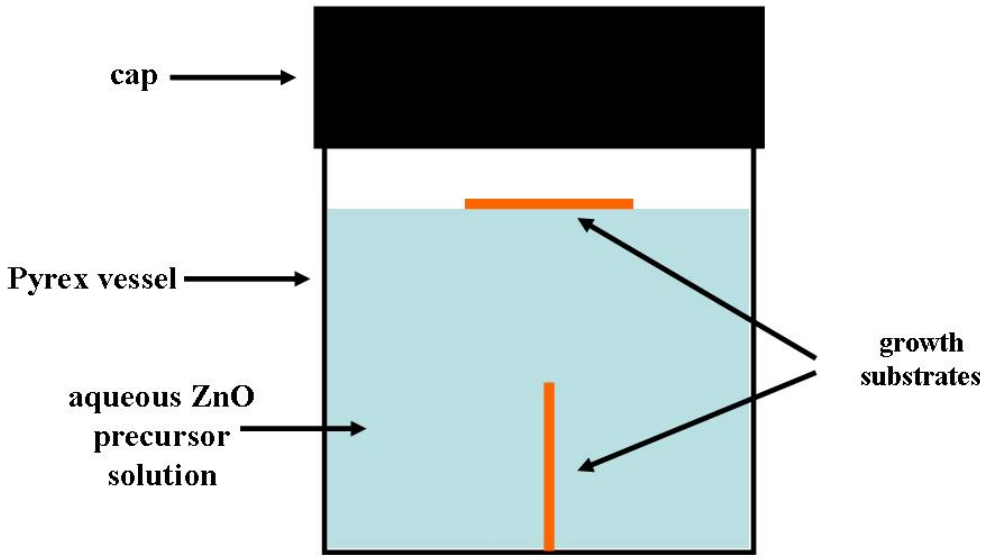

Figure 3.1 Schematic of synthesis setup

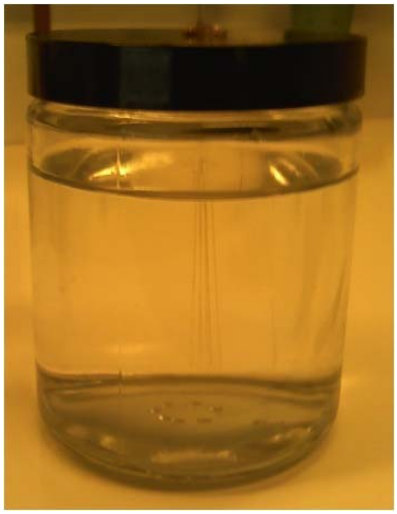

Figure 3.2 Solution-based synthesis vessel consisting of 250 mL Pyrex bottle filled with precursor solution.

The Pyrex vessel was placed inside a Yamato DKN400 mechanical convection box oven (see Figure 3.3) which uses a proportional-integral-derivative temperature microprocessor controller to maintain the temperature setpoint. The temperature was ramped to the setpoint and allowed to stabilize for 0.5 hr before introducing the reaction vessel.

Figure 3.3 Mechanical convection box oven (Yamato DKN400)

3.2 Growth Mechanism

Hydrothermal methods have been widely used for the synthesis of 1D nanomaterials. For ZnO, characterized by the wurtzite crystal structure, the main approach for achieving 1D growth is to exploit the difference in surface chemistry between the polar $\{0001\}$ and non-polar $\{10\bar{1}0\}$ and $\{11\bar{2}0\}$ facets. By selectively promoting or suppressing growth on these facets, rational 1D growth can be achieved from the bottom up. The dominant zinc species present varies in an aqueous system depending on the solution pH (see reactions (1)-(5)). The chemical equations are below:

$$Zn^{2+} + H_2O \leftrightarrow ZnO_{(s)} + 2H^+ \quad (1)$$

$$ZnOH^+ \leftrightarrow ZnO_{(s)} + H^+ \quad (2)$$

$$Zn(OH)_{2(aq)} \leftrightarrow ZnO_{(s)} + H_2O \quad (3)$$

$$Zn(OH)^{3-} + H^{+} \leftrightarrow ZnO_{(s)} + 2H_2O \quad (4)$$

$$Zn(OH)_4^{2-} + 2H^{+} \leftrightarrow ZnO_{(s)} + 3H_2O \quad (5)$$

The addition of amines to control the pH and morphology introduces additional zinc/amine complexes as outlined later in the chapter. Using thermodynamic solubility data, Yamabi et al. assembled stability phase diagrams to determine the dominant phase present as a function of zinc concentration and pH at room temperature (Figure 3.4) [1]. The dashed lines denotes the thermodynamic equilibria between the Zn soluble species and the ZnO solid phase. The boundaries were calculated on the basis of the equilibrium thermodynamic data. The solid lines represent the total concentration of the soluble species as a function of pH (i.e. the solubility of the solid phases). It can be noted that the soluble species are the dominant phase below pH 7 at 0.01 M Zn concentration.

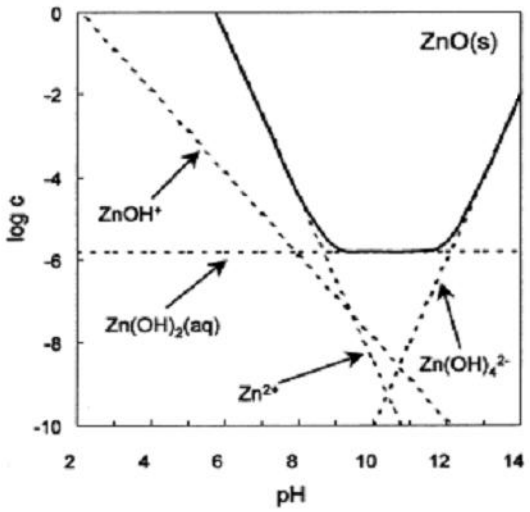

Figure 3.4 Thermodynamic phase diagram for $ZnO_{(s)}$-H_2O at 25 ˚C [1]

One of the key parameters for synthesizing 1D nanomaterials in solution is controlling the supersaturation (σ) of reactants, defined as:

$$\sigma = \ln \frac{c}{c_o} \tag{6}$$

where c and c_o are the concentration and the equilibrium concentration of the system, respectively [2]. In general, low reactant supersaturation levels favor 1D nanomaterial growth. In order to maintain low supersaturation levels during the growth process, the nutrient supply must be finely controlled. This is difficult for closed systems where the precursor supersaturation level is steadily decreasing with time and the concentration of soluble zinc species is slowly being depleted. The decrease in soluble zinc species as a function of time was measured by Song et. al. (see Figure 3.5) by heating a series of equimolar solutions of $Zn(NO_3)_2$ and hexamethylenetetramine (5 mM, 10 ml, at 95° C) in closed vials [3]. The reactions were stopped 15 minutes apart and the remaining concentration of soluble zinc species was measured using inductively coupled plasma atomic emission spectroscopy.

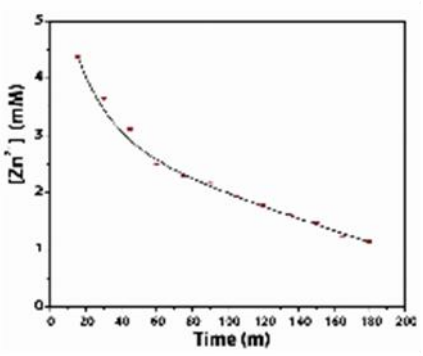

Figure 3.5 Decrease of soluble zinc species over time measured by inductively coupled plasma atomic emission spectroscopy. [3]

HMTA is commonly used in solution-based methods to synthesize ZnO NRs at low temperatures, however its detailed role is still an area of debate. It is generally accepted that HMTA acts as a pH buffer and slow, steady source of hydroxide ions. The

hydroxide ions further react with Zn^{2+} to form zinc complexes. The decomposition kinetics of HMTA into formaldehyde and ammonia have been investigated and found to be pH dependent [4]. Sugunan et. al. investigated the role of HMTA in the synthesis of ZnO NRs as well [5]. A seeded glass slide was immersed in a chemical bath containing equimolar zinc nitrate and HMTA between 60–95 ^{o}C for up to 24 hrs. FTIR in ATR mode was used to track the decomposition of HMTA by monitoring the changes in absorption due to stretching vibrations of the C–N bond as an indicator of HMTA degradation. Under the experimental conditions, HMTA was expected to slowly decompose to formaldehyde and ammonia, and the C-N bond vibrations measured in the IR spectra were expected to reduce over time. However, the IR spectra taken from the mixture after 1 hr reaction was almost identical to that taken after 5 hrs, strongly suggesting that no change in the tertiary amine structure had taken place. Furthermore, there was no significant difference in NR morphologies that were grown at different temperatures. Thus, the authors hypothesized that the formation of ZnO NRs with high aspect ratios could be explained by preferential adsorption of non-ionic HMTA on the non-polar, a-planes of the ZnO NRs. The role of HMTA can be understood schematically in Figure 3.6. The non-polar HMTA is preferentially adsorbing to the non-polar $\{10\bar{1}0\}$ and $\{11\bar{2}0\}$ facets and allowing the precursor zinc species access to the polar {0001} growth front facet.

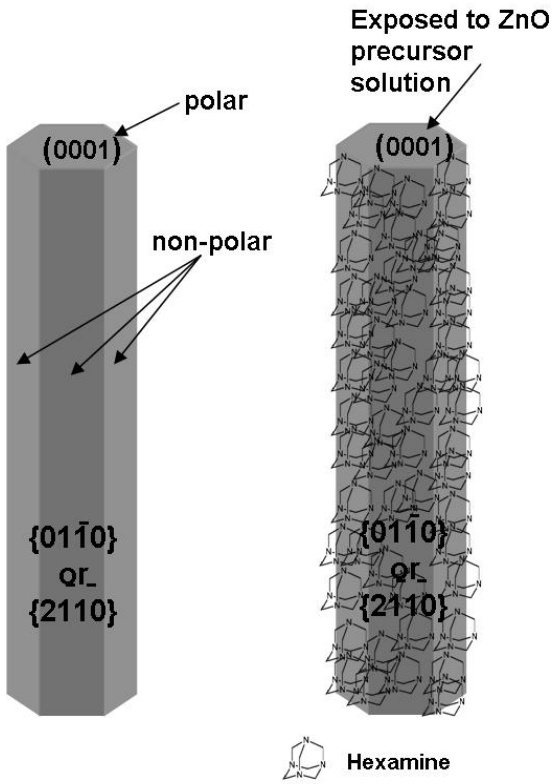

Figure 3.6 Schematic showing role of hexamethylenetetramine as a capping agent to promote 1-D growth

3.3 Position Control

In this section, the position-controlled, seedless growth of ZnO nanorod arrays on a polymer substrate via a wet chemical synthesis route will be described.

3.3.1 Introduction

Recently, there has been growing interest in ZnO nanorod arrays for applications in electronics and optoelectronics such as solar cells [6], UV lasers [7], nanogenerators [8, 9] , light emitting diodes [10], and field emission devices [11]. One-dimensional ZnO nanostructured arrays are typically synthesized in the gas phase catalytically using the vapor-liquid-solid process [12] on single crystal sapphire substrates and catalyst-free

using metal-organic chemical vapor deposition(MOCVD) [13, 14]. These methods produce high quality single crystal nanorods, but have strict substrate requirements due to the high synthesis temperature requirements (450 - 900 ºC) and are limited by sample uniformity. Wet chemical methods are an attractive alternative since they can be carried out at temperatures as low as 50 ºC and allow for a greater variety of crystalline and amorphous substrates [15-17].

Wet chemical growth can be achieved independent of the substrate by employing ZnO seeds in the form of thin films or nanoparticles. This approach typically requires higher temperature substrate processing. ZnO seeds must be annealed at 150 ºC to improve particle adhesion to the substrate, and ZnO nanorod vertical alignment could be further improved by textured ZnO seeds annealed at 350 ºC [18, 19]. However, there is interest in carrying out the entire process from substrate preparation to synthesis at low temperatures which would be compatible with organic substrates for applications in flexible and wearable electronics. ZnO nanorod arrays have been synthesized on polymer substrates such as polydimethylsiloxane (PDMS), Au coated Kapton, and polycarbonate coated with polystyrene beads [17, 18, 20]. As expected, the nanorods grew at random sites on the substrate surface.

Site-selective growth of ZnO nanorods is of interest for the integration of nanostructures into MEMS and NEMS devices. Nanosphere lithography has been employed to define Au catalyst patterns for ZnO nanowire arrays on single crystal sapphire [21]. Electron beam lithography was successfully utilized to define position and size-controlled micro and nanorods arrays on Si substrates covered with a ZnO thin film seed layer [22]. Photolithography techniques have been used to pattern micron-size

regions and enhance the growth with ZnO nanoparticle seeds [23]. Microstamped self-assembled monolayers (SAM) have also been employed to define ZnO micron-size patterned arrays [24].

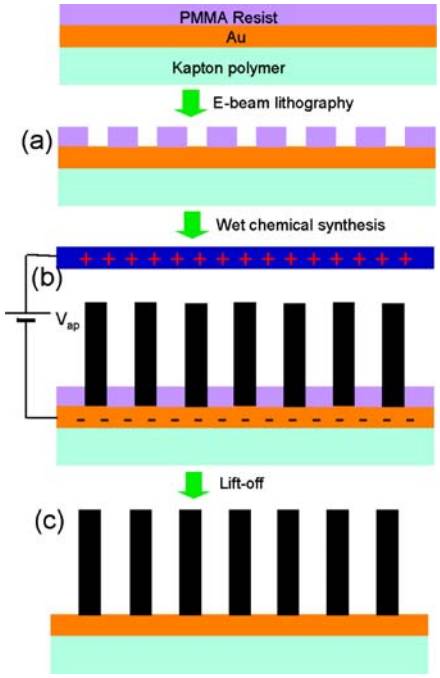

Figure 3.7 Process flow for lithography-based density-controlled ZnO nanorod array growth. Flexible Kapton polymer substrate is coated in a Au thin film and PMMA resist. (a) Desired density is defined using electron beam lithography, and the Au pattern is subsequently exposed during the developing step. (b) The patterned substrate is immersed in a nutrient solution bath and held at a −500 mV bias relative to the reference electrode. (c) The PMMA resist is removed in the lift-off step. [25]

In this section, the site-selective growth of individual ZnO nanorods in patterned arrays by a wet chemical approach on organic substrates is described. This novel synthesis technique does not require a ZnO thin film or nanoparticle seeds and it can be carried out at low temperatures (<70 ºC) making it an important synthesis technique for flexible electronic applications.

3.3.2 Experimental Procedure

The following process flow employed electron beam lithography to define the nanorod positions and an applied potential across the substrate relative to a second reference electrode to enhance the ZnO nucleation. Figure 3.7 details the process flow. The substrate was a 50 μm thick Kapton polyimide film provided by Du Pont (HN200). A thin layer of Au was thermally evaporated (0.3 Å/s deposition rate, 50 nm) to provide electrical conductivity and uniform nucleation sites on the substrate. The substrate was then spin coated with 2% 495,000 M_w PMMA resist in anisole at 2000 rpm for 45 s resulting in a thickness c.a. 75 nm. Finally, the substrate was baked on a hotplate at 180 °C for 90 s to remove the solvent. Arrays of circular patterns (diameters of 200 nm & 1 – 9 μm) were patterned into the resist using a LEO 1550 field emission scanning electron microscope (FESEM) modified with a J.C. Nabity Nanometer Pattern Generation System (NPGS). The substrates were developed in a 3:1 by volume isopropyl alcohol/methyl isobutyl ketone solution to reveal the patterned features. Electrical contact was made to the substrate by selectively removing a small portion of the PMMA resist using acetone. The patterned substrate was submerged vertically into a nutrient solution parallel to a second Au coated Kapton substrate of equal dimensions referred to as the reference electrode. A -500 mV potential was applied relative the patterned substrate using a Hewlett Packard DC power supply (Model E3620A). The aqueous nutrient solution was composed of 20 mM zinc nitrate hexahydrate and 20 mM hexaminetetramine (HMTA) and maintained at 70 ± 5 °C on a hot plate. All chemicals were reagent grade and purchased from Fluka. The reaction time was varied between 1-5 hrs in order to control the nanorod length.

Once the synthesis was complete, the PMMA resist was removed with acetone, the sample was rinsed with DI water and air dried overnight. The as grown nanorods were characterized by a LEO 1530 FESEM operated at an accelerating voltage of 5 kV. X-ray diffraction data was collected on a PANalytical X-Pert Pro Alpha-1 with Cu Kα radiation.

3.3.3 Experimental Results

The process technique enables position control of ZnO nanorods of micron and submicron sized patterns. Figure 3.8a demonstrates micron scale patterning of 5 x 5 arrays with circular patterns ranging in diameter from 1 to 9 μm in micron step sizes. The largest diameter array of 9 μm is shown in Figure 3.8b. The nanorods range in diameter from 50-150 nm and have a uniform length of 1.4 μm. The nanorods exhibited a high degree of vertical alignment and growth density while fully occupying the patterned regions as can be seen in Figure 3.8c. A small amount of non-vertical growth was observed at the resist mask boundaries.

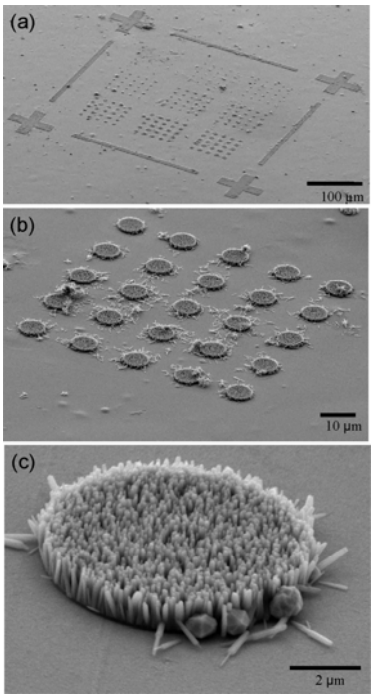

Figure 3.8 SEM images of micron-scale ZnO nanorod patterns of 5 × 5 arrays. (a) Low-magnification tilted SEM image of ZnO nanorod arrays ranging in diameter from 1 to 9 µm. (b) Tilted SEM image of a patterned ZnO nanorod array with a 9 µm circular diameter. (c) High-magnification tilted SEM image of a single patterned ZnO nanorod array with a 9 µm circular diameter. [25]

In addition, submicron-sized patterns were defined for growth of single ZnO nanorod arrays. Figure 3.9a shows a low magnification SEM image of a 25 x 25 array of individual ZnO nanorods separated by 1.25 µm. Circular patterns of 200 nm were defined in the resist in order to nucleate a single ZnO nanorod. ZnO nanorods did not grow on the PMMA resist regions due to a lack of nucleation sites [22]. It was found that 200 nm was the optimum circular diameter in order to nucleate a single nanorod under the given experimental conditions. At 70 °C, the approximate growth rate was 0.7 µm/h. The nanorod length was controlled by the synthesis time. Figure 3.9b shows a high magnification SEM image of the ZnO nanorod array profile. Figure 3.9c shows a top SEM image of the array and demonstrates that the nanorods exhibit a high degree of

vertical alignment. The base diameter was defined by the resist mask. Above the resist, lateral growth occurred along the non-polar $\{2\bar{1}\,\bar{1}\,0\}$ planes resulting in nanorods with a diameter of 200 ± 50 nm.

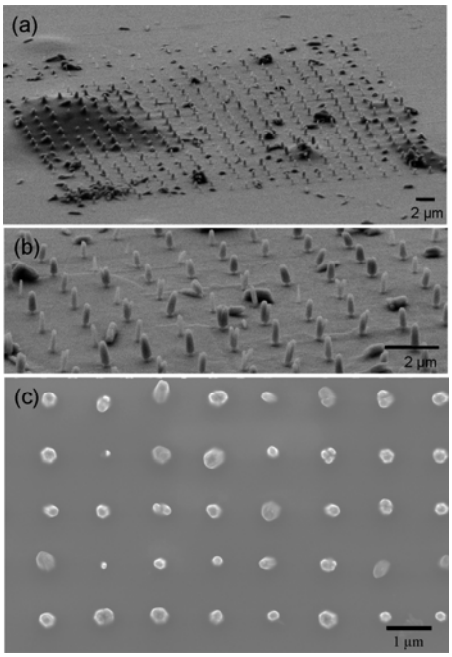

Figure 3.9 SEM image of a 25 × 25 array of patterned single ZnO nanorods with a spacing of 1.25 μm. (a) Low-magnification SEM image at a 70° stage tilt of a ZnO nanorod array. (b) Higher magnification SEM image of the array. (c) Top view SEM image of the array. [25]

The ability to scale up the patterned growth to larger array sizes and densities has also been demonstrated. Figure 3.10a shows a SEM image of a 50 x 50 array of single ZnO nanorods separated by a distance of 0.5 μm. The lengths ranged from 1.8 - 2.0 μm and some lateral growth can be seen in the SEM profile image in Figure 3.10b. The base width was 200 nm as defined by the resist pattern and the upper diameter ranged from 300 - 400 nm. The lateral growth caused some of the nanorods to detach from the substrate.

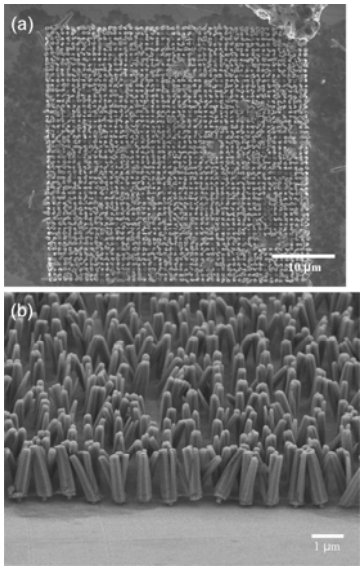

Figure 3.10 SEM image of a 50 × 50 array of patterned single ZnO nanorods with a spacing of 0.5 µm. (a) Top view SEM image of the array. (b) SEM image of the nanorod array at a 60° stage tilt. [25]

After systematically varying the diameter of the patterned circular features, it was found that nucleation could not be achieved within smaller pattern sizes (<1 µm) without an applied potential. The nucleation process was hampered since there were fewer nucleation sites exposed on the Au. It has been found that an applied potential increases the nucleation density of ZnO nanorods by up to 4 orders of magnitude on polished surfaces [26]. The applied potential was essential for achieving high density nucleation within the micron-sized patterns and single nanorod nucleation in the 200 nm diameter patterns.

ZnO nanostructures form by the hydrolysis of zinc nitrate in water in the presence of HMTA. The detailed role of HMTA is still under investigation. HMTA is a nonionic cyclic tertiary amine that can act as a Lewis base with metal ions and a bidentate ligand capable of bridging two zinc(II) ions in solution [27]. HMTA can also hydrolyze to produce formaldehyde and ammonia under the given reaction conditions [4]. It is

thought to gradually decompose and provide a steady supply of ammonia which can form ammonium hydroxide and complex with zinc(II) to form $Zn(NH_3)_4^{2+}$ [28, 29]. Zinc(II) is known to coordinate in tetrahedral complexes. Under the given pH and temperature, zinc(II) is thought to exist primarily as $Zn(OH)_4^{2-}$ and $Zn(NH_3)_4^{2+}$. The ZnO is formed by the dehydration of these intermediates. Although the system is quite complex, we represent the dominant chemical reactions on the basis of our analysis and others [29-33] by the following formulae:

$$C_6H_{12}N_4 + 6\ H_2O \leftrightarrow 6CH_2O + 4NH_3 \quad (7)$$

$$C_6H_{12}N_4 + Zn^{2+} \rightarrow [Zn(C_6H_{12}N_4)]^{2+} \quad (8)$$

$$NH_3 + H_2O \leftrightarrow NH_4^+ + OH^- \quad (9)$$

$$Zn^{2+} + 4NH_3 \rightarrow Zn(NH_3)_4^{2+} \quad (10)$$

$$Zn^{2+} + 4OH^- \rightarrow Zn(OH)_4^{2-} \quad (11)$$

$$Zn(NH_3)_4^{2+} + 2OH^- \rightarrow ZnO + 4NH_3 + H_2O \quad (12)$$

$$Zn(OH)_4^{2-} \rightarrow ZnO + H_2O + 2OH^- \quad (13)$$

$$[Zn(C_6H_{12}N_4)]^{2+} + 2OH^- \rightarrow ZnO + H_2O + C_6H_{12}N_4 \quad (14)$$

After analysis of the dominant chemical reactions in the system, the role of the applied potential is more apparent. Positively-charged intermediates are formed in reactions (8) and (10). The electric field established between the patterned substrate and the reference electrode caused the $Zn(NH_3)_4^{2+}$ and $[Zn(C_6H_{12}N_4)]^{2+}$ intermediates to migrate towards the negatively biased patterned substrate. This caused a high concentration of the ZnO precursors to become localized at the patterned substrate

region. Thus, enhanced nucleation could be achieved in the submicron space confined regions. Others [26, 34-37] have proposed that the applied potential causes an increased OH^- concentration by the reduction of NO_3^- in an electrochemical reaction at the negative electrode (for reaction (15), E°_{red}=0.93 V). As such the reaction would proceed as follows:

$$NO_3^- + H_2O + 2e^- \rightarrow NO_2^- + 2OH^- \quad (15)$$

$$Zn^{2+} + 2OH^- \rightarrow ZnO + H_2O \quad (16)$$

Both mechanisms involve an increased precursor concentration at the patterned substrate and further investigation is required to determine which is more dominant. X-ray diffraction data shown in Figure 3.11 shows the data for the patterned substrate. The appearance of the (0002) peak at 34.6º confirms the [0001] as the fast growth direction and the high degree of vertical alignment. It also confirms the crystallinity of the nanorods. The strong intensity of the Au peaks diminishes the intensity of the (0004) peak at 72.5º.

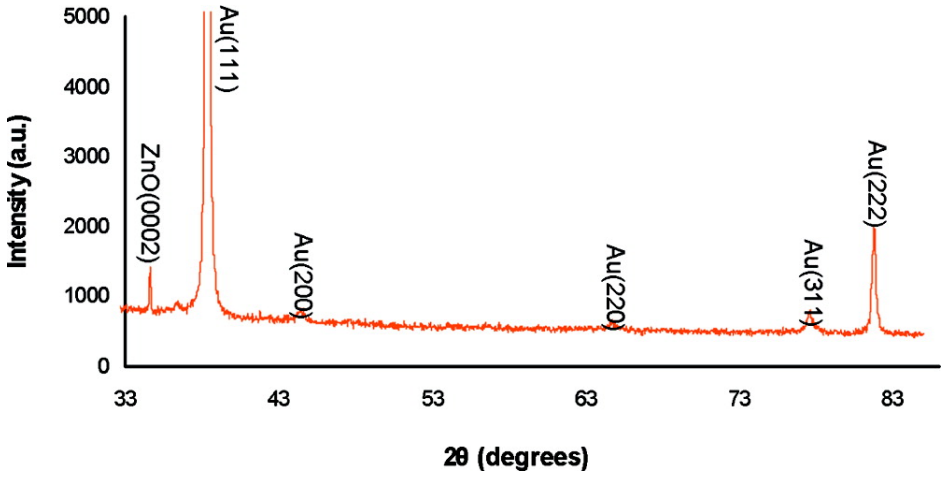

Figure 3.11 X-ray diffraction data for the patterned ZnO nanorod array. [25]

The optical properties of the ZnO nanorods grown on patterned and unpatterned substrates were investigated. Figure 3.12a shows the room temperature photoluminescence (PL) spectrum. In general, ZnO exhibits three PL bands in the UV, green, and yellow regions [38]. Yellow emission at 578 nm for the unpatterned substrate and green emission at 534 nm for the patterned substrate were observed. The yellow and green emissions are attributed to the radiative recombination of the electrons from shallow donors with the trapped holes from singly ionized oxygen vacancies and interstitial oxygen defects [39]. The unpatterned sample can be seen in Figure 3.12b.

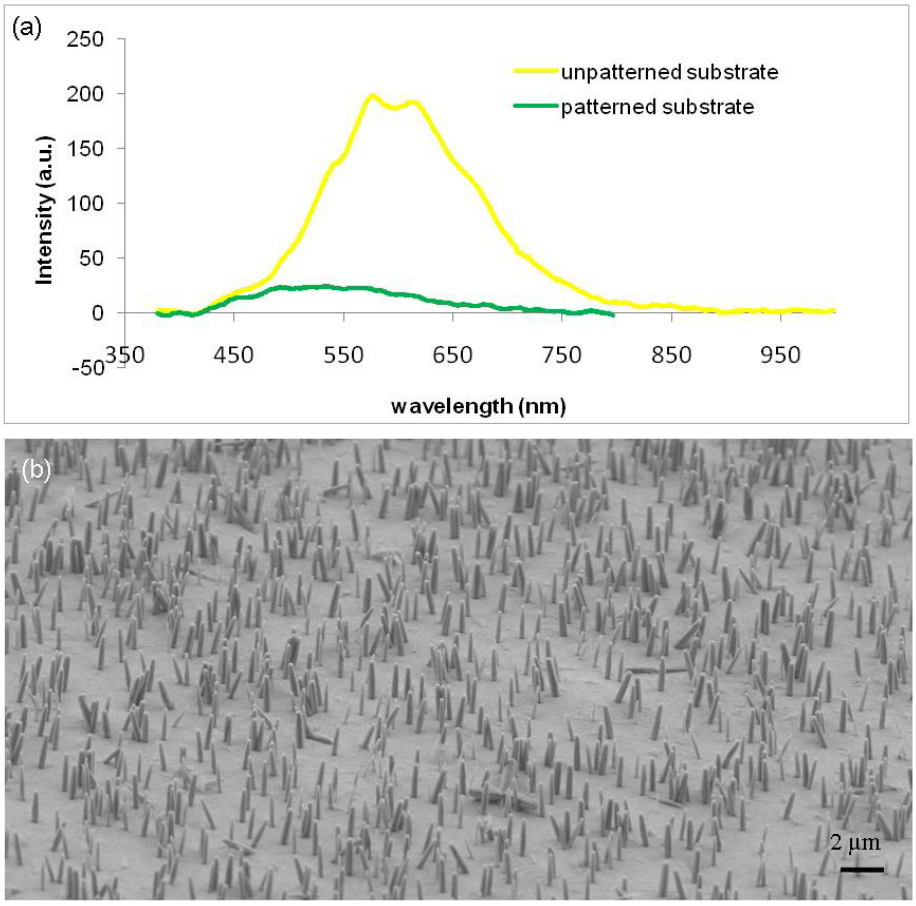

Figure 3.12 (a) Photoluminescence spectrum of patterned and unpatterned ZnO nanorod array. (b) Tilted SEM image of unpatterned ZnO nanorods using an applied potential.

Figure 3.13a shows a low magnification SEM image of a large scale patterned array of individual ZnO nanorods separated by 535 nm. Circular patterns of 200 nm were defined in the resist in order to nucleate a single ZnO NR. Fig. 3.13b shows a high magnification top SEM image of the ZnO NR array showing the hexagonal cross section and well-defined facets and demonstrates that the NRs exhibit a high degree of vertical alignment. Fig. 3.13b inset shows an optical micrograph of the patterned ZnO NR array appearing green due to periodic spacing of 535 nm.

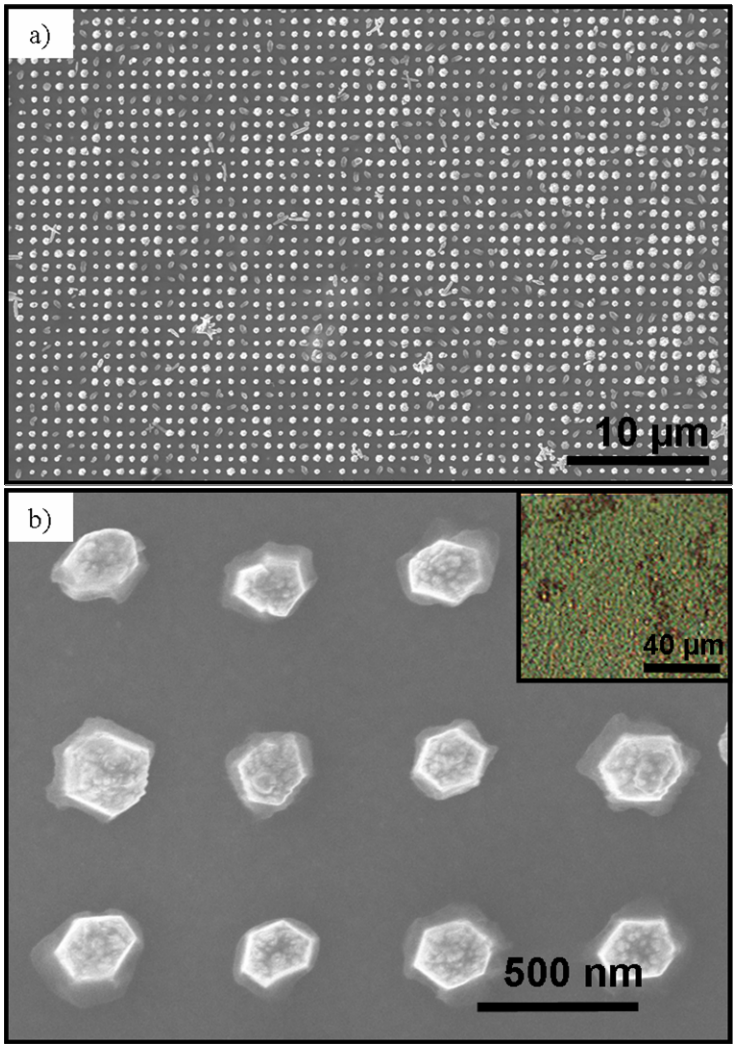

Figure 3.13 SEM images of large-scale ZnO nanorod array (a) low magnification and (b) high magnification. Inset is the optical micrograph of large-scale patterned ZnO nanorod array appearing green due to periodic spacing of 535 nm. [40]

3.3.4 Brief Summary

In summary, a new synthesis technique has been demonstrated in this section for growing ZnO nanorods site-selectively on a polymer substrate. The synthesis does not require the use of ZnO seeds and has been demonstrated at temperatures as low as 70 ºC. The technique utilizes electron beam lithography to define the specific nanorod positions and an applied potential to enhance the nucleation process. In terms of electronic device integration, the nanorods are already in electrical contact with the Au thin film and if left remaining the PMMA resist can serve as an insulating layer. This technique represents a novel and low cost way for integrating ZnO nanorods into flexible electronic and piezoelectronic [41] devices.

3.4 Density Control

In this section, density-controlled, solution grown ZnO nanorod arrays by a layer-by-layer polymer approach is discussed. Subsequently, data from field emission studies are presented.

3.4.1 Introduction

Important for flat-panel display technology, one-dimensional (1-D) nanomaterials such as nanotubes and nanowires are considered promising candidates for achieving high field-emission currents at low electric fields due to their high aspect ratios. In the last decade, field-emission (FE) research efforts have mostly focused on carbon nanotubes (CNTs) due to their high electrical conductivity, aspect ratio, thermal stability as well as low fabrication cost [42-44]. However, metal oxide nanomaterials such as ZnO are gaining increasing interest due to their high chemical and thermal stability and tunable electronic properties. ZnO, a wide band-gap semiconductor (E_g = 3.37 eV) and

piezoelectric material, is an important functional material utilized in photovoltaics, lasers, energy harvesting nanogenerators, and sensors [6, 9, 45-47].

For a given material, it has been shown that the FE efficiency can be improved by controlling the emitter density and aspect ratio [48-52]. Emitters too closely packed suffer from a screening effect whereas emitters spaced too far apart approach the behavior of a thin film [50, 53]. Within the emitter density spectrum, there is an optimal density to achieve the best FE performance. In addition to optimizing emitter density, it has been shown that a sharp, elongated morphology such as a nano-needle or -pencil can improve FE performance [54, 55]. Because the field enhancement factor β varies inversely with emitter tip radius, a high local electric field can be generated at a sharp emitter tip to effectively lower the required FE potential barrier (β =emitter height/emitter tip radius).

Recently, Wang et al. have developed a synthesis technique for controlling ZnO nanorod (NR) growth density and showed a correlation with field emission (FE) performance [53, 56]. However, this vapor-liquid-solid technique based on varying the thickness of a Au catalyst thin film requires a high temperature (T=950 °C) to melt the Au catalyst rendering it costly and incompatible with organic materials valued in the flexible display industry. There has been little research into optimizing FE performance by controlling ZnO NR density using low temperature methods. Heralded for its low temperature compatibility with many organic materials, wet chemical ZnO NW synthesis based on the zinc nitrate/hexamethylenetetramine system is becoming quite popular due to its scalability and low cost making it attractive for nano-manufacturing prospects [15].

Therefore, finding a technique for controlling NR growth density compatible with this technique is of great scientific and commercial interest.

With these considerations in mind, a novel low temperature synthesis technique to control ZnO NR array density and morphology to optimize FE performance was developed. The approach was based on a low temperature, wet chemical ZnO NR synthesis technique using a ZnO thin film-deposited Si substrate. In general, ZnO NR array density is typically quite high when synthesized on a polycrystalline ZnO thin film since each crystallite exposed to the nutrient solution can act as a growth site. The idea was to establish a thin polymer film above the ZnO seed layer to inhibit the precursor ion transport. In this way, the rate of reactant ions traveling from solution to the seed layer could be limited, thereby reducing the probability of eventual NR growth. Polyelectrolyte layer-by-layer (LBL) polymer thin films were chosen for this purpose because of their excellent thickness control ability and hydrophilic nature [57-59].

3.4.2 Experimental Procedure

Si substrates with dimensions of 1 cm x 1 cm were deposited with a 100 nm ZnO seed film by RF magnetron sputtering. To establish the ion transport barrier, the ZnO seed-coated samples were spin-coated with alternating layers of poly(allylamine hydrochloride) (PAH) and poly(sodium 4-styrenesulfonate) (PSS) polymers. Samples of 0, 1, 2, 3, 4, and 5 bilayers were prepared. AFM analysis verified the film thicknesses and showed in general that each polymer bilayer measured 2.5 nm (see Figure 3.14). For solution-based NR array synthesis, the substrates were floated face-down in a 50 ml Pyrex glass bottle containing a 20 mM solution of zinc nitrate hexahydrate and hexamethylenetetramine (HMTA) and aged for 1.5 hrs at 90 °C in a laboratory grade box

oven. Substrates were subsequently rinsed with water and ethanol and oven dried at 60 °C for 30 mins in air.

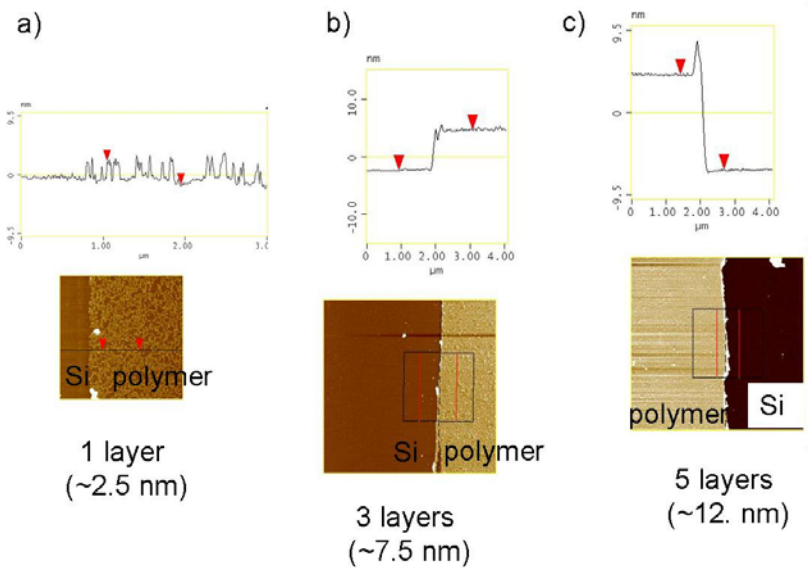

Figure 3.14 AFM line scan and phase image analysis of LBL polymer layers coated on bare Si substrate (a) 1 bilayer sample showing penetrating pores (b) 3 bilayer sample showing a fully coated polymer substrate (c) 5 bilayer sample showing a fully coated polymer substrate. [60]

All chemicals used were reagent grade. Zinc nitrate and hexamethylenetetramine were purchased from Fluka. PAH and PSS purchased from Sigma-Aldrich had a M_w of 70,000 and concentration of 0.2 % (w/w). Details of the LBL deposition process can be found elsewhere [61, 62]. Substrates of (100) oriented Si were sputtered at room temperature and then annealed at 350 °C for 20 mins to improve grain alignment and crystallinity. NR characterization was carried out on a LEO 1530 FE scanning electron microscope operated at 5 kV. X-ray diffraction data were collected on a Panalytical X'Pert Pro diffractometer with Cu Kα radiation, a Göbel mirror, 0.09˚ parallel plate collimator and 0.04 radian Soller slits. AFM topographical and phase images (Figure 3.14) were collected on a Digital Instruments Dimension 3000 in tapping mode under

ambient conditions. For these measurements, LBL polymers were spin-coated onto bare Si substrates to minimize surface roughness effects. The thickness of the polymer layers with different number of bilayers was measured using AFM by scanning along the edge of the film. For FE measurements, a Keithley 6517A electrometer was used to both apply the voltage and measure the current. Fluorescence images were taken on a Canon 400D camera outfitted with a EF50mm f/2.5 compact macro lens.

3.4.3 Experimental Results

3.4.3.1 Structural analysis

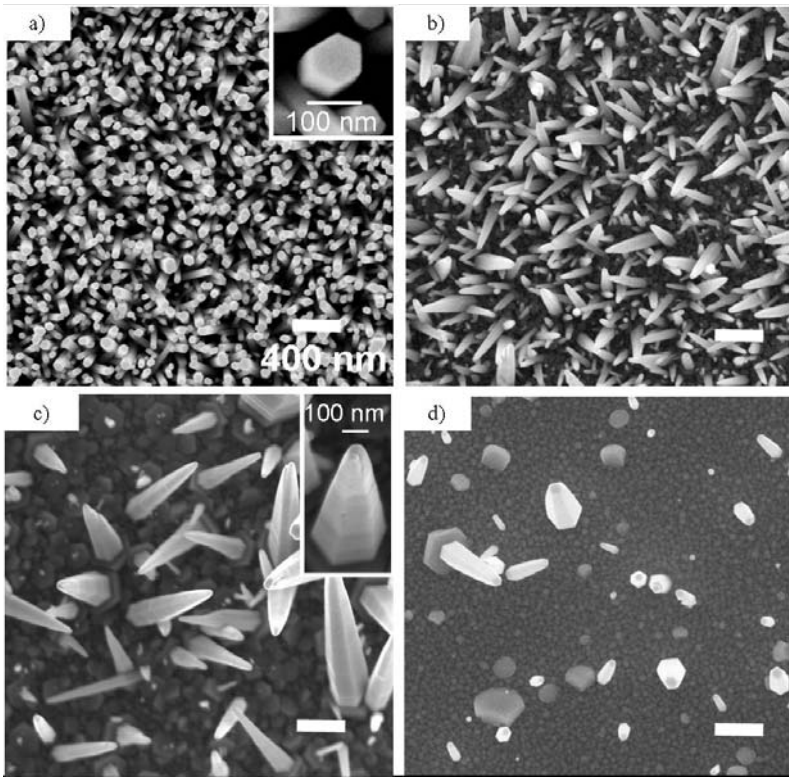

Figure 3.15 Top view SEM micrographs at same magnification of ZnO nanorod arrays with substrates of varying number of PSS/PAS bilayers. (a) 0 bilayers. Inset shows nanorod morphology. (b) 1 bilayer (c) 3 bilayers. Inset shows nanorod morphology. (d) 5 bilayers [60]

Figure 3.15 displays the representative SEM images of the density-controlled ZnO NR arrays for the 0, 1, 3, and 5 bilayer samples showing the general trend of decreasing density. As expected in fig. 1a, the sample without a polymer barrier exhibits the highest density. Likewise, the density decreases as the number of polymer bilayers increases, as shown in Figures 3.15b – 1d corresponding to 1, 3, and 5 bilayer samples, respectively. The Figure 3.15 insets show high magnification SEM images of the morphology. It can be seen that the NRs become tapered for the polymer-coated samples. We believe that the polymer layer effectively slowed the initial NR growth kinetics. As the polymer layer increased to 5 layers (Figure 3.15d), instead of NR growth, some ZnO particles precipitated out on the substrate and in the solution due to the migration of some ZnO precursor ions through the barrier polymer film. As the reaction sequence proceeds, the available ZnO precursor ions begin to decrease and the net effect is a morphological NR tapering. It was also observed that the NR shape changed from regular rod with a flat top to a sharp pencil shape. The rod size and length distributions were also increased when the number of the polymer thin layer was increased.

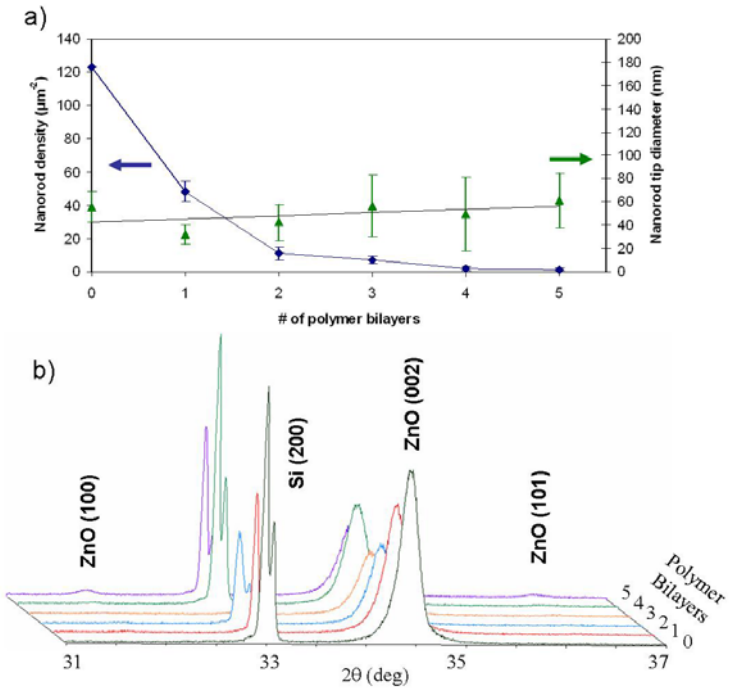

Figure 3.16 (a) Plot of nanorod density and nanorod tip diameter as a function of the number of LBL polymer bilayers. (b) X-ray diffraction spectra for the samples with differing number of polymer bilayers. [60]

Quantitative analysis was carried out to determine the relationship between both the NR density and tip diameter and the number of polymer bilayers as shown in Figure 3.16a. The density was uniform throughout the 1 cm x 1 cm substrate. NR average density was calculated by counting the number of NRs shown in SEM images of the same magnification at three different substrate locations chosen at random. As shown in Figure 3.16a, the average NR density decreases exponentially with values of 123, 48, 11, 7, 2, and 1 NR/μm^2 corresponding to 0, 1, 2, 3, 4, and 5 polymer bilayers. It should be noted that the FE performance strongly depends on the tip diameter. The average NR tip diameter, estimated by measuring the tip diameter of 20 NRs chosen at random imaged using high magnification SEM, indicates that although the base diameter increased, the

tip diameter change is not significant, as shown in fig. 3.16a. NRs in the various samples ranged in length from ca. 0.2 – 2 μm.

X-ray diffraction data shown in fig. 3.16b confirm the epitaxial nature of the aligned NRs with the seeds as well the <001> fast growth direction. The two strong peaks seen at 33.0˚ and 34.4˚ correspond to the substrate Si (200) and ZnO (002) planes. The presence of only a single ZnO (002) peak indicates a high degree of vertical alignment. Weak peaks at 31.8˚ and 36.3˚, present only in the case of the 5 bilayer sample, correspond to ZnO (100) and ZnO (101) reflections and indicate that this sample had poor vertical alignment.

AFM analysis (see Figure 3.14) revealed that the 1 and 2 polymer bilayer samples with thickness of 2.5 and 5.0 nm, respectively, contained small penetrating pores which directly exposed the ZnO seed layer to the nutrient solution. Thus, the density of the pores most likely controlled the ion transport to the seed layer. In the 3, 4, and 5 bilayer samples corresponding to thicknesses of 7.5, 10, and 12.5 nm, respectively, the AFM results show that the polymer film did not contain any penetrating pores and fully covered the seed layer. It is believed that the hydrophilic PAH/PSS LBL polymer swelled in the aqueous solution allowing for the passage of ZnO intermediate precursor ions such as $Zn(OH)_4^{2-}$ and $Zn(NH_3)_4^{2+}$ [28]. In this case, the thickness of the polymer primarily controlled the ion transport to the seed layer surface and the probability of eventual NR growth.

3.4.3.2 Patterned growth

To reliably incorporate ZnO NR arrays into electronic device applications it is important to achieve scalability and process control. To demonstrate the precise level of

density control possible using this technique, patterned substrates of varying density were prepared using soft lithography methods over a 1 mm x 1 mm area. The SEM images can be seen in Figure 3.17. Regions of varying polymer thickness were patterned corresponding to 3 and 13 bilayer stripes on a ZnO thin film-deposited Si substrate. A simple process flow was employed and shown in Figure 3.17a based on capillary transfer lithography. First, the ZnO thin film was coated with 3 bilayers of PAH/PSS. Second, a 400 nm thick polystyrene (PS) pattern with a periodicity of 10 μm defined by a polydimethylsiloxane (PDMS) stamp was deposited onto the initial 3 bilayers. Next, an additional 10 PAH/PSS bilayers were spin-coated on top of the PS patterned substrate to provide a thickness differential. Finally, the PS pattern was lifted off in toluene leaving patterned stripe features with 3 (future high density growth region) and 13 bilayers (future low density growth strip) on the ZnO seed layer. After patterning, the substrates were subjected to the same solution-based synthesis conditions as described above. The stripes can be seen in the low magnification top view SEM image in Figure 3.17b. Figure 3.17c shows the thinner 3 bilayer 7 μm wide stripe regions exhibiting a higher NR density than the thicker 13 bilayer 3 μm wide stripe regions. The 60° tilted SEM image in Figure 3.17d further reveals the disparity in growth density. This evidence further supports that the polymer thickness controls the NR growth density.

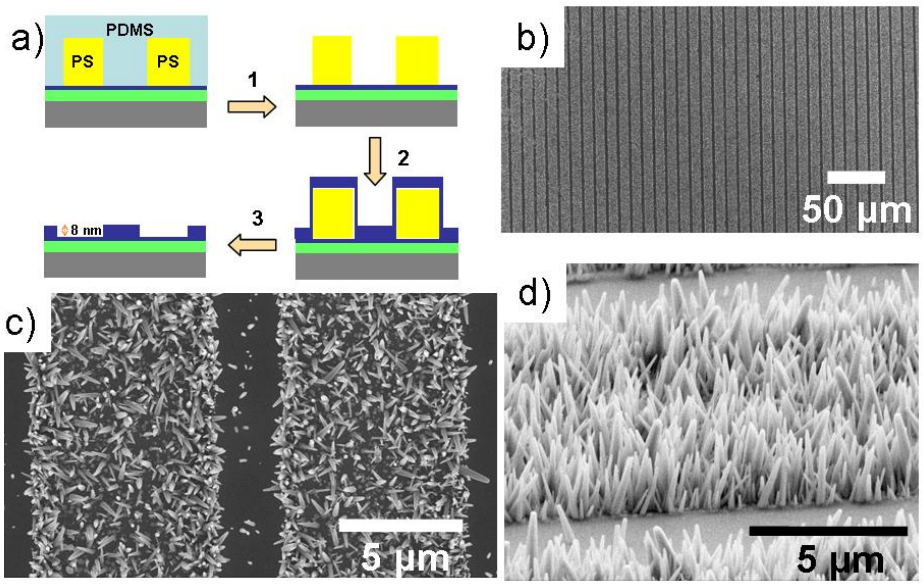

Figure 3.17 Patterned growth via microcontact printing. a) Process flow for soft lithography (not to scale). A ZnO-coated Si substrate contains an initial 3 PSS/PAH bilayers. In step 1, a polystyrene (PS) stripe pattern is transferred to the substrate. In step 2, an additional 10 bilayers are spin coated. In step 3, the PS is dissolved leaving a 8 nm differential thickness b) Low magnification SEM image of striped pattern of bilayers with a 10 µm periodicity (c) High magnification SEM image of stripe pattern (d) 60° tilted SEM image of patterned sample. [60]

A differential thickness of ca. 8 nm verified by AFM was significantly smaller than that expected for 10 bilayers (ca. 23 nm). This can be explained by the presence of hydrophobic PS stripes on the initial 3 bilayers causing the surface to poorly wet with the subsequent hydrophilic polymer solution. Furthermore, the force exerted during the PDMS stamping process caused compression of the initial 3 bilayers, verified by AFM. While it seems unlikely that the elastomeric PDMS stamp could cause significant stress to deform a glassy LBL polymer as a significant depression in T_g for ultrathin polymer film may occur [63, 64]. Due to the ultra-thin film nature, the initial 3 bilayers (ca. 7.5 nm) exhibited a relatively low stiffness resulting in compression during the stamping process. All these factors likely contributed to the lower than expected polymer thickness differential.

3.4.3.3 Field emission properties

To investigate the influence of NR array density on FE properties, representative samples of 0, 1, 3, and 5 bilayers were tested using a simple diode configuration. A gap distance of ca. 80 μm was fixed between an ITO glass anode and the NR array cathode by Kapton and Si spacers. The vacuum level of the measurement chamber was maintained at $1x10^{-6}$ torr. Figure 3.18a shows current density versus applied electric field measurement results for the series of samples. Similar to CNTs, the highest density 0 bilayer sample performed poorly as a field emitter which was generally attributed to a screening effect [50]. The turn-on field was 14.1 V μm^{-1} at a current density of 10 μA cm^{-2}. The FE data reveal that the medium density 1 and 3 bilayer samples showed the best FE performance. They turned on at electric fields of 9.8 and 5.1 V μm^{-1}, respectively. The 3 bilayer sample jumped to a high current density of 50 μA cm^{-2} at an electric field of ca. 7 V μm^{-1}. The lowest density sample of 5 bilayers showed poor FE efficiency as it did not draw a current density above 10 μA cm^{-2}. This density versus FE performance trend is consistent with others [53]. The turn-on field values are summarized in Table 3.1. The Figure 3.18a inset shows a representative fluorescence image for the medium density samples. This fluorescence image of the 1 bilayer sample at a 62.5 V μm^{-1} electric field demonstrates a relatively uniform emission over a large sample surface area.

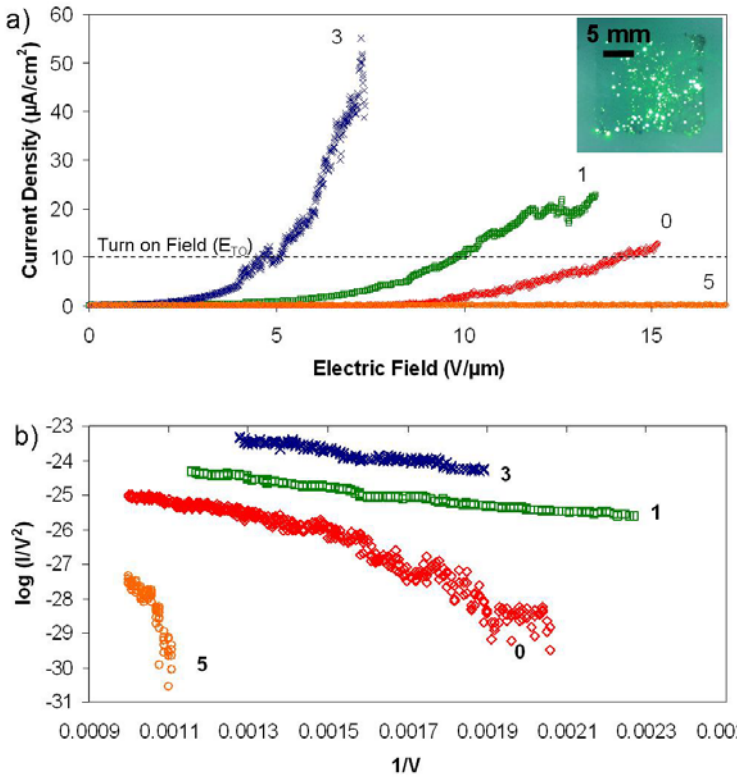

Figure 3.18 Field Emission Data (a) Field-emission I-V data for samples of 0,1,3, and 5 bilayers. Inset shows fluorescence image of the 1 bilayer sample. (b) Fowler-Nordheim plots [60]

The current-voltage (I-V) plots were converted to Fowler-Nordheim (F-N) plots by expressing ln (I/V^2) versus 1/V and are shown in Figure 3.18b. The 4 F-N curves show a linear behavior and negative slope indicating that the FE current originates from barrier tunneling from the cathode due to an electric field. The field enhancement factor β, describing the ratio of the local electric field at the emitter tip versus the macroscopic electric field, can be calculated from the F-N curve slope according to

$$\beta = 6.83X10^{9}\frac{d\phi^{3/2}}{k} \tag{17}$$

where d is the gap distance, φ is the work function of ZnO (5.2 eV) and *k* is the slope of the F-N curve. Following a trend similar to the turn-on field, NR samples with bilayers

of 1 and 3 show the highest field enhancement factors of 4910 and 5884, respectively. Table 3.1 summarizes the field enhancement factors. In general, a wide range of β values have been reported in the literature for ZnO nanostructures ranging from ca. 300 to 41,000 [65]. The highest values have been achieved using high temperature synthesis techniques such as carbonthermal vapor transport, molten-salt-assisted thermal evaporation, and metal organic chemical vapor deposition [49, 54, 66]. In terms of low temperature, solution-based FE studies, Liu et al. and Ahsanulhaq et al. have recently reported beta values of 2350 and 1680, respectively [55, 67]. The high reported value of 5884 reported in this chapter is generally attributed to the optimized density and tapered morphology giving rise to a sharp emitter tip with a large localized electric field. Thus, this reasonably large β value of 5,884 along with the low turn-on field of 5.1 V μm^{-1} achieved in the 3 bilayer sample suggest that the decreased NR density and tapered morphology could be useful to fabricate optimized ZnO field emitters.

Table 3.1 Summary of field-enhancement factors and turn-on fields for ZnO NR arrays with different densities [60]

Number of LBL Polymer Bilayers	NR Density [μm^{-2}]	β	E_{TO} [V/μm]
0	123	1538	14.1
1	48	4910	9.8
3	7	5884	5.1
5	1	173	N/A

3.4.4 Physical Model of Growth Mechanism

AFM analysis revealed that from three polymer bilayers and above ($x \geq 7.5$), the polymer film hardly contained any pores and almost fully covers the seed layer. On the

other hand, thinner films of one bilayer $(x = 2.5)$ contained small penetrating pores that directly expose the ZnO seed layer to the nutrient solution. AFM analysis was not done for films with two bilayers $(x = 5)$. By looking at the AFM line scan profile and taking the ratio of the length of the lines at the baseline versus the total line length, the percentage surface area exposed for $x = 2.5$ was computed as 64.5%.

Based on the above finding, two growth mechanisms were proposed – *pore-dominated* and *diffusion-dominated* – to explain the influence of layer-by-layer polymer thickness on nanowire growth. When there is no polymer layer on the substrate, growth is 100% pore-dominated (direct-contact). When the substrate is covered by one or two layers of polymer $(x = 2.5, 5.0)$, the density of the pores in the polymer control the ion transport to the seed layer. Some precursor ions are also expected to diffuse through the polymer layer. Thus, at this stage, the growth is essentially assumed to be a result of two processes – direct contact and diffusion. As the number of layers increases beyond two, growth is essentially due to diffusion, where the ions must penetrate through the polymer film.

A physical model is proposed based on the diffusion-dominated growth. The diffusion process is expected to be governed by Fick's second law of diffusion, which is as follows. Let $C(x,t)$ denote the concentration of precursor ions (in units of number of atoms per unit volume) after time *t* at a distance *x* from its surface. Then, the diffusion process is explained by:

$$\frac{\partial C}{\partial t} = D\frac{\partial^2 C}{\partial x^2}, \tag{18}$$

where D is the diffusion coefficient. Now, $C_0(x) = C(x,0)$ denotes the concentration of precursor ions at a distance x from the surface of the precursor solution at the instant the experiment begins. It is therefore reasonable to assume that $C_0(x) = 0$ for all $x > 0$, since at time $t = 0$, diffusion would not have started. We also assume that $C_s(t) = C(0,t)$ remains more or less unchanged throughout the time the diffusion takes place. A particular solution of the above differential equation under the boundary conditions $C(x,0) = 0$ and $C(0,t) = C_s$ is given by:

$$C(x,t) = C_s - C_s erf(\frac{x}{2\sqrt{Dt}}), \tag{19}$$

where *erf* is the error function given by

$$erf(z) = \frac{2}{\sqrt{\pi}} \int_0^z e^{-u^2} du = 2\{\Phi(z\sqrt{2}) - \frac{1}{2}\},$$

and Φ denotes the cumulative density function of the standard normal variable. Consequently, (3) can be re-written as

$$C(x,t) = 2C_s \Phi(-\frac{x}{\sqrt{2Dt}}). \tag{20}$$

Let t^* denote the total experimental time. The diffusion coefficient D is unknown and approximations are made.

Using a physical-statistical model, the data was fit to determine values of D [68]. The lower and upper bounds of D are thus obtained as 4×10^{-3} and 17.8×10^{-3} atoms per nm^2 per sec. The computation is based on the total experiment time, t^*; however, the actual diffusion time which is less than t^* is unknown. From a physical standpoint, the

majority of the mass transport is expected through the polymer barrier occurs during the initial 30 minutes of the experimental time. In this case, the lower and upper bounds of *D* are obtained as 12.8×10^{-3} and 53.3×10^{-3} atoms per nm^2 per sec.

The diffusion coefficient, *D* is proportional to the velocity of the ZnO precursor ion species diffusing down the concentration gradient from a region of high concentration to low concentration. Thus, it provides important insight into the transport physics of the diffusing species through the polymer barrier. The diffusion coefficient is a temperature dependent quantity that can be expressed as $D = D_0 \exp(-E_a/RT)$, where D_0 is the maximum diffusion coefficient at infinite temperature, E_a is the activation energy, *R* is the gas constant, and *T* is the temperature. The baseline approximation of *D* at the specified temperature can be used to solve for other values of *D* at other experimental temperatures in order to further optimize the ZnO precursor species mass transport properties. In this way, future experiments can be guided by this model to achieve greater levels of growth control for ZnO nanowire arrays.

3.4.5 Brief Summary

In summary, a simple, scalable, and cost-effective technique for controlling ZnO NR array growth density by varying polymer film thickness was discussed in this section. The FE results revealed that an emitter density of 7 μm^{-2} and a tapered NR morphology resulted in a high field enhancement factor of 5,884 making this an important technique for flat panel display technology. Lastly, this low temperature technique can easily be extended to organic substrates for flexible electronic NR array-based FE devices such as electronic paper.

3.5 Orientation Control

In the previous section, all nanowire synthesis experiments focus on vertically-aligned nanowire growth. In the following section, efforts focus on horizontally-aligned nanowire growth. Orientation is especially important in order to bridge ZnO nanowires across trenched electrodes for nanoelectronic devices.

3.5.1 Introduction

Integration of individual nanowire (NW) or nanotube devices into large-scale nanosystems in a precise and efficient manner is an attractive research area. However, it remains a challenge despite fast development of nanofabrication and manipulation techniques [69, 70]. Using as-grown NWs as building blocks, previous work has been done in cross-bar arrays of GaP, InP, and Si NWs fabricated using flow field and electrical field induced self-assembly [46, 71, 72]. The challenge for this type of assembly is scale up and precise control over the self-assembly.

Seeking an alternate strategy that can directly grow NWs onto prefabricated nanodevice structures is of great interest and there have been some recent successes. For example, using metal-organic chemical vapor deposition, an individual Si NW has been grown as a bridge across a microscale trench on a Si or silicon on insulator substrate [73, 74]. Using a layer with ZnO seeds, lateral growth of ZnO NWs across a Si trench via a vapor-solid method was also realized [75, 76]. However, the high temperature vapor-phase approach limits their applicability to temperature sensitive substrates such as plastic and annealing-sensitive platforms. To solve this problem, a hydrothermal synthesis method [15, 20, 77] is described in this section to synthesize similar structures but at a much lower temperature (80 °C). Large-scale and laterally bridged ZnO NWs

have been grown across Au electrode arrays with separations of 500 nm and 10 μm. The as-bridged NW diameters range from 50 to 1000 nm depending on the growth conditions. Using a four-terminal approach, current-voltage characteristics of the grown structures have been characterized at both room temperature (295 K) and low temperature (77 K).

3.5.2 Experimental Procedure

The growth of ZnO NWs was conducted by suspending substrates that had been modified with Au or ZnO seeds in a Pyrex glass bottle filled with an equal molar aqueous solution of zinc nitrate hydrate [$Zn(NO_3)_26H_2O$, Fluka, ≥ 99.0% (KT), 0.01 *M*] and hexamethylenetetramine ($C_6H_{12}N_4$, Fluka, 0.01 *M*) at 80 °C. The reaction time was 1–4 h for both substrates coated with Au or ZnO seeds. After the reaction, the substrates were removed from the solution, rinsed with de-ionized water, and then dried in air at 65 °C overnight.

Figure 3.19 shows a schematic diagram of the synthesis strategy. To define Au side wall electrodes across trenches with 10 μm separation, typical photolithography, dry etching, and Bosch processes were employed. The process started with depositing 100 nm of SiO_2 on a 4 in. silicon wafer (*p* type, <100>, 0.01 Ω cm), as shown in Figure 3.19a using uniaxis plasma enhanced physical vapor deposition. A typical lithography process was then applied to the wafer with AZ5214 image reversal photoresist. The pattern was subsequently transferred to the SiO_2 via dry etching using a Plasma-Therm inductive coupled plasma (ICP) etcher. A Bosch process was utilized to form the deep (etched-through) trenches using ICP with the SiO_2 acting as the hard mask. After that, a 100 nm thick Au coating was deposited on the entire wafer, including the side walls and bottoms of the trenches, using a CVC dc sputterer. Finally, the SiO_2 layer and the Au coating on

top of it were lifted off in HF. After this process, the Au/Si side wall electrodes were formed across the 10 μm trench (Figure 3.19b). The ZnO nanowire synthesis is carried out in Figure 3.19c.

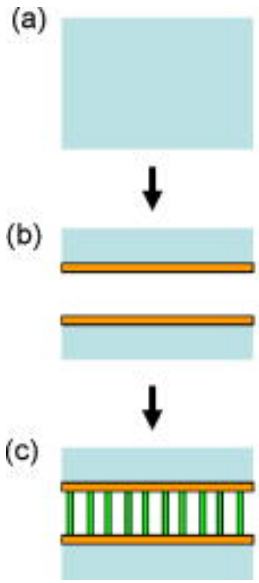

Figure 3.19 Fabrication and growth processes for growing bridged nanowires across trenched electrodes [78]

For electrical characterization, a Keithley 6221 AC/DC current source and 2182A nano-voltmeter combination was used for four-terminal current-voltage measurements. For both room and low temperature characterization, a VPF-700 LN2 optical cryostage was used as a vacuum chamber to hold the NW devices. Au wire bonding and focused ion beam (FIB) nanolithography were used for ensuring good contact and interconnects between the nanowire device and the test platform.

3.5.3 Experimental Results

Figure 3.20 shows SEM images of the as-grown NW devices on the Si substrate. The left region of Figure 3.20a shows the NWs selectively grown from both Au sidewalls separated by 10 μm, but not touching the opposite side. As growth time increased,

nanowires continued to grow longer and eventually made contact to the opposite sidewall (right region of Figure 3.20b). The wire diameter is around 2 μm with a defined length of 10 μm. From the high magnification SEM image in Figure 3.20b, it is evident that the wire grew from right-hand side wall to the left-hand side wall, as shown by the rooted region indicated by the red dotted circle on the right-hand side. An inset energy dispersive spectroscopy spectrum from the side wall revealed the composition of the Au layer on Si sidewall.

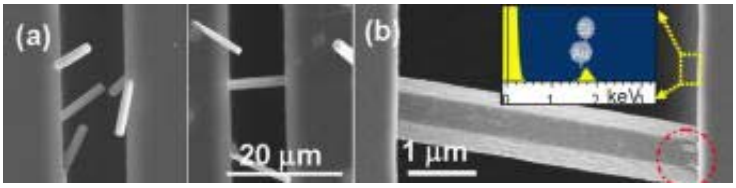

Figure 3.20 (a) low magnification and (b) high magnification SEM images show the as-grown nanowire arrays bridging across Au/Si electrodes [78]

Figure 3.21a is a schematic circuit with a SiO_2 insulation layer on the Si substrate. A real device structure is shown next to the schematic diagram with an array of bridged NWs. The two vertical lines at the top left-hand side and bottom right-hand side are 200 nm Pt interconnects deposited using focused ion beam microscopy.

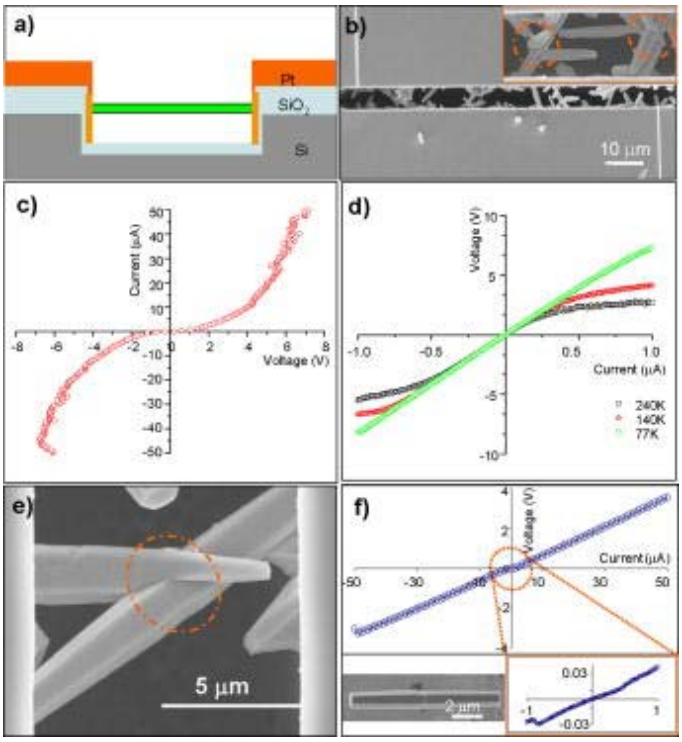

Figure 3.21 (a) Schematic for the transport measurement. (b) SEM image of the bridged nanowire array. (c) and (d) are, respectively, the room temperature and low temperature *I-V* curves for the nanowire arrays across Au/SiO_2/Si electrodes. (e) and (f) are, respectively, a typical multi-nanowire bridge grown with interfacial grain boundaries and the corresponding nonlinear *I-V* characteristics of a freestanding twin-type nanowire with one grain boundary [78].

Figure 3.21b is an *I-V* curve measured at room temperature and is observed to be rather symmetric. At a low current range of ±1 μA, the resistance is ~ 8 MΩ, which suggests a low current leakage due to the existence of an intermediate SiO_2 insulation layer between Au/Pt interconnects and the Si substrate. When the current was increased to ±10 μA, the resistance at higher bias was close to 400 kΩ. The degree of nonlinearity is about 20. Figure 3.21c shows low temperature electrical characteristics at a low bias range of ±1 μA. When the temperature decreased from 240 to 77 K, it was evident that the degree of nonlinearity decreased as well. At 77 K, the *I-V* behavior was linear. This

result suggests that the nonlinear electrical behavior of ZnO nanowires at room temperature is likely due to domination by phonon scattering. Another six bridged NW devices across Au/SiO_2/Si electrodes were also tested, yielding similar *I-V* characteristics as the one described above, suggesting good reproducibility of the as-grown NW devices. It is worth noting, in addition to the temperature effect, that the possible microscopic factor leading to the *varistor-like* nonlinear *I-V* behavior could be the existence of frequent multiple grain boundaries between the crossed NWs in the bridges shown in Figures 3.21b and d, indicated by the orange highlighted dotted circle. To study this further, a typical electrical measurement was conducted on a hydrothermally grown twin nanowire with a grain boundary (inset of Figure 3.21e). The *I-V* characteristics were found to be nonlinear as the dotted circle indicated in Figure 3.21e and clearly described in the bottom right inset. Considering the small quantity of impurities such as Co, Cd, Ni, and Fe present in the ≥ 99% Zn $(NO_3)_2 \cdot 6H_2O$ salt precursor, it is likely that some impurities segregated at the NW grain boundaries. This would result in the varistor-like nonlinear *I-V* characteristics by forming electrostatic potential barriers across the multigrain boundaries [79-82].

Additionally, using ZnO seeds as electrodes, large scale well-aligned arrays of NW bridges were grown. Figure 3.22 shows SEM images of horizontally-aligned nanowires across the nanotrench arrays. The width of each trench is about 500 nm. In Figures 3.22a and b, sparsely grown ZnO NWs span across each nanotrench, forming a network of horizontal nanowire bridges. These NWs have a uniform diameter of ~50 nm. As the growth time increased, the NW network density increased, as indicated in Figures 3.22c and d. The frequency of crossed NWs is low (Figure 3.22d).

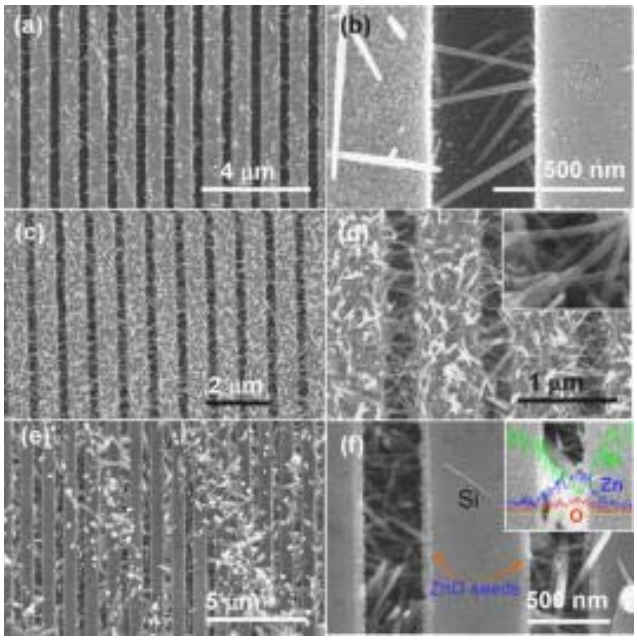

Figure 3.22 Bridged ZnO nanowire arrays across a 500 nm nanotrench array with different densities, where (a) and (b) are the most sparse, (c) and (d) are the most dense, and (e) and (f) are the most dense ones following removal of the ZnO NWs on the top region [78].

The nanowires on the top surfaces were removed by sweeping across the surface of the substrate as shown in Figure 3.22e. Figure 3.22f is a magnified SEM image showing the densely packed nanowire bridges embedded in two nanotrenches. A layer of ~50 nm ZnO seeds can be seen as indicated by the orange arrowheads.

3.5.4 Brief Summary

In summary, laterally bridged NWs were grown across trenched Au/Si, Au/SiO2/Si, and ZnO/Si electrodes in this section. The technique shows a low temperature (80 °C) approach for growing ZnO NWs on a prepatterned substrate. *I-V* characteristics of the NWs were measured and the electrical behavior was analyzed. The

bridged NW arrays represent a useful platform for fabricating gas, chemical, or biochemical nanosensor arrays.

3.6 References

[1] S. Yamabi and H. Imai, "Growth conditions for wurtzite zinc oxide films in aqueous solutions," *Journal of Materials Chemistry,* vol. 12, pp. 3773-3778, 2002.

[2] I. V. Markov, "Crystal Growth For Beginners: Fundamentals of Nucleation, Crystal Growth, and Epitaxy," World Scientific Publishing, 1995.

[3] M. J. B. S.A. Morin, J. Tong, S. Jin, "Mechanism and Kinetics of Spontaneous Nanotube Growth Driven by Screw Dislocations," *Science,* vol. 328, pp. 476-480, 2010.

[4] J. G. Strom and H. W. Jun, "Kinetics of Hydrolysis of Methenamine," *Journal of Pharmaceutical Sciences,* vol. 69, pp. 1261-1263, 1980.

[5] A. Sugunan, H. C. Warad, M. Boman, and J. Dutta, "Zinc oxide nanowires in chemical bath on seeded substrates: Role of hexamine," *Journal of Sol-Gel Science and Technology,* vol. 39, pp. 49-56, Jul 2006.

[6] M. Law, L. E. Greene, J. C. Johnson, R. Saykally, and P. D. Yang, "Nanowire dye-sensitized solar cells," *Nature Materials,* vol. 4, pp. 455-459, Jun 2005.

[7] M. H. Huang, Y. Y. Wu, H. Feick, N. Tran, E. Weber, and P. D. Yang, "Catalytic growth of zinc oxide nanowires by vapor transport," *Advanced Materials,* vol. 13, pp. 113-116, Jan 16 2001.

[8] Z. L. Wang and J. H. Song, "Piezoelectric nanogenerators based on zinc oxide nanowire arrays," *Science,* vol. 312, pp. 242-246, Apr 14 2006.

[9] X. D. Wang, J. H. Song, J. Liu, and Z. L. Wang, "Direct-current nanogenerator driven by ultrasonic waves," *Science,* vol. 316, pp. 102-105, Apr 6 2007.

[10] N. Saito, H. Haneda, T. Sekiguchi, N. Ohashi, I. Sakaguchi, and K. Koumoto, "Low-temperature fabrication of light-emitting zinc oxide micropatterns using self-assembled monolayers," *Advanced Materials,* vol. 14, pp. 418-+, Mar 18 2002.

[11] J. B. Cui, C. P. Daghlian, U. J. Gibson, R. Pusche, P. Geithner, and L. Ley, "Low-temperature growth and field emission of ZnO nanowire arrays," *Journal of Applied Physics,* vol. 97, pp. -, Feb 15 2005.

[12] P. D. Yang, H. Q. Yan, S. Mao, R. Russo, J. Johnson, R. Saykally, N. Morris, J. Pham, R. R. He, and H. J. Choi, "Controlled growth of ZnO nanowires and their optical properties," *Advanced Functional Materials,* vol. 12, pp. 323-331, May 2002.

[13] W. I. Park, G. C. Yi, M. Y. Kim, and S. J. Pennycook, "ZnO nanoneedles grown vertically on Si substrates by non-catalytic vapor-phase epitaxy," *Advanced Materials,* vol. 14, pp. 1841-1843, Dec 17 2002.

[14] J. J. Wu and S. C. Liu, "Low-temperature growth of well-aligned ZnO nanorods by chemical vapor deposition," *Advanced Materials,* vol. 14, pp. 215-+, Feb 5 2002.

[15] L. Vayssieres, "Growth of arrayed nanorods and nanowires of ZnO from aqueous solutions," *Advanced Materials,* vol. 15, pp. 464-466, Mar 4 2003.

[16] L. Vayssieres, K. Keis, S. E. Lindquist, and A. Hagfeldt, "Purpose-built anisotropic metal oxide material: 3D highly oriented microrod array of ZnO," *Journal of Physical Chemistry B,* vol. 105, pp. 3350-3352, May 3 2001.

[17] C. C. Lin, S. Y. Chen, and S. Y. Cheng, "Nucleation and growth behavior of well-aligned ZnO nanorods on organic substrates in aqueous solutions," *Journal of Crystal Growth,* vol. 283, pp. 141-146, Sep 15 2005.

[18] L. E. Greene, M. Law, J. Goldberger, F. Kim, J. C. Johnson, Y. F. Zhang, R. J. Saykally, and P. D. Yang, "Low-temperature wafer-scale production of ZnO nanowire arrays," *Angewandte Chemie-International Edition,* vol. 42, pp. 3031-3034, 2003.

[19] L. E. Greene, M. Law, D. H. Tan, M. Montano, J. Goldberger, G. Somorjai, and P. D. Yang, "General route to vertical ZnO nanowire arrays using textured ZnO seeds," *Nano Letters,* vol. 5, pp. 1231-1236, Jul 2005.

[20] P. X. Gao, J. H. Song, J. Liu, and Z. L. Wang, "Nanowire piezoelectric nanogenerators on plastic substrates as flexible power sources for nanodevices," *Advanced Materials,* vol. 19, pp. 67-+, Jan 8 2007.

[21] X. D. Wang, C. J. Summers, and Z. L. Wang, "Large-scale hexagonal-patterned growth of aligned ZnO nanorods for nano-optoelectronics and nanosensor arrays," *Nano Letters,* vol. 4, pp. 423-426, Mar 2004.

[22] Y. J. Kim, C. H. Lee, Y. J. Hong, G. C. Yi, S. S. Kim, and H. Cheong, "Controlled selective growth of ZnO nanorod and microrod arrays on Si substrates by a wet chemical method," *Applied Physics Letters,* vol. 89, pp. -, Oct 16 2006.

[23] B. S. Kang, S. J. Pearton, and F. Ren, "Low temperature (< 100 degrees C) patterned growth of ZnO nanorod arrays on Si," *Applied Physics Letters,* vol. 90, pp. -, Feb 19 2007.

[24] T. L. Sounart, J. Liu, J. A. Voigt, J. W. P. Hsu, E. D. Spoerke, Z. Tian, and Y. B. Jiang, "Sequential nucleation and growth of complex nanostructured films," *Advanced Functional Materials,* vol. 16, pp. 335-344, Feb 3 2006.

[25] B. Weintraub, Y. L. Deng, and Z. L. Wang, "Position-controlled seedless growth of ZnO nanorod arrays on a polymer substrate via wet chemical synthesis," *Journal of Physical Chemistry C,* vol. 111, pp. 10162-10165, Jul 19 2007.

[26] J. B. Cui and U. J. Gibson, "Enhanced nucleation, growth rate, and dopant incorporation in ZnO nanowires," *Journal of Physical Chemistry B,* vol. 109, pp. 22074-22077, Nov 24 2005.

[27] I. S. Ahuja, C. L. Yadava, and R. Singh, "Tetradentate Behavior of Hexamethylenetetramine," *Journal of Molecular Structure,* vol. 81, pp. 289-291, 1982.

[28] K. Govender, D. S. Boyle, P. B. Kenway, and P. O'Brien, "Understanding the factors that govern the deposition and morphology of thin films of ZnO from aqueous solution," *Journal of Materials Chemistry,* vol. 14, pp. 2575-2591, 2004.

[29] Z. Wang, X. F. Qian, J. Yin, and Z. K. Zhu, "Large-scale fabrication of tower-like, flower-like, and tube-like ZnO arrays by a simple chemical solution route," *Langmuir,* vol. 20, pp. 3441-3448, Apr 13 2004.

[30] L. G. Yu, G. M. Zhang, S. Q. Li, Z. H. Xi, and D. Z. Guo, "Fabrication of arrays of zinc oxide nanorods and nanotubes in aqueous solution under an external voltage," *Journal of Crystal Growth,* vol. 299, pp. 184-188, Feb 1 2007.

[31] J. Zhang, L. D. Sun, C. S. Liao, and C. H. Yan, "A simple route towards tubular ZnO," *Chemical Communications,* pp. 262-263, 2002.

[32] J. Zhang, L. D. Sun, J. L. Yin, H. L. Su, C. S. Liao, and C. H. Yan, "Control of ZnO morphology via a simple solution route," *Chemistry of Materials,* vol. 14, pp. 4172-4177, Oct 2002.

[33] Z. Wang, X. F. Qian, J. Yin, and Z. K. Zhu, "Aqueous solution fabrication of large-scale arrayed obelisk-like zinc oxide nanorods with high efficiency," *Journal of Solid State Chemistry,* vol. 177, pp. 2144-2149, Jun 2004.

[34] M. Izaki and T. Omi, "Electrolyte optimization for cathodic growth of zinc oxide films," *Journal of the Electrochemical Society,* vol. 143, pp. L53-L55, Mar 1996.

[35] A. Chatterjee and J. Foord, "Electrochemical deposition of nanocrystalline zinc oxide at conductive diamond electrodes," *Diamond and Related Materials,* vol. 15, pp. 664-667, Apr-Aug 2006.

[36] B. Q. Cao, W. P. Cai, F. Q. Sun, Y. Li, Y. Lei, and L. D. Zhang, "Fabrication of large-scale zinc oxide ordered pore arrays with controllable morphology," *Chemical Communications,* pp. 1604-1605, 2004.

[37] B. Q. Cao, Y. Li, G. T. Duan, and W. P. Cai, "Growth of ZnO nanoneedle arrays with strong ultraviolet emissions by an electrochemical deposition method," *Crystal Growth & Design,* vol. 6, pp. 1091-1095, May 2006.

[38] L. Dai, X. L. Chen, W. J. Wang, T. Zhou, and B. Q. Hu, "Growth and luminescence characterization of large-scale zinc oxide nanowires," *Journal of Physics-Condensed Matter,* vol. 15, pp. 2221-2226, Apr 9 2003.

[39] X. L. Wu, G. G. Siu, C. L. Fu, and H. C. Ong, "Photoluminescence and cathodoluminescence studies of stoichiometric and oxygen-deficient ZnO films," *Applied Physics Letters,* vol. 78, pp. 2285-2287, Apr 15 2001.

[40] B. Weintraub, Zhou, Z. Z., Li, Y. H., Deng, Y., "Solution Synthesis of One-Dimensional ZnO Nanomaterials and their Applications," *Nanoscale,* 2010 (to appear).

[41] Z. L. Wang, "The new field of nanopiezotronics," *Materials Today,* vol. 10, pp. 20-28, May 2007.

[42] W. I. Milne, K. B. K. Teo, G. A. J. Amaratunga, P. Legagneux, L. Gangloff, J. P. Schnell, V. Semet, V. T. Binh, and O. Groening, "Carbon nanotubes as field emission sources," *Journal of Materials Chemistry,* vol. 14, pp. 933-943, 2004.

[43] W. M. Bai X, Zhang GM,Yu J, Zhang ZX, Guo DZ, Zhao X Y and Xue Z Q, "Field emission of individual carbon nanotubes on tungsten tips," *J. Vac. Sci. Technol. B,* vol. 25, pp. 561-565, 2007.

[44] W. A. Deheer, A. Chatelain, and D. Ugarte, "A Carbon Nanotube Field-Emission Electron Source," *Science,* vol. 270, pp. 1179-1180, Nov 17 1995.

[45] Y. Qin, X. D. Wang, and Z. L. Wang, "Microfibre-nanowire hybrid structure for energy scavenging," *Nature,* vol. 451, pp. 809-U5, Feb 14 2008.

[46] C. S. Lao, J. Liu, P. X. Gao, L. Y. Zhang, D. Davidovic, R. Tummala, and Z. L. Wang, "ZnO nanobelt/nanowire Schottky diodes formed by dielectrophoresis alignment across Au electrodes," *Nano Letters,* vol. 6, pp. 263-266, Feb 2006.

[47] M. H. Huang, S. Mao, H. Feick, H. Q. Yan, Y. Y. Wu, H. Kind, E. Weber, R. Russo, and P. D. Yang, "Room-temperature ultraviolet nanowire nanolasers," *Science,* vol. 292, pp. 1897-1899, Jun 8 2001.

[48] X. J. Li and W. F. Jiang, "Enhanced field emission from a nest array of multi-walled carbon nanotubes grown on a silicon nanoporous pillar array," *Nanotechnology,* vol. 18, Feb 2007.

[49] D. Banerjee, S. H. Jo, and Z. F. Ren, "Enhanced field emission of ZnO nanowires," *Advanced Materials,* vol. 16, pp. 2028-+, Nov 2004.

[50] L. Nilsson, O. Groening, C. Emmenegger, O. Kuettel, E. Schaller, L. Schlapbach, H. Kind, J. M. Bonard, and K. Kern, "Scanning field emission from patterned carbon nanotube films," *Applied Physics Letters,* vol. 76, pp. 2071-2073, Apr 10 2000.

[51] J. M. Bonard, N. Weiss, H. Kind, T. Stockli, L. Forro, K. Kern, and A. Chatelain, "Tuning the field emission properties of patterned carbon nanotube films," *Advanced Materials,* vol. 13, pp. 184-188, Feb 5 2001.

[52] K. B. K. Teo, M. Chhowalla, G. A. J. Amaratunga, W. I. Milne, G. Pirio, P. Legagneux, F. Wyczisk, D. Pribat, and D. G. Hasko, "Field emission from dense, sparse, and patterned arrays of carbon nanofibers," *Applied Physics Letters,* vol. 80, pp. 2011-2013, Mar 18 2002.

[53] X. D. Wang, J. Zhou, C. S. Lao, J. H. Song, N. S. Xu, and Z. L. Wang, "In situ field emission of density-controlled ZnO nanowire arrays," *Advanced Materials,* vol. 19, pp. 1627-+, Jun 18 2007.

[54] C. J. Park, D. K. Choi, J. Yoo, G. C. Yi, and C. J. Lee, "Enhanced field emission properties from well-aligned zinc oxide nanoneedles grown on the Au/Ti/n-Si substrate," *Applied Physics Letters,* vol. 90, Feb 2007.

[55] J. P. Liu, X. T. Huang, Y. Y. Li, X. X. Ji, Z. K. Li, X. He, and F. L. Sun, "Vertically aligned 1D ZnO nanostructures on bulk alloy substrates: Direct solution synthesis, photoluminescence, and field emission," *Journal of Physical Chemistry C,* vol. 111, pp. 4990-4997, Apr 5 2007.

[56] X. D. Wang, J. H. Song, C. J. Summers, J. H. Ryou, P. Li, R. D. Dupuis, and Z. L. Wang, "Density-controlled growth of aligned ZnO nanowires sharing a common contact: A simple, low-cost, and mask-free technique for large-scale applications," *Journal of Physical Chemistry B,* vol. 110, pp. 7720-7724, Apr 20 2006.

[57] Z. Tang, Wang, Y., Podsiadlo, P., Kotov, N.A., "Biomedical Applications of Layer-by-Layer Assembly: From Biomimetics to Tissue Engineering," *Advanced Materials,* vol. 18, pp. 3203 - 3224, 2006.

[58] G. Decher, J. D. Hong, and J. Schmitt, "Buildup of Ultrathin Multilayer Films by a Self-Assembly Process .3. Consecutively Alternating Adsorption of Anionic and

Cationic Polyelectrolytes on Charged Surfaces," *Thin Solid Films,* vol. 210, pp. 831-835, Apr 30 1992.

[59] C. Y. Jiang, S. Markutsya, Y. Pikus, and V. V. Tsukruk, "Freely suspended nanocomposite membranes as highly sensitive sensors," *Nature Materials,* vol. 3, pp. 721-728, Oct 2004.

[60] B. Weintraub, S. Chang, S. Singamaneni, W. H. Han, Y. J. Choi, J. H. Bae, M. Kirkham, V. V. Tsukruk, and Y. L. Deng, "Density-controlled, solution-based growth of ZnO nanorod arrays via layer-by-layer polymer thin films for enhanced field emission," *Nanotechnology,* vol. 19, pp. -, Oct 29 2008.

[61] C. Y. Jiang, S. Markutsya, and V. V. Tsukruk, "Collective and individual plasmon resonances in nanoparticle films obtained by spin-assisted layer-by-layer assembly," *Langmuir,* vol. 20, pp. 882-890, Feb 3 2004.

[62] C. Y. Jiang, S. Markutsya, and V. V. Tsukruk, "Compliant, robust, and truly nanoscale free-standing multilayer films fabricated using spin-assisted layer-by-layer assembly," *Advanced Materials,* vol. 16, pp. 157-+, Jan 16 2004.

[63] J. A. Forrest, K. DalnokiVeress, and J. R. Dutcher, "Interface and chain confinement effects on the glass transition temperature of thin polymer films," *Physical Review E,* vol. 56, pp. 5705-5716, Nov 1997.

[64] V. V. Gorbunov, Fuchigami,N., Tsukruk, V.V., "Microthermal Probing of Ultrathin Polymer Films," *High Performance Polymers,* vol. 12, pp. 603-610, 2000.

[65] X. Fang, Y. Bando, U. K. Gautam, C. Ye, and D. Golberg, "Inorganic semiconductor nanostructures and their field-emission applications," *Journal of Materials Chemistry,* vol. 18, pp. 509-522, 2008.

[66] W. Z. Wang, B. Q. Zeng, J. Yang, B. Poudel, J. Y. Huang, M. J. Naughton, and Z. F. Ren, "Aligned ultralong ZnO nanobelts and their enhanced field emission," *Advanced Materials,* vol. 18, pp. 3275-+, Dec 2006.

[67] Q. Ahsanulhaq, J. H. Kim, and Y. B. Hahn, "Controlled selective growth of ZnO nanorod arrays and their field emission properties," *Nanotechnology,* vol. 18, Dec 2007.

[68] T. Dasgupta, Weintraub, B., V. Roshan Joseph, "A Physical-Statistical Model for Density Control of Nanowires," *IIE Transactions-Quality and Reliability Engineering,* 2010 (to appear).

[69] C. M. Lieber, "The incredible shrinking circuit - Researchers have built nanotransistors and nanowires. Now they just need to find a way to put them all together," *Scientific American,* vol. 285, pp. 58-64, Sep 2001.

[70] C. M. Lieber and Z. L. Wang, "Functional nanowires," *Mrs Bulletin,* vol. 32, pp. 99-108, Feb 2007.

[71] X. F. Duan, Y. Huang, Y. Cui, J. F. Wang, and C. M. Lieber, "Indium phosphide nanowires as building blocks for nanoscale electronic and optoelectronic devices," *Nature,* vol. 409, pp. 66-69, Jan 4 2001.

[72] Y. Huang, X. F. Duan, Y. Cui, L. J. Lauhon, K. H. Kim, and C. M. Lieber, "Logic gates and computation from assembled nanowire building blocks," *Science,* vol. 294, pp. 1313-1317, Nov 9 2001.

[73] R. R. He, D. Gao, R. Fan, A. I. Hochbaum, C. Carraro, R. Maboudian, and P. D. Yang, "Si nanowire bridges in microtrenches: Integration of growth into device fabrication," *Advanced Materials,* vol. 17, pp. 2098-+, Sep 5 2005.

[74] R. R. He and P. D. Yang, "Giant piezoresistance effect in silicon nanowires," *Nature Nanotechnology,* vol. 1, pp. 42-46, Oct 2006.

[75] J. S. Lee, M. S. Islam, and S. Kim, "Direct formation of catalyst-free ZnO nanobridge devices on an etched Si substrate using a thermal evaporation method," *Nano Letters,* vol. 6, pp. 1487-1490, Jul 12 2006.

[76] J. F. Conley, L. Stecker, and Y. Ono, "Directed integration of ZnO nanobridge devices on a Si substrate," *Applied Physics Letters,* vol. 87, pp. -, Nov 28 2005.

[77] Z. R. R. Tian, J. A. Voigt, J. Liu, B. McKenzie, M. J. McDermott, M. A. Rodriguez, H. Konishi, and H. F. Xu, "Complex and oriented ZnO nanostructures," *Nature Materials,* vol. 2, pp. 821-826, Dec 2003.

[78] P. X. Gao, J. Liu, B. A. Buchine, B. Weintraub, Z. L. Wang, and J. L. Lee, "Bridged ZnO nanowires across trenched electrodes," *Applied Physics Letters,* vol. 91, pp. -, Oct 1 2007.

[79] F. Oba, Y. Sato, T. Yamamoto, Y. Ikuhara, and T. Sakuma, "Current-voltage characteristics of cobalt-doped inversion boundaries in zinc oxide bicrystals," *Journal of the American Ceramic Society,* vol. 86, pp. 1616-1618, Sep 2003.

[80] G. E. Pike, S. R. Kurtz, P. L. Gourley, H. R. Philipp, and L. M. Levinson, "Electroluminescence in Zno Varistors - Evidence for Hole Contributions to the Breakdown Mechanism," *Journal of Applied Physics,* vol. 57, pp. 5512-5518, 1985.

[81] G. E. Pike and C. H. Seager, "Dc Voltage Dependence of Semiconductor Grain-Boundary Resistance," *Journal of Applied Physics,* vol. 50, pp. 3414-3422, 1979.

[82] Y. Sato, F. Oba, T. Yamamoto, Y. Ikuhara, and T. Sakuma, "Current-voltage characteristics across [0001] twist boundaries in zinc oxide bicrystals," *Journal of the American Ceramic Society,* vol. 85, pp. 2142-2144, Aug 2002.

CHAPTER 4

PHOTOVOLTAIC DEVICE FABRICATION & CHARACTERIZATION

In the last chapter, several examples were provided demonstrating highly rational ZnO nanowire synthesis using an aqueous chemistry technique. Nanowire individual position, density, length, and orientation control were achieved. In order to achieve nanowire-based electronic devices, high levels of reproducibility and synthesis control must be achieved. Building on the synthesis control realized in the previous chapter, ZnO nanowires will be implemented in dye-sensitized solar cell devices in this chapter.

4.1 Introduction

Renewable and green energy are the technological drivers of the future economy. Solar cells (SCs) are one of the most important sustainable energy technologies that have the potential to meet the worlds energy demands [1]. Among the various approaches to SCs [2-11], the performance of dye-sensitized solar cells (DSSCs) is largely influenced by the surface area of adsorbed light-harvesting molecules. Traditional DSSCs utilize a nanoparticle film for enhancing the SC conversion efficiency [12, 13]. Photons absorbed by the dye monolayer create excitons that are rapidly split at the surface of the nanoparticles. After splitting, electrons are injected into the nanoparticles and holes move towards the opposite electrode by means of a redox species in an electrolyte. The surface area of the nanoparticle film and the effectiveness of charge collection by the electrodes determine the photovoltaic efficiency of the cell. The latter property has been improved

by using aligned ZnO nanowire (NW) arrays, which provide direct electrical pathways for rapid collection of carriers generated throughout the device, and a full-sun efficiency of 1.5 % has been demonstrated [14]. However, the design is still based on a two-dimensional (2D) planar substrate, which has a relatively low surface area that limits the dye loading capacity and restricts mobility and adaptability for remote operation. Moreover, the increasing surface area is limited by the requirement that the electron transport distance d remains significantly smaller than the electron diffusion length L_n in order to minimize recombination of electrons with holes or other species. For wire-based SCs, in which light is illuminated perpendicular to the wire,[15, 16] the shadow effect from the entangled wire shaped electrode may limit the enhancement in power efficiency.

In this chapter, an innovative hybrid structure is demonstrated that integrates optical fibers and nanowire (NW) arrays as three-dimensional (3D) dye-sensitized solar cells (DSSCs) that have a significantly enhanced energy conversion efficiency. The ZnO NWs grow normal to the optical fiber surface and enhance the surface area for the interaction of light with dye molecules. The light illuminates the fiber from one end along the axial direction, and its internal reflection within the fiber creates multiple opportunities for energy conversion at the interfaces.

4.2 Approach

The DSSC hybrid structure integrates optical fibers and ZnO NWs grown by a chemical approach on the fiber surfaces. The design principle is shown in Figure 4.1. The main structure consists of a bundle of quartz fibers arranged such that the incident sunlight can enter the fibers from one end (Figure 4.1a). The upper region of the fibers

functions to effectively guide light for concealed and adaptable applications. The fiber surface is coated with a low-refractive-index cladding layer for minimizing light loss. The DSSC is fabricated on the lower region of the fiber surface, which can be situated remotely from the top surface where incoming light enters the fiber. This segment of the fiber, which lacks a cladding layer, is first coated with an indium tin oxide (ITO) layer that simultaneously acts as a conductive electrode and a high-refractive-index material that allows light to escape the fiber and enter the DSSC (Figure 4.1b). A thin layer of ZnO deposited on the ITO layer serves as a seed layer for growth of aligned ZnO NWs by a chemical approach (see Figures 4.7 and 4.9) [17]. The key principle is that the light entering from the axial direction inside the fiber experiences multiple internal reflections along the fiber. At each internal reflection at the fiber/ITO/ZnO NW interfaces, light will cross the interface to reach the dye molecules through the NWs. The effective propagation distance of light along the fiber covered with NWs is a few centimeters (see Figures 4.4 and 4.5). Therefore, the light interaction surface area is increased not only because of the NWs, but also because of the multiple reflections along the fiber. This effect does not increase the path length that electrons must travel to reach the electrode. This is the core principle behind the 3D DSSC.

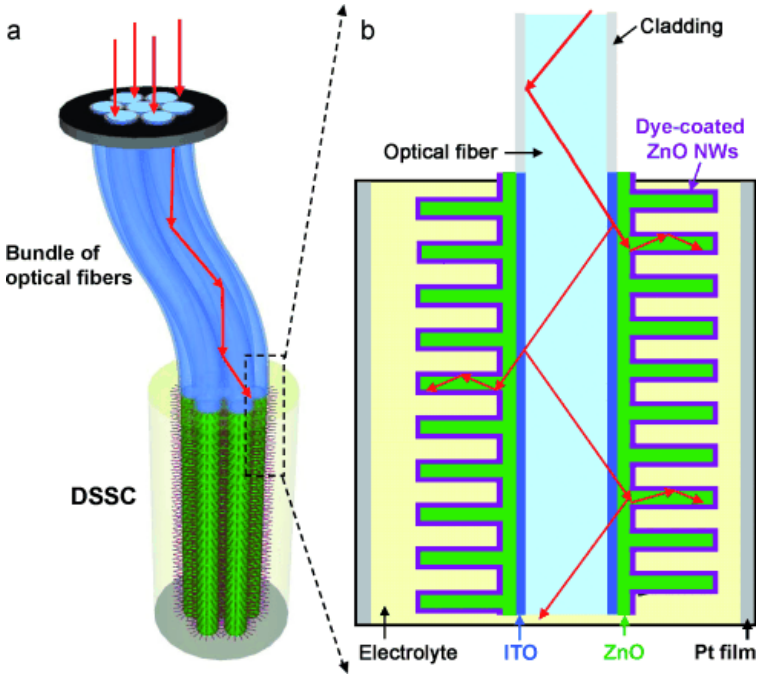

Figure 4.1 Design and principle of a three-dimensional DSSC. The cross-section of the fiber can be cylindrical or rectangular. a) The 3D DSSC is composed of optical fibers and ZnO NWs are grown vertically on the fiber surface. The top segment of the bundled optical fibers utilizes conventional optical fibers and allows for remote transmission of light. The bottom segment consists of the 3D DSSC for solar power generation at a remote/concealed location. b) Detailed structure of the 3D DSSC. [18]

4.3 Cylindrical optical fiber

4.3.1 Device fabrication procedure

To first demonstrate the 3D DSSC concept, a cell was fabricated on a cylindrical optical fiber. Cylindrical fibers were provided by OFS Optics (HCS 200). To expose the 200 μm pure silica core, the ETFE (ethylene tetrafluoroethylene) jacket was mechanically stripped and the polymer cladding (HCS) was removed with acetone. Rectangular fibers were home-made by grinding circular quartz rods into a rectangular geometry with a 2:1 aspect ratio. The rods were drawn into fiber strands under an oxygen-enriched flame. All fibers were ultrasonically cleaned in acetone, water, and

ethanol. Thin films of 300 nm ITO and 50 nm ZnO were deposited by radio frequency (RF) magnetron sputtering at room temperature. For circular fibers, the samples were oriented parallel to the sputtering target on a rotating sample stage for uniform coverage of all surfaces. For three-side-coated rectangular fibers, samples were oriented normal to the sputter target to result in thin films on only three sides. NWs were synthesized by a wet-chemical method in a Pyrex glass bottle containing 20 mM zinc chloride (Aldrich) and 20 mM hexamine (Fluka) at 95 ˚C for 16 h in a Yamato convection box oven. Aspect ratios were controlled by adding (0-5 mL in 100 mL solutions) 28 % ammonium hydroxide (Aldrich). All chemicals were reagent grade. Samples were rinsed with water and ethanol and air-dried at 95 ˚C for 12 h. Fiber tips were cleaved with a Corning diamond fiber cleaver (the manufacturer guarantees fiber end-faces that average less than 0.7˚ from the perpendicular), which ensured efficient light coupling into the fiber. The fibers were characterized on a LEO 1550 field-emission gun SEM.

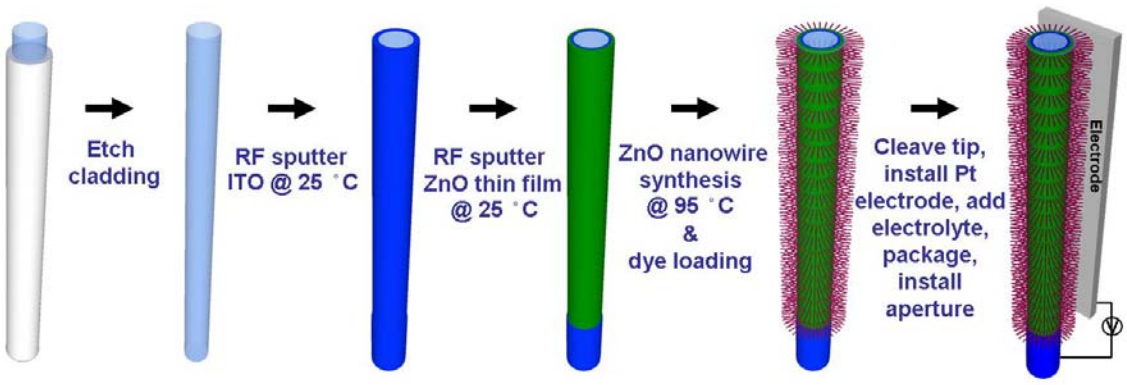

Figure 4.2 Fabrication process flow for optical fiber-nanowire hybrid structure dye-sensitized solar cell.

For 3D DSSC fabrication, the NW arrays were sensitized in a 0.5 mM N719 dye solution in dry ethanol for 1 h [19]. A Pt layer was evaporated on a precleaned glass

substrate with a Ti adhesion layer that served as the counter electrode. The working electrode fiber coated with sensitized ZnO NWs was placed in parallel with the Pt film counter electrode. The internal space of the device was filled with a liquid electrolyte (0.5 M LiI, 50 mM I_2 , 0.5 M 4-tertbutylpyridine in 3-methoxypropionitrile (Fluka)) by the capillary effect. The entire cell was fully packaged and shielded to prevent light leakage.

4.3.2 Remote functionality

One of the advantages of the optical fiber design is that the solar cell can be located at a different region than the light entry point and thus, it can function remotely. Stability due to the volatile liquid electrolyte is a challenge with high performance DSSCs. By the solar cell functioning at a remote location compared to the light entry point, more robust packaging can be employed to improve DSSC stability.

To demonstrate the remote functionality, an optical fiber-nanowire hybrid device was fabricated on a 30 cm in length OFS (HCS 200) optical fiber. The initial 26 cm including the core, cladding, and jacket was left undisturbed. The jacket and cladding from the final 4 cm was removed and the solar cell was subsequently fabricated on this region. Figure 4.3 demonstrates high intensity light (>> 1 sun) being coupled into the photoanode remotely. Qualitatively, it can be seen that >90% of the light escapes radially within the initial 1 cm of the DSSC. The dark region at the 2.5 cm region is an process defect due to poorly etched cladding. The remaining light left at the fiber tip at the 4 cm point can be reflected back into the device using a Ag paste mirror.

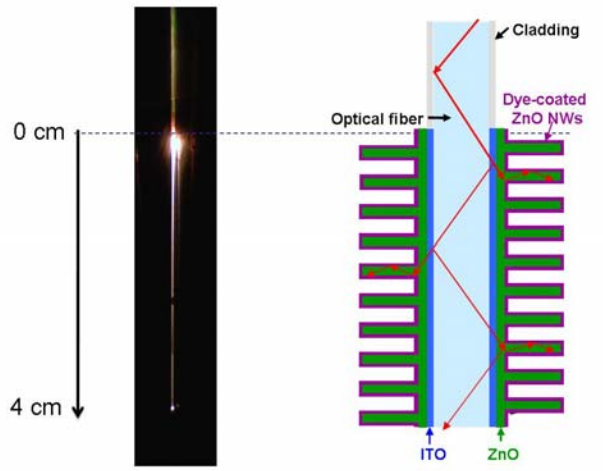

Figure 4.3 Optical image demonstrating remote functionality of optical fiber solar cell and radial light escape in the lower solar cell region.

4.3.3 Light transport measurements

Cylindrical fibers with a diameter of 1.5 mm (Thorlabs BFL37-1500) were employed for quantitative light transport measurements. The solar simulator was used as the source and a thermopile (Newport 70260) as the photodetector. This thermopile had the ability to measure light power between 60 μW- 3 W and wavelengths between 150 - 6000 nm. In these experiments, no filter was employed and the same fiber was tested at different lengths. For the cladding coated fiber (Figure 4.4a), the decay was very slow. For the fiber with cladding (Figure 4.4b), the light decayed twice as fast as the one with cladding. For the fiber with an ITO coating and ZnO NWs (Figure 4.4c), the light escaped radially within 10 cm.

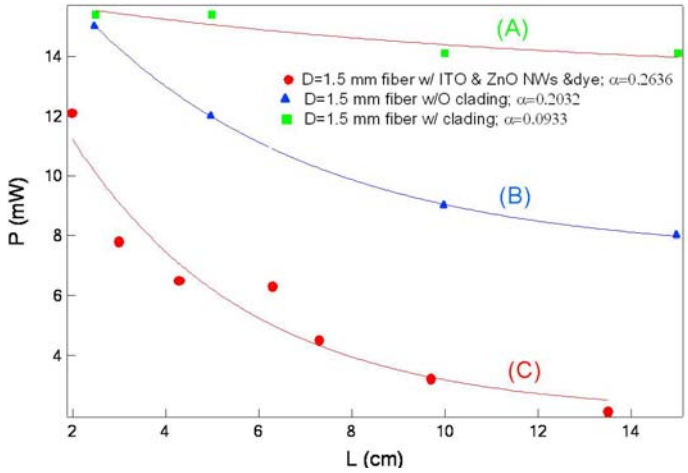

Figure 4.4 Characterization of decay of light as a function of fiber length. [18]

To study the wavelength dependence, the light attenuation along the fiber was measured using the solar simulator as the source in conjunction with color filters of wavelength 400 nm, 500 nm, 550 nm, 700 nm, and 880 nm, respectively and a thermopile as the photodetector. The same fiber was tested at different lengths. With a filter, 89.6% and 96.7% incident power were absorbed within 2 cm and 3 cm along the fiber, respectively. After curve fitting, the data follows a power decay law. Thus, all optical fiber devices processed were of lengths between 2 - 4 cm. From Figure 4.5, it can be seen that longer wavelength radiation in the visible and IR propogated further than the short wavelength UV radiation. As expected for a 1.5 mm diameter core multimode optical fiber, no color filtering was evident.

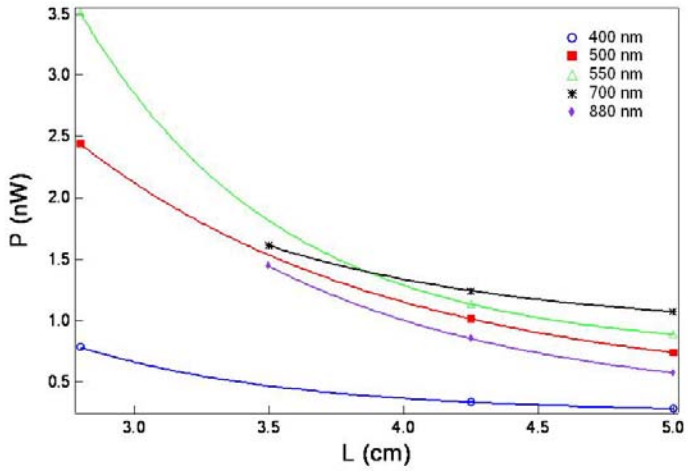

Figure 4.5 Characterization of the light transport along a cylindrical optical fiber at various wavelengths. [18]

4.3.4 Current density-voltage measurements

ZnO NWs with lengths of approximately 15 μm were synthesized on a quartz fiber with a diameter of 0.2 mm (Figure 4.6a, b). The DSSC was investigated by using a single fiber placed in parallel with a flat Pt counter electrode. Two typical configurations were considered: light illumination normal to the fiber axis (NA) and parallel to the fiber axis (PA), as shown in Figure 4.6c (insets). For the PA case, careful measurements were taken in order to eliminate light leakage at the fiber entrance (see Figure 4.1a) and accurately calculate the illumination cross-sectional area. The plot of current density against voltage (J-V curve) shows the open circuit voltage V_{OC} , short-circuit current density J_{SC} , fill factor FF, and energy conversion efficiency $=FFxV_{OC}xJ_{SC}/P_{in}$, where P_{in} is the incident light power density. It is apparent that the axial illumination configuration yields an enhanced efficiency. To properly characterize the enhancement in energy conversion efficiency, the efficiency enhancement factor EEF is defined as the ratio of power efficiencies for the PA and NA cases, that is, $EEF=\eta_{PA}/\eta_{NA}$. For a total of five

DSSCs, the EEF ranges from 4 to 18 (Figure 4.6d). The large value is partially due to the hybrid structure and partially to the geometrical configuration of the Pt film electrode. The electrode was fabricated by depositing a thin film of Pt on a glass substrate. The configuration of the Pt counter electrode is important for deciding the collection efficiency of the holes. The flat Pt electrode can effectively collect the holes generated at the bottom surface of the fiber adjacent to the electrode, but the holes generated at the upper surface may not reach the electrode before recombining with electrons and/or other species in electrolyte. Moreover, in such a design configuration, the most effective power generation portion is the upper part of the fiber that directly faces the sunlight, while the sunlight is largely attenuated once it penetrates through the ZnO NWs, ITO layer, and fiber to reach the bottom surface of the fiber. This attenuation is part of the reason that the EEF is high but the absolute energy conversion efficiency is low for this configuration. Most importantly, this result provides proof of the design concept presented in Figure 4.1 for a 3D DSSC. The short-circuit current density J_{SC} for the PA case is much higher than that for the NA case, while the open-circuit voltage V_{OC} for the PA case is significantly lower than that for the NA case. This difference occurs as the lower local incident light intensity at the ZnO-dye interface is lower in the PA case than in the NA case because of multiple internal reflections in the fiber (see Figure 4.11a).

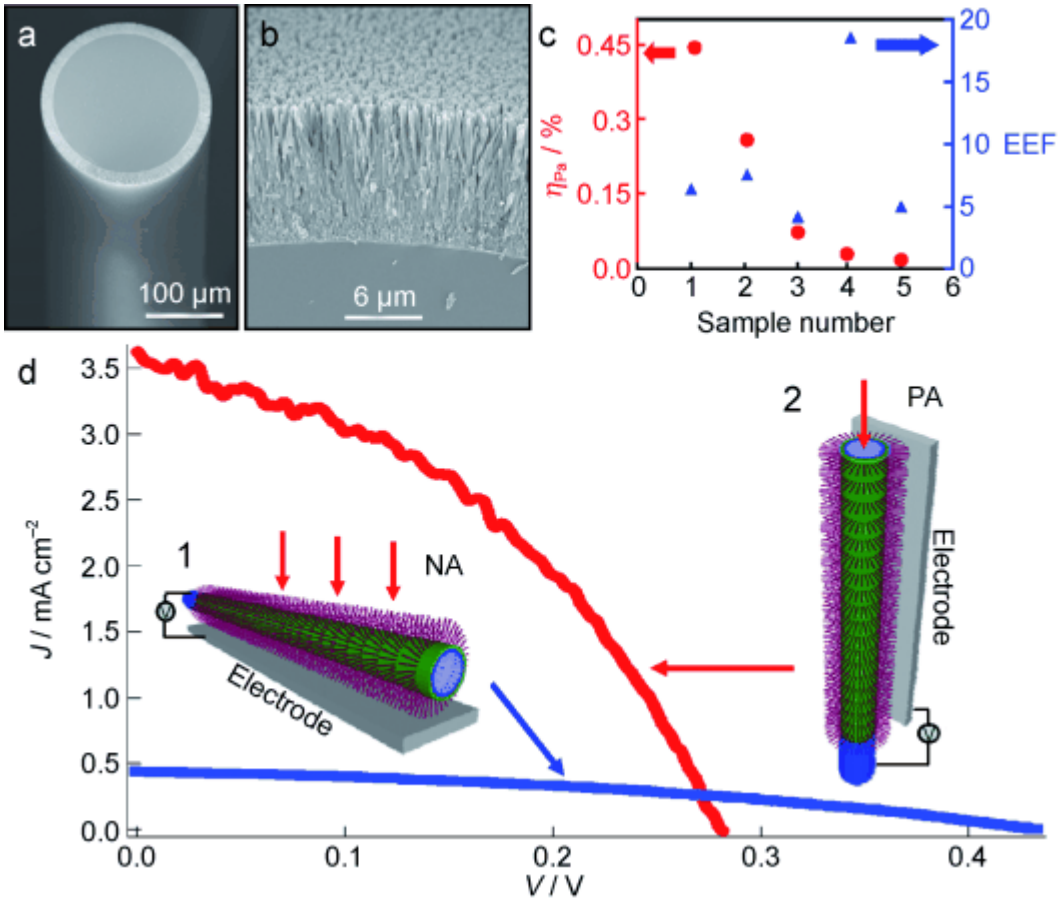

Figure 4.6 Cylindrical optical-fiber-based 3D DSSC and its performance. a) Low-magnification SEM image of a quartz fiber with uniformly grown ZnO NWs on its surface. b) High-magnification SEM image showing the densely packed ZnO NWs on the fiber surface. c) Plot of EEF and the corresponding energy conversion efficiencies for five 3D DSSCs. The data variation is mainly attributed to fluctuations in SC packaging. d) J-V curves of the DSSC under one full-sun illumination (AM 1.5 illumination, 100 mW cm^{-2}). The illumination is 1) normal to the fiber axis (NA; 2D case) and 2) parallel to the fiber axis (PA; 3D case). For the NA case, J_{sc}=0.44 mA cm^{-2}, V_{oc}=0.433 V, FF=0.375, η_{NA}=0.071 %. For the PA case, J_{sc}=3.73 mA cm^{-2}, V_{oc}=0.283 V, FF=0.414, η_{PA}=0.44 %. A corresponding efficiency enhancement factor of EEF=6.1 has been achieved by converting the 2D DSSC to 3D DSSC. [18]

However, the absolute efficiency of the cylindrical fiber in the PA case is still limited (Figure 4.6d), mainly by the curved geometry of the fiber and the short mean free path of the generated charges (case 2 in Figure 4.6d). The highest efficiency that was achieved with this configuration was 0.45 %. The flat Pt film electrode can effectively collect the photon-induced holes created at the side surface of the fiber adjacent to the electrode, but

the holes generated at the opposite surface may not reach the electrode before recombining with electrons or other species [13]. An ideal solution to capture all of the holes is to use a cylindrical, tube-shaped electrode to enclose the fiber, but this design is difficult to achieve in practice with DSSCs. An improved design takes advantage of the rectangular optical fiber geometry.

4.4 Rectangular Optical fiber

The motivation for using a rectangular fiber is the gain in effective contact area between the fiber and the flat Pt electrode for efficient collection of photon-induced holes in the electrolyte.

4.4.1 Four-sided rectangular fiber device fabrication procedure

Nanowire length has a profound effect on DSSC performance. Long nanowires maximize the effective surface area for dye loading, but on the otherhand, short nanowires allow for more efficient charge carrier collection. To this end, various experiments were devised to control the nanowire length. Well-aligned nanowires with diameters of 50-100 nm and lengths of 4 um can be seen as in Figure 4.7. Thin films of ITO (200-300 nm) and ZnO (100 nm) were deposited via RF magnetron sputtering. The ITO/ZnO thin film coated rectangular fibers were immersed in equal molar aqueous solutions of 25 mM $Zn(NO_3)_2$ and hexamethylenetetramine for 12 hours at 80ºC. Subsequently, they were rinsed with DI water and ethanol several times and dried in a box oven for 1 hour at 80 ºC.

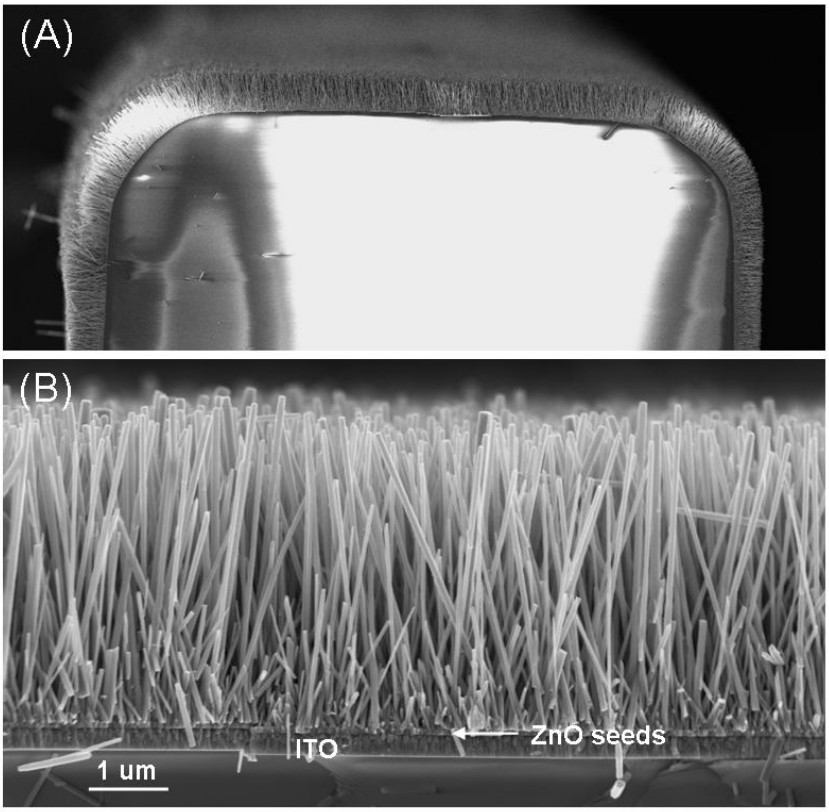

Figure 4.7 SEM images of ZnO nanowires grown on the surfaces of a rectangular fiber, showing uniform coating around its surfaces. [18]

It was found experimentally that charge carriers generated in single crystalline ZnO nanowires of lengths less than 25 μm could efficiently be collected [14]. Thus, subsequent efforts were towards synthesizing nanowires of these lengths. The approach was to introduce ammonium hydroxide to further promote supersaturation. In this way, heterogeneous nucleation would be preferred over homogeneous nucleation. NWs were synthesized by a wet-chemical method in a Pyrex glass bottle containing 20 mM zinc chloride (Aldrich) and 20 mM hexamine (Fluka) at 95 ˚C for 16 h in a Yamato convection box oven. Aspect ratios were controlled by adding (5 mL in 100 mL solutions) 28 % ammonium hydroxide (Aldrich). All chemicals were reagent grade.

Samples were rinsed with water and ethanol and air-dried at 95 ˚C for 12 h. The fiber substrates were fully immersed in the nutrient solution to promote nanowire growth on all four surfaces. SEM results of the long nanowires can be seen in Figure 4.8a and b. Length of ~15 μm and diameters of ~200 nm are evident. The rectangular fibers were custom drawn by Friedrich & Dimmock, Inc. and had dimensions of 500 μm by 100 μm with tolerances of ±50 μm.

4.4.2 Current density-voltage measurements

The electrical performance for rectangular optical fiber devices comparing the PA and NA orientation can be seen in Figure 4.8c. Similar to the cylindrical fiber case, in the PA orientation, J_{sc} is higher and the V_{oc} is lower compared to the NA orientation. The best devices had a notably high J_{sc}=10 mA/cm^2 owing to the multiple reflection of light propagating within the optical fiber creating an extended optical path length. The Figure 3.8c inset shows the EEF for a few samples, which can be as high as 26. However, these values are only approximations. When nanowires are coated on all four surfaces much of the incoming light in the NA orientation is attenuated before interacting with the bottom junction region. Thus, NA efficiencies are low for this reason and a quantitative EEF value cannot be determined for a 4-sided rectangular optical fiber device. This problem will be address later in the chapter by employing a 3-side coated rectangular fiber.

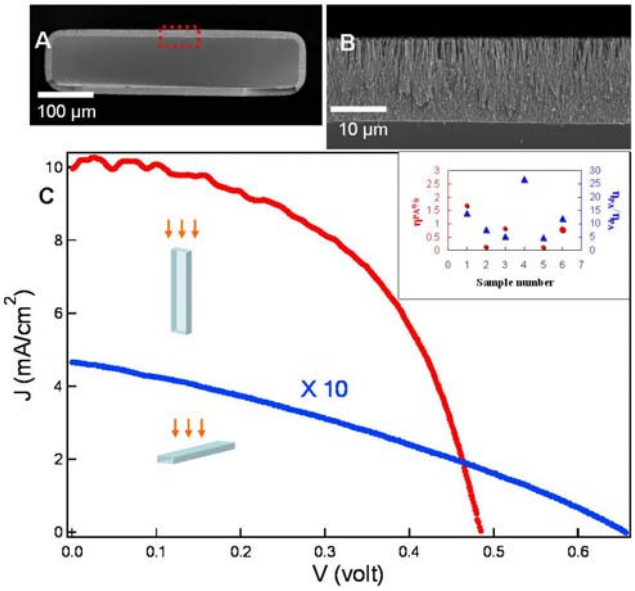

Figure 4.8 A rectangular fiber with nanowires grown around the entire circumference, and the corresponding DSSC performance when the incident light illuminates along the normal-to-axis and parallel-to-axis orientations. [18]

4.4.3 Three-sided rectangular fiber device fabrication procedure

ZnO NWs can be grown uniformly on all four sides of a fiber (see Figure 4.8), but to accurately compare the performance of the NA and PA cases, long NWs of lengths around 25 µm [21] and diameter 200 nm were grown on only three sides of the fiber (Figure 4.10a, b). It was found experimentally that the longer NWs resulted in higher efficiencies. NW arrays around 25 µm in length were the longest grown using a chemical approach. One of the challenges associated with growing ultra-long NWs is the dense film formed adjacent to the fiber because of the lateral growth of the NWs. Optical and SEM images of the 3-sided rectangular optical fiber-nanowire photoanode before and after dye-loading can be seen in Figure 4.9.

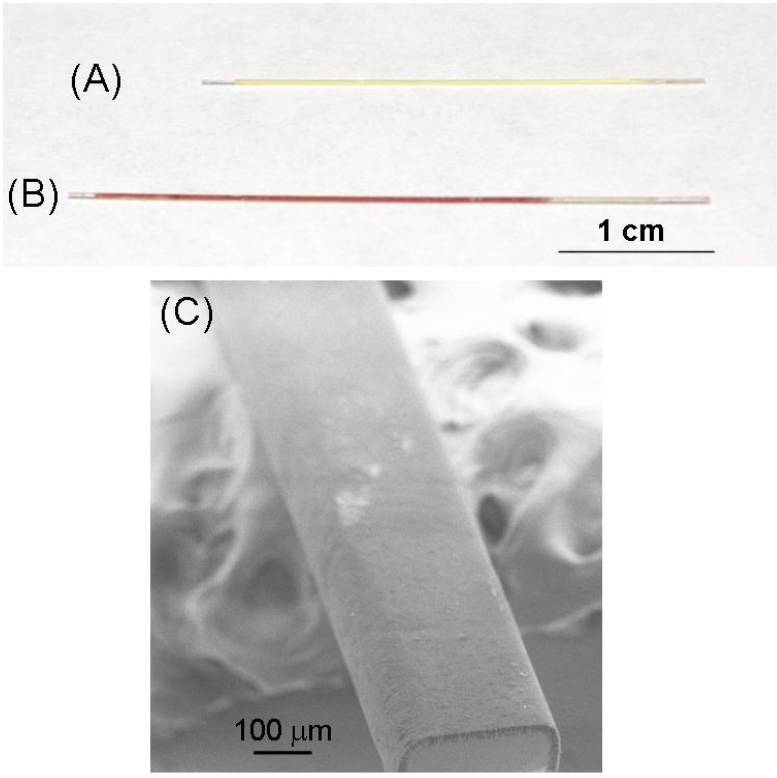

Figure 4.9 (A) Optical image of a rectangular fiber with ZnO NWs grown on the surface. (B) Optical image of the fiber after dye loading on NW surfaces. (C) SEM image of the fiber with NWs grown on surface before dye loading. [18]

For 3D DSSC output measurements, the solar cell was irradiated using a solar simulator (300 W Model 91160, Newport) with an AM 1.5 spectrum distribution calibrated against a NREL reference cell to accurately simulate a full-sun intensity (100 mW cm^{-2}). The J-V curve was measured under two configurations: light illumination normal to the fiber axis (NA) and parallel to the fiber axis (PA; Figure 4.6d and Figure 4.10d). For the PA case, the optical fiber was completely shielded by black scotch tape except for the tip, where light could couple with the fiber. Intensity-dependent measurements below 1.4 full-sun intensity were carried out with a set of neutral density

filters and by adjusting the input power of the solar simulator. To increase the light intensity up to 14 suns for high intensity solar measurements, two converging lenses were placed in between the light source and the DSSC.

The effective surface area or roughness factor (RF) is defined as the total film area per unit substrate. The measured RF is 267 for the three-sided rectangular fiber and 196 for the circular fiber. RF was measured by UV/Vis spectroscopy by desorbing the dye in an alkaline aqueous solution. The calculation of the roughness factor for the NA case is straightforward because the incident light intensity is fairly uniform across the illumination area. For the PA case, the intensity of the incident light decays as the light travels along the axis. The calculated roughness factor may not truly affect the roughness factor.

4.4.4 Current density-voltage measurements

In the NA illumination case (case 1 in Figure 4.10d), which was designed to be similar to a 2D DSSC arrangement, the uncovered top surface of the fiber allows light to effectively penetrate into the fiber and reach the bottom surface, where NWs meet the Pt electrode, thus resulting in a typical energy conversion efficiency. If the top surface of the fiber had been covered by NWs, the incident light would have been significantly attenuated once it reached the bottom surface, thus resulting in a reduction in energy conversion efficiency and thus an erroneous representation of a 2D DSSC. The PA measurement was conducted using the same hybrid-structured fiber, except that the light was introduced from the end (case 2 in Figure 4.10d). The J-V curve shows a substantial difference between the two cases; most notably, the PA case has a significantly enhanced current density. For a total of eight devices, the efficiency of the 3D design for the PA

case is enhanced by a factor of up to six (Figure 4.10d). The data variation is mainly attributed to fluctuations in solar cell packaging (see Table 4.1). The absolute energy conversion efficiency reached as high as 3.3 %, which is 120 % higher than the reported value for ZnO NW DSSCs [14]. The one side of the fiber without NWs may contribute to the power conversion by serving as a mirror that reflects the light back towards the DSSC side. A drastic increase in energy conversion efficiency is therefore demonstrated when changing from the 2D illumination (NA case) to the 3D illumination (PA case).

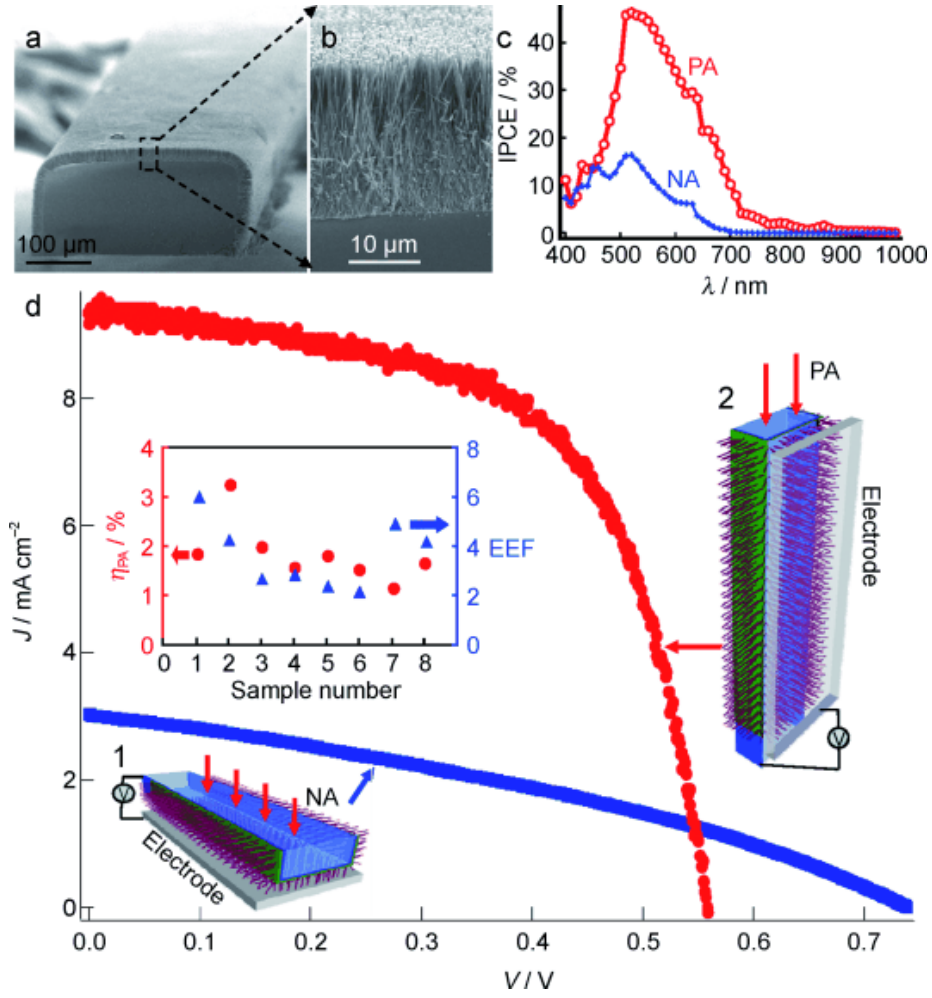

Figure 4.10 Rectangular optical-fiber-based 3D DSSC and its performance. a) Low-magnification SEM image of a quartz fiber with uniformly grown ZnO NWs on three sides. b) High-magnification SEM image showing the densely packed ZnO NWs on the fiber surface. c) Typical incident photon to electron conversion efficiency (IPCE) measured for the PA and NA cases from a DSSC. d) Current density J and voltage V curves of a DSSC under one full-sun illumination oriented 1) normal to the fiber axis (NA; 2D case) and 2) parallel to the fiber axis (PA; 3D case). For the NA case, J_{sc}=3.02 mA cm^{-2}, V_{oc}=0.739 V, FF=0.342, η_{NA}=0.76 %. For the PA case, J_{sc}=9.5 mA cm^{-2}, V_{oc}=0.559 V, FF=0.623, η_{PA}=3.3 %. A corresponding efficiency enhancement factor of EEF=4.34 has been achieved by converting the 2D DSSC to the 3D DSSC. The inset shows a plot of EEF and the corresponding energy conversion efficiencies for eight 3D DSSCs. [18]

Table 4.1 Solar cell efficiency of parallel to and normal to axis configurations measured at 1 sun intensity as plotted Figure 4.10d. [18]

η_{PA} (%)	η_{NA} (%)	EEF = η_{PA}/η_{NA}
1.91	0.31	6.16
3.3	0.76	4.34
2.02	0.77	2.62
1.85	0.57	3.25
1.83	0.77	2.38
1.5	0.71	2.12
1.1	0.23	4.82
1.76	0.39	4.51

4.4.5 External quantum efficiency measurements

The incident photon to electron conversion efficiencies (IPCE) or external quantum efficiency (EQE) is the ratio of incoming photons to the number of photo-generated electron carriers. Theoretically, the IPCE is described by the following expression:

$$IPCE(\lambda) = LHE(\lambda) \times \phi_{inj} \times \eta_c \quad (1)$$

where LHE is the light harvesting efficiency at a given wavelength, Φ_{inj} is the electron injection efficiency, η_c is the charge collection efficiency. The LHE is the fraction of photons absorbed at that wavelength, which can be described using Beer's law in the form:

$$LHE = 1 - 10^{-\varepsilon(\lambda) \times L_n \times C} \quad (2)$$

where ε(λ) is the extinction coefficient of the absorber, C is concentration (determined by photoanode roughness factor), and L_n is the diffusion length (or absorber film thickness if it is smaller).

Experimentally, IPCE measurements were carried out using a 300 W Xe lamp light source coupled to a monochromator (Oriel). A reference Si photodiode calibrated for spectral response was used for the monochromatic power-density calibration. IPCE is defined as:

$$IPCE(\lambda) = 100 \times \left[\frac{1240}{\lambda} \times \frac{resp}{Y_{ref}} \right] \times Y \tag{3}$$

where Y_{ref} is the λ-J scan for Si reference detector. Y is the λ-J scan for the actual sample. *Resp* is the responsivity curve for the Si photodetector (provided by the manufacturer). In general, responsivity measures electrical output per optical input. In other words, it measures the input-output gain of the detector system in units of [A/W].

The measured IPCE results for the PA and NA illumination cases are shown in Figure 4.10d, inset. Although the PA and NA orientations both exhibit maxima at 520 nm that correspond to the absorption maximum of the N719 dye, the PA orientation has a substantially larger absolute peak maximum compared to that of the NA curve (47 % and 17 %, respectively), thus further supporting the efficiency enhancement generated from the PA orientation. In addition, a broader photoaction in the red region is seen in the PA orientation, thus suggesting that longer-wavelength photons can be more efficiently converted to electrons farther down the optical fiber where the overall light intensity is diminished.

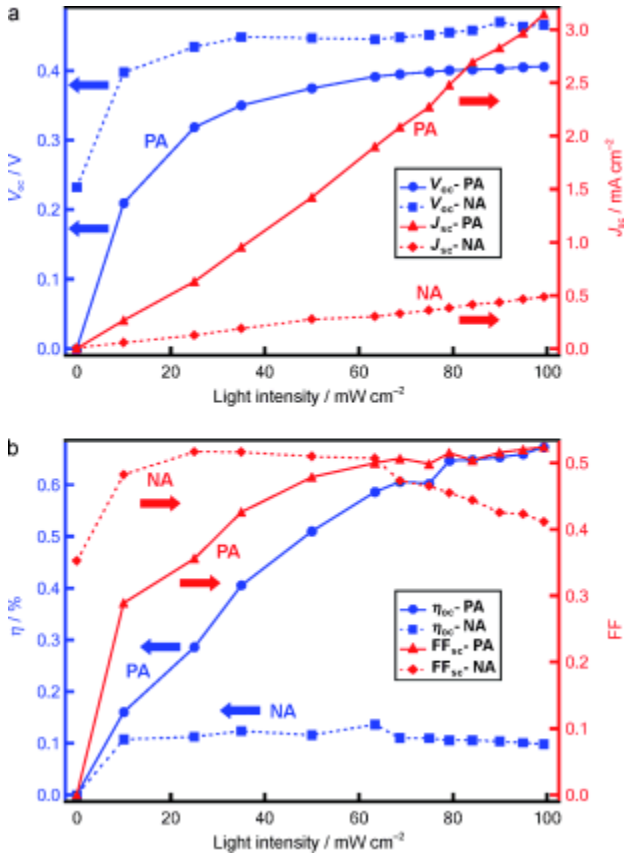

Figure 4.11 Characterization of a rectangular fiber-based 2D and 3D DSSC as a function of incident light intensity, showing the superior performance of the 3D DSSC. a) Dependence of the open-circuit voltage V_{oc} and short-circuit current density J_{sc} on incident light intensity for the NA and PA cases. b) Dependence of energy conversion efficiency and fill factor on incident light intensity for the NA and PA cases, demonstrating the largely enhanced performance of the 3D DSSC under weak light intensity to high light intensity (see Figure 4.12). [18]

4.4.6 Light intensity dependent measurements

The superior performance of the PA configuration over the NA configuration is investigated by examining the output characteristics of the DSSC as a function of incident light intensity. The open-cell voltage is significantly higher for the NA case than for the PA case (Figure 4.11a) because the local light intensity at the ZnO-dye interface is lower in the PA case than in NA case. Also, the current density in the PA case is a lot larger than that in the NA case and increases linearly with light intensity. This result

indicates that the multiple light reflections within the fiber play a role in enhancing the current output. It is noted that the efficiency of the NA case is rather flat, which is consistent with the result in reference [14], but the efficiency of the PA case increases linearly (Figure 4.11b), possibly because of the multiple reflections of the stronger light with an intensity above the threshold for receiving detectable solar power generation in the fiber. The energy conversion efficiency at one full sun for the PA case is much larger than that for the NA case. In addition, the fill factor of the NA case decreases with light intensity, while that of the PA case maintains a steadily increasing trend. These data show that the performance of the DSSC in the PA configuration outperforms that of the NA case from intensities of one full sun and below. The short-circuit current density in the PA case increases linearly and does not reach a saturation maximum until an incident light intensity of over 10 full suns (Figure 4.12), thus showing the potential of the design for concentrator applications. Although organic materials are unstable under high temperature conditions, this design could be applicable to high temperature inorganic-based photovoltaic systems.

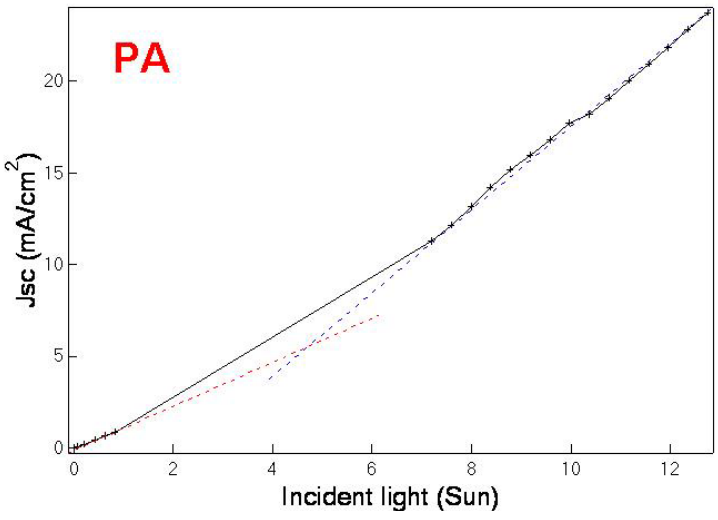

Figure 4.12 Short circuit current density versus light intensity in the PA orientation demonstrating that device does not saturate at high intensities. [18]

4.4.7 Light transport measurements

Quantitative light transport measurements were carried out to study the light attenuation versus fiber length for rectangular fibers. The samples were custom-drawn rectangular optical fibers (Friedrich & Dimmock, Inc.) with cross-sectional dimensions of 100 um x 300 um with tolerances of ±50 µm. Samples were coated with ITO and ZnO NWs on only 3 surfaces. Multiple fiber samples of various lengths were prepared. The experimental setup is shown in Figure 4.13a. Light from a 300 W Xe lamp source (Newport) was run through a monochromator (Oriel) and focused on the aperture-covered fiber top by a converging lens. The absolute power output was measured at the end of the fiber using a Si photodiode (Oriel 70282). In the experiments, it was assumed that the decrease in absolute power measured from the end of the fiber was attributed to light escaping radially. The data measured at 550, 650, and 950 nm were fit to a power decay law. Over 90% of the radiation escaped within in the initial 1-2 cm of the fiber which was used to optimize the device electrical performance. No color filtering was observed in the visible and IR region as expected for multimode optical fibers.

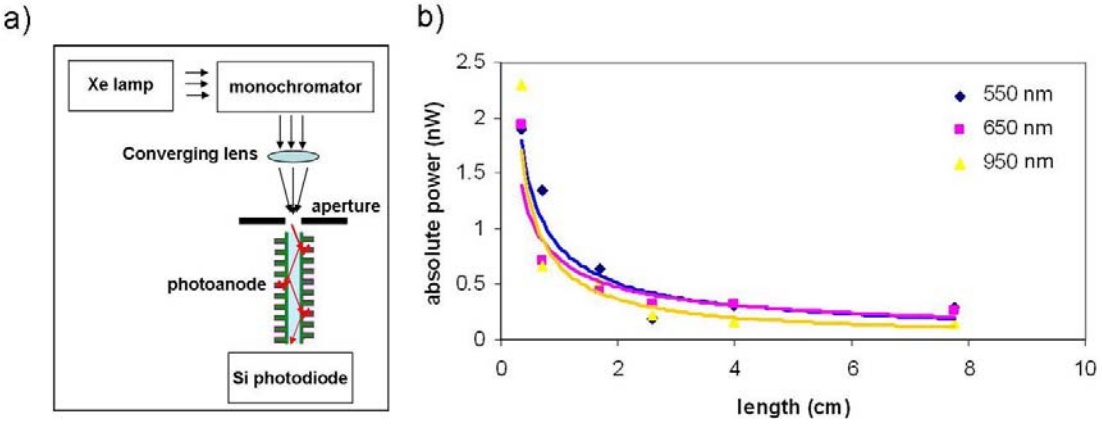

Figure 4.13 Light transport measurements for rectangular optical fiber.

4.4.8 Angular dependence measurements

Angular dependence measurements were carried out to study the light coupling and transport characteristics as a function of light entrance angle. The samples were custom-drawn rectangular optical fibers (Friedrich & Dimmock, Inc.) with cross-sectional dimensions of 100 um x 300 um with tolerances of ±50 μm. Samples were coated with ITO and ZnO NWs on only 3 surfaces. The experimental data showing the effect of coupling angle on Jsc is shown in Figure 4.14. For $\Theta<0$, initial photon interaction is with the quartz/ITO interface and for $\Theta>0$, initial photon interaction is with the quartz/air interface. At small angles, the electrical output varies depending on which interface the light strikes first, a phenomena associated with a rectangular optical fiber purposely coated with ITO/ZnO nanowires on only 3 of the 4 surfaces. The peak electrical output was found at -4˚. The variation of electrical output with coupling angle demonstrates the balance between maximizing photon/absorber interaction and extending photon propagation down fiber for multiple scattering events. In later chapters, there is future discussion on modeling studies to further study the effect of coupling angle on electrical performance.

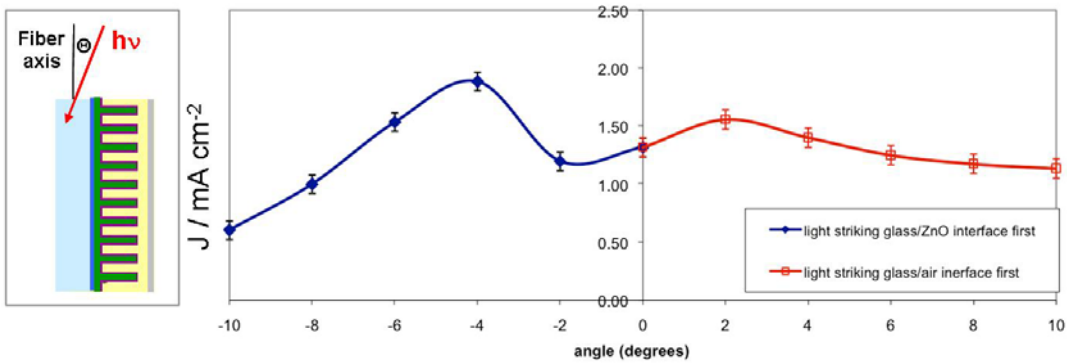

Figure 4.14 Angular dependence of 3-sided rectangular optical fiber-nanowire hybrid dye-sensitized solar cell.

4.4.9 Discussion

The use of fiber-based media for fabricating SCs is a natural choice. A fiber-shaped organic photovoltaic cell has been demonstrated by utilizing concentric thin films of small molecular organic compounds [20] The cell is illuminated at normal incidence to the fiber axis through a thin metal electrode, and exhibits a power conversion efficiency of 0.5 %. Organic photovoltaic devices have been fabricated on multimode optical fibers by constructing concentric thin films [21]. An energy conversion efficiency of 0.6 % has been measured under parallel-to-axial illumination. The approach outlined in this chapter is based on a hybrid structure that integrates an optical fiber and aligned ZnO NW arrays, which increases the light-absorbing surface area because of multiple reflections and the presence of the nanostructure. The efficiency of the 3D DSSC is enhanced by up to a factor of six compared to the 2D DSSC. The 3D DSSC, which is based on pure ZnO NWs, yields a full-sun energy conversion efficiency of up to 3.3 %, which is 120 % higher than the efficiency received using ZnO NWs on a flat substrate surface (for a review see reference [22]), 47 % higher than that produced using ZnO NWs coated with

TiO2,[23] 15 times higher than that of the hybrid polymer/ZnO NW photovoltaic devices (=0.2 %),[24] and even higher than that of the SCs made using TiO2 nanotube arrays (=2.9 %)[25] and SCs based on CdSe quantum wires/dots (=2.9 %) [6, 7]. The performance strongly suggests that the paradigm shift from 2D to 3D DSSCs offers a general approach for the development of high-efficiency SCs.

The 3D DSSC has the several outstanding features. From a physical perspective, the 2D DSSC based on NWs has a low surface area, which limits dye loading. Attempts at increasing the surface area by maximizing NW length are restricted to NW dimensions much smaller than the electron diffusion length ($d<<L_n$). The 3D DSSC is advantageous because this configuration allows light to have multiple interactions with the dye molecules without increasing the electron transport distance d. The 3D design has the following key merits for applications. Firstly, the use of fibers allows the DSSC to function remotely with high mobility. The SC unit can be concealed and located where the sunlight is available away from the surface, thus making unique designs and surface-confined applications possible. Secondly, the design concept transforms the traditional SC from action at the light illuminated side surface (e.g., 2D or projection area) to action inside the volume (e.g., 3D) of the unit, therefore allowing applications at remote locations such as underground and in deep water, in which light arrives at an exterior surface but the SC is concealed elsewhere. To produce the same amount of electricity, the 3D DSSC could have a smaller size, greater mobility, more robust design, flexible shape, and potentially lower production cost. Thirdly, the 3D DSSC has a high saturation limit and large dynamic range so that it works effectively from low light intensities below 1 sun to very high light intensities (>10 suns). Furthermore, the 3D DSSC processing

utilizes chemical synthesis at low temperatures with environmentally friendly and biologically safe materials [26], with a great potential for scale-up. Finally, since ZnO NWs can be grown on substrates of any material or shape at temperatures below 100 ˚C, [27] it is possible to replace the quartz optical fibers with highly transparent polymer fibers. By combining the hybrid structure presented here with new dyes and surface coating materials, it is possible to significantly improve the efficiency of DSSCs in general. The method outlined in this chapter provides a new and general approach for designing high-performance SC using organic and inorganic materials.

After transmitting through the air/fiber tip plane entrance, the light propagates through the various thin layers and reflects and refracts at each interface according to Fresnels equations. The angles of refraction can be calculated from Snell's law. Using ray tracing and optical path iteration, Carroll et. al. presented a mathematical model for light transmission, absorption, and loss in fiber-based organic photovoltaics (see Figure 4.15) [28]. They found that their was enhanced absorption for longer fibers (0.5 cm) compared to shorter fibers (0.1 cm) which supports that the light is undergoing multiple scattering events within the device. Additionally, they found that higher absorption resulted from smaller diameter fibers. Again, small diameter fibers would promote more multiple reflection/refraction events at interfaces than large diameter fibers. This also supports the model that multiple scattering events are occurring within the fiber. Similar principle should apply to optical fiber DSSC as well.

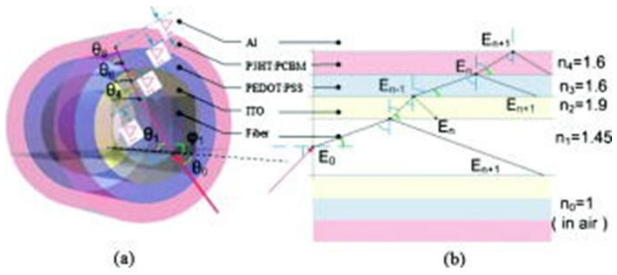

Figure 4.15 Model for light transmission, absorption, and loss in fiber-based organic photovoltaics using ray tracing and optical path iteration. [28]

4.5 Summary

In this chapter, an innovative hybrid structure was demonstrated that integrates optical fibers and nanowire arrays as 3D dye-sensitized solar cells that have a significantly enhanced energy conversion efficiency. In comparison to the case of light illumination normal to the fiber axis from outside the device (2D case), the internal axial illumination enhanced the energy conversion efficiency of a rectangular fiber-based hybrid structure by a factor of up to six for the same device. Furthermore, the absolute full-sun efficiency (AM 1.5 illumination, 100 mW cm^{-2}) is increased to 3.3 %, which is 120 % higher than the highest value reported for ZnO NWs grown on a flat substrate surface and 47 % higher than that of ZnO NWs coated with a TiO_2 film. The results in this chapter demonstrated a new approach from 2D to 3D solar cells with advantages of high efficiency, expanded mobility, surface adaptability, and concealed/remote operation capability.

4.6 References

[1] M. S. Dresselhaus and I. L. Thomas, "Alternative energy technologies," *Nature,* vol. 414, pp. 332-337, Nov 15 2001.

[2] B. Z. Tian, X. L. Zheng, T. J. Kempa, Y. Fang, N. F. Yu, G. H. Yu, J. L. Huang, and C. M. Lieber, "Coaxial silicon nanowires as solar cells and nanoelectronic power sources," *Nature,* vol. 449, pp. 885-U8, Oct 18 2007.

[3] G. Yu, J. Gao, J. C. Hummelen, F. Wudl, and A. J. Heeger, "Polymer Photovoltaic Cells - Enhanced Efficiencies Via a Network of Internal Donor-Acceptor Heterojunctions," *Science,* vol. 270, pp. 1789-1791, Dec 15 1995.

[4] J. J. M. Halls, C. A. Walsh, N. C. Greenham, E. A. Marseglia, R. H. Friend, S. C. Moratti, and A. B. Holmes, "Efficient Photodiodes from Interpenetrating Polymer Networks," *Nature,* vol. 376, pp. 498-500, Aug 10 1995.

[5] B. Oregan and M. Gratzel, "A Low-Cost, High-Efficiency Solar-Cell Based on Dye-Sensitized Colloidal Tio2 Films," *Nature,* vol. 353, pp. 737-740, Oct 24 1991.

[6] W. U. Huynh, J. J. Dittmer, and A. P. Alivisatos, "Hybrid nanorod-polymer solar cells," *Science,* vol. 295, pp. 2425-2427, Mar 29 2002.

[7] I. Gur, N. A. Fromer, M. L. Geier, and A. P. Alivisatos, "Air-stable all-inorganic nanocrystal solar cells processed from solution," *Science,* vol. 310, pp. 462-465, Oct 21 2005.

[8] P. Peumans, S. Uchida, and S. R. Forrest, "Efficient bulk heterojunction photovoltaic cells using small-molecular-weight organic thin films," *Nature,* vol. 425, pp. 158-162, Sep 11 2003.

[9] J. Y. Kim, K. Lee, N. E. Coates, D. Moses, T. Q. Nguyen, M. Dante, and A. J. Heeger, "Efficient tandem polymer solar cells fabricated by all-solution processing," *Science,* vol. 317, pp. 222-225, Jul 13 2007.

[10] A. Goetzberger, C. Hebling, and H. W. Schock, "Photovoltaic materials, history, status and outlook," *Materials Science & Engineering R-Reports,* vol. 40, pp. 1-46, Jan 2 2003.

[11] C. J. Brabec, N. S. Sariciftci, and J. C. Hummelen, "Plastic solar cells," *Advanced Functional Materials,* vol. 11, pp. 15-26, Feb 2001.

[12] M. Gratzel, "Photoelectrochemical cells," *Nature,* vol. 414, pp. 338-344, Nov 15 2001.

[13] J. Bisquert, D. Cahen, G. Hodes, S. Ruhle, and A. Zaban, "Physical chemical principles of photovoltaic conversion with nanoparticulate, mesoporous dye-sensitized solar cells," *Journal of Physical Chemistry B,* vol. 108, pp. 8106-8118, Jun 17 2004.

[14] M. Law, L. E. Greene, J. C. Johnson, R. Saykally, and P. D. Yang, "Nanowire dye-sensitized solar cells," *Nature Materials,* vol. 4, pp. 455-459, Jun 2005.

[15] M. R. Lee, R. D. Eckert, K. Forberich, G. Dennler, C. J. Brabec, and R. A. Gaudiana, "Solar Power Wires Based on Organic Photovoltaic Materials," *Science,* vol. 324, pp. 232-235, Apr 10 2009.

[16] X. Fan, Z. Z. Chu, F. Z. Wang, C. Zhang, L. Chen, Y. W. Tang, and D. C. Zou, "Wire-shaped flexible dye-sensitized solar cells," *Advanced Materials,* vol. 20, pp. 592-+, Feb 2008.

[17] Y. Qin, X. D. Wang, and Z. L. Wang, "Microfibre-nanowire hybrid structure for energy scavenging," *Nature,* vol. 451, pp. 809-U5, Feb 14 2008.

[18] B. Weintraub, Y. G. Wei, and Z. L. Wang, "Optical Fiber/Nanowire Hybrid Structures for Efficient Three-Dimensional Dye-Sensitized Solar Cells," *Angewandte Chemie-International Edition,* vol. 48, pp. 8981-8985, 2009.

[19] K. Kakiuchi, E. Hosono, and S. Fujihara, "Enhanced photoelectrochemical performance of ZnO electrodes sensitized with N-719," *Journal of Photochemistry and Photobiology a-Chemistry,* vol. 179, pp. 81-86, Apr 1 2006.

[20] B. O'Connor, K. P. Pipe, and M. Shtein, "Fiber based organic photovoltaic devices," *Applied Physics Letters,* vol. 92, pp. -, May 12 2008.

[21] J. W. Liu, M. A. G. Namboothiry, and D. L. Carroll, "Fiber-based architectures for organic photovoltaics," *Applied Physics Letters,* vol. 90, pp. -, Feb 5 2007.

[22] I. Gonzalez-Valls and M. Lira-Cantu, "Vertically-aligned nanostructures of ZnO for excitonic solar cells: a review," *Energy & Environmental Science,* vol. 2, pp. 19-34, 2009.

[23] M. Law, L. E. Greene, A. Radenovic, T. Kuykendall, J. Liphardt, and P. D. Yang, "ZnO-Al2O3 and ZnO-TiO2 core-shell nanowire dye-sensitized solar cells," *Journal of Physical Chemistry B,* vol. 110, pp. 22652-22663, Nov 16 2006.

[24] P. Ravirajan, A. M. Peiro, M. K. Nazeeruddin, M. Graetzel, D. D. C. Bradley, J. R. Durrant, and J. Nelson, "Hybrid polymer/zinc oxide photovoltaic devices with vertically oriented ZnO nanorods and an amphiphilic molecular interface layer," *Journal of Physical Chemistry B,* vol. 110, pp. 7635-7639, Apr 20 2006.

[25] G. K. Mor, K. Shankar, M. Paulose, O. K. Varghese, and C. A. Grimes, "Use of highly-ordered TiO2 nanotube arrays in dye-sensitized solar cells," *Nano Letters,* vol. 6, pp. 215-218, Feb 2006.

[26] Z. Li, R. S. Yang, M. Yu, F. Bai, C. Li, and Z. L. Wang, "Cellular Level Biocompatibility and Biosafety of ZnO Nanowires," *Journal of Physical Chemistry C,* vol. 112, pp. 20114-20117, Dec 25 2008.

[27] Z. Wang, "ZnO nanowire and nanobelt platform for nanotechnology," *Materials Science and Engineering: R: Reports,* vol. 64, pp. 33-71, 2009.

[28] Y. Li, W. Zhou, D. Xue, J. W. Liu, E. D. Peterson, W. Y. Nie, and D. L. Carroll, "Origins of performance in fiber-based organic photovoltaics," *Applied Physics Letters,* vol. 95, pp. -, Nov 16 2009.

CHAPTER 5

FUTURE DIRECTIONS

There are a number of future directions for studies contained within this thesis. They include improving the stability of 3-D solar cells, reduced the carrier recombination to boost the overall power conversion efficiencyImprove stability, and engineering the bandgap of the nanowires through doping.

Shown in Figure 5.1 is a schematic of a solid-state 3D optical fiber dye-sensitized solar cell. The optical fiber is coated with ITO thin film, ZnO thin film blocking later, ZnO nanowires, N719 dye, spiro-OMeTAD organic hole conductor, and Au.

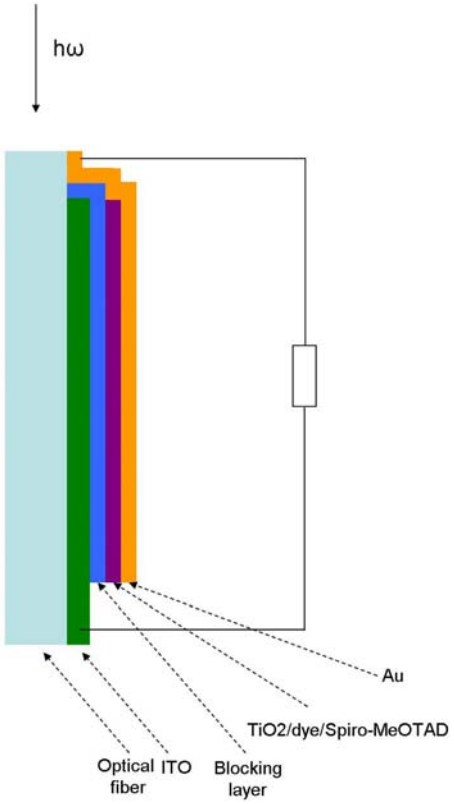

Figure 5.1 Schematic of solid-state 3D optical fiber dye-sensitized solar cell

The cross sectional SEM image for an actual solid-state device (F&D 100 um x 300 um optical fiber) can be seen in Figure 5.2a which shows an optical fiber with ITO thin film/ZnO thin film/N719 dye coated ZnO nanowires/spiro-OMeTAD organic hole conductor/Au. The nanowires exhibit lengths of 2-3 μm and diameters of 80-100 nm. Th synthesis was carried out at 80 ˚C, 2.5 mM Zn(NO3)2/HMTA, 20 hrs. The electrical performance can be seen in Figure 5.2b. The J-V traces for the normal-to-axis (NA) orientation exhibit the following metrics: V_{oc} 0.459 V, I_{sc} 8.70E-07 A, FF 0.41, η=0.0021%**.** The J-V traces for the parallel-to-axis (PA) orientation exhibit the following metrics: V_{oc} 0.294 V, I_{sc} 1.98E-08 A, FF 0.38, η=0.0075%. The efficiency enhancement factor is 3.6 suggesting the potential for high efficiency, stable devices using such an approach.

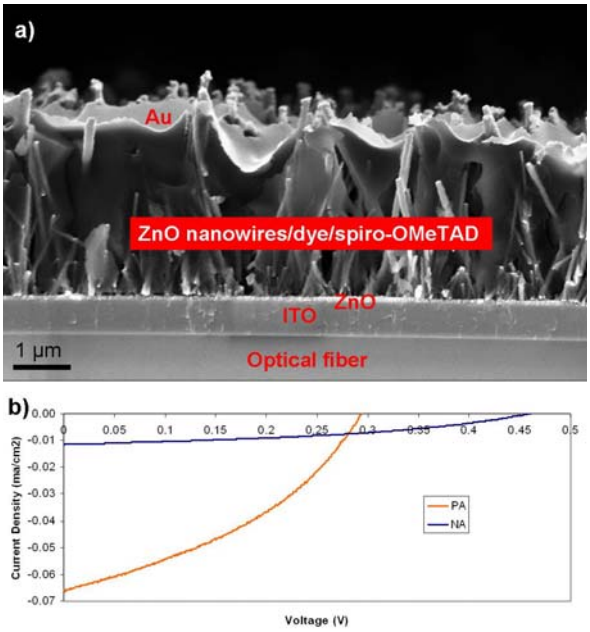

Figure 5.2 (a) cross sectional SEM image showing a solid state optical fiber DSSC (b) J-V characteristics comparing the two orientations. The efficiency enhancement factor is 3.6.

Another future direction of work in the thesis should be in exploring the surface science of the nanowires in an effort to optimize the solar cell performance. The ZnO facets etch due to the carboxylic acid end groups on the N719 dye and thus its performance is degraded. Materials such as TiO2 are more compatible with acid environments. Future work should entail ZnO nanowire core-TiO2 shell structures to minimize recombination the DSSCs. Figure 5.3 shows a TEM image of a solution-synthesized ZnO nanowire coated in a 50 nm amorphous layer of TiO2 by atomic layer deposition (ALD).

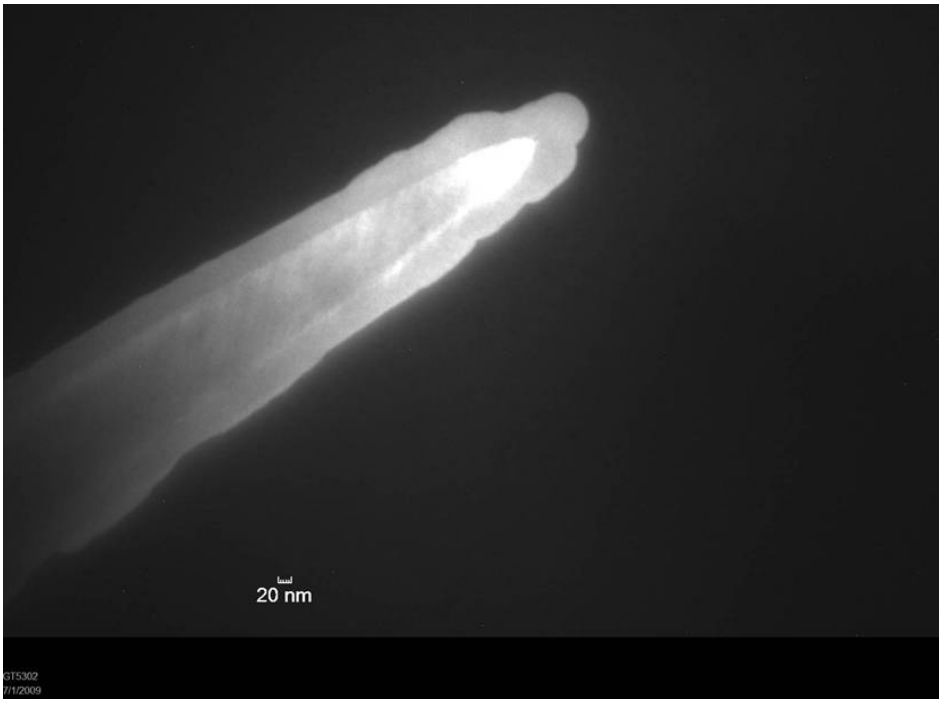

Figure 5.3 TEM image showing ZnO-TiO_2 core-shell structure

In order to design the next generation, of 3-D solar cells, the some ray trace modeling should be carried out to study the light transport down the optical fiber. Studies should aim to optimize the indices of refraction of the core and various material layers in an effort to maximize the photon-absorber layer interaction.

In terms of nanowire synthesis, future studies should aim at bandgap engineering to introduce defect levels to narrow the bandgap. By tailoring the absorption to longer wavelengths, bare ZnO can be used directly for photovoltaic and water splitting applications. In preliminary studies, NH3 has been added the precursor solution in an effort to introduce N defects into the ZnO lattice. Optical images of synthesis with and without NH3 added to the precursor solution can be seen in Figure 5.4a & b. The nanowires in Figure 5.4a were grown on a borosilicate cover slip (95 ˚C, 16 hrs, 20 mM $ZnCl_2$/HMTA, no additives, floating) and appear optically white. The nanowires in Figure 5.4b were grown on a borosilicate cover (95 ˚C, 16 hrs, 20 mM $ZnCl_2$/HMTA, NH_3 additive, floating) and appear optically yellow. Both substrates were initially sputtered with a 100 nm ZnO seed layer confirmed by SEM.

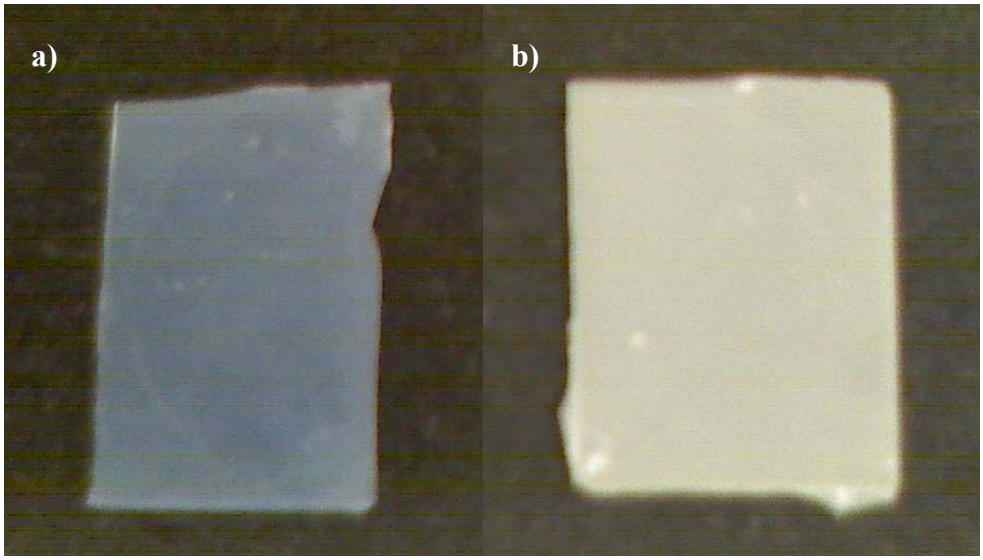

Figure 5.4 Optical micrograph of ZnO nanowire arrays on glass substrate (a) no NH_3 added (b) NH_3 added to the precursor solution

.

To investigate the possible introduction of N into the ZnO lattice, x-ray photoelectron spectroscopy (XPS) was carried out. Figure 5.5 & 5.6 shows the XPS data

for the sample without a NH_3 additive and with NH_3, respectively. The Zn $2p^{1/2}$(1045 eV), Zn $2p^{3/2}$(1021 eV), and O 1s (530 eV) peaks are evident in both as expected. In the sample with NH3 added, further XPS studies were carried out (Figure 5.6 bottom graph) to determine if N was present. However, no N 1s peak was evident at 398 eV which suggests that the solution-based NH_3 additive approach needs further investigation as a means of N-doping.

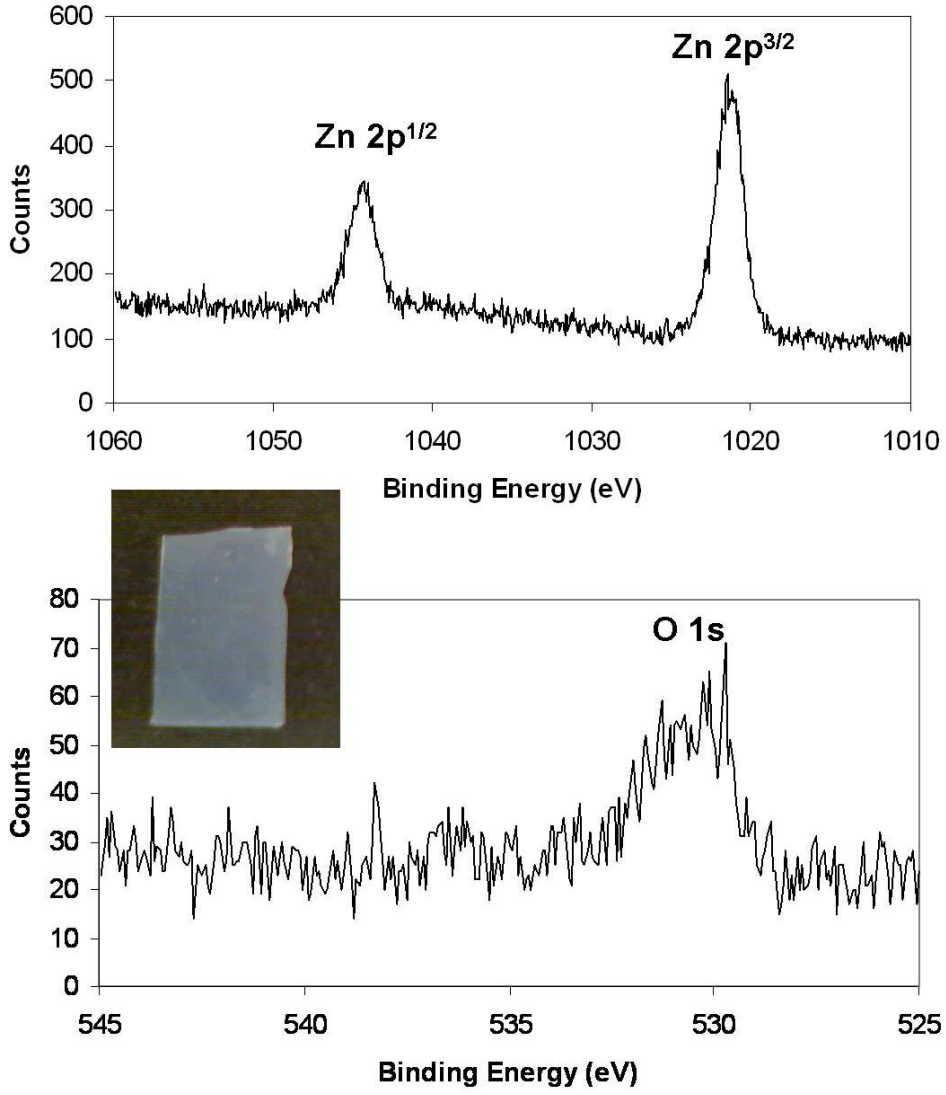

Figure 5.5 XPS analysis of ZnO nanowire array without using a NH_3 additive

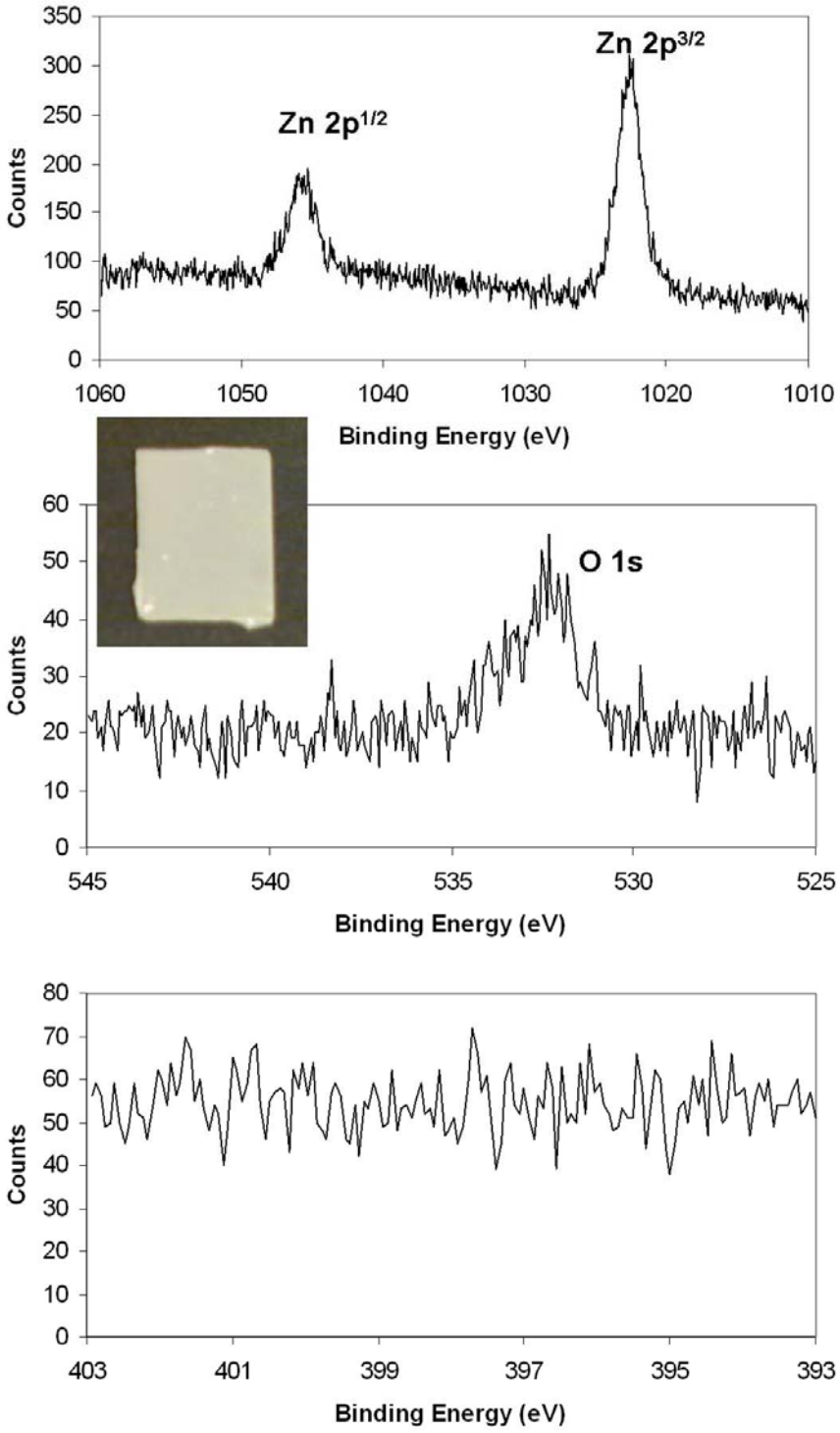

Figure 5.6 XPS analysis of ZnO nanowire array with precursor solution containing NH_3. No N 1s peak evident at 398 eV.

CHAPTER 6

CONCLUSION

The following is a summary of this thesis. Chapter 1 provided and introduction to the thesis. Chapter 2 provided a background in nanotechnology and photovoltaic fundamentals. Chapter 3 discussed rationale ZnO nanowire synthesis using aqueous solution-based approaches. Chapter 4 examined photovoltaic device fabrication and electrical and optical characterization. Chapter 5 discussed future directions and new questions raised.

In conclusion, the following thesis goals have been achieved: 1) rationale synthesis of a single ZnO nanowire on a polymer substrate without seeding; 2) Design of a wafer-scale technique to control ZnO nanowire array density using layer-by-layer polymers; 3) Determination of optimal nanowire field emitter density to yield a high field enhancement factor for applications in flat screen displays; 4) Rationale design of bridged nanowires across metal electrodes to order to circumvent post-synthesis manipulation steps; 5) Electrical characterization of bridged nanowires; 6) Rationale solution-phase synthesis of long ZnO nanowires on optical fibers; 7) Fabrication of ZnO nanowire dye-sensitized solar cells on optical fibers; 8) Electrical and optical characterization of solar cell devices; 9) Comparison studies of 2-D versus 3-D nanowire dye-sensitized solar cell devices; 10) Achievement of 6-fold power conversion efficiency enhancement using a 3-D approach.

VITA

BENJAMIN A. WEINTRAUB

BAW was born in Oceanside, CA on January 11, 1979. He attended public schools in Carlsbad, CA and received a B.S. in Chemistry from the University of California at Berkeley in 2001 before coming to the Georgia Institute of Technology to pursue a Ph.D. in Materials Science and Engineering. His research focused on the solution-phase synthesis of novel nanomaterials and their applications in solar cells. When he is not working on research, he enjoys practicing foreign languages, martial arts and guitar.